CHARACTERIZATION OF PROTON-EXCHANGED PLANAR OPTICAL WAVEGUIDES IN $LiNbO_3$

by

John Nikolopoulos, B. Eng. (Hon.)

Department of Electrical Engineering

McGill University

Montreal, Quebec

July 1990

A Thesis submitted to the Faculty of Graduate Studies and Research in partial fulfillment of the requirements for the degree of Master of Engineering για τους γονεις μου

Abstract

Planar optical waveguides fabricated by proton-exchange and annealed proton-exchange in $LiNbO_3$ are investigated.

The use of a Fermi function was found to accurately model the proton-exchange refractive index profile resulting in a better agreement between the measured effective mode indices and the computed dispersion curves compared to the conventional step-index profile. Numerical simulations of the nonlinear diffusion equation have shown that the proton-exchange process can not be adequately described by the well established ion-exchange equations.

A generalized Gaussian function was used to accurately model the refractive index profile in annealed proton-exchanged waveguides resulting in considerable improvements over previous work. Annealing was found to allow for flexibility in the tailoring of the waveguide parameters. In addition to establishing single mode propagation criteria, changes in these parameters were correlated with the fabrication conditions using a general power law thus showing that the anneal process is not characterized by simple diffusion mechanisms.

Résumé

Les guides optiques planaires fabriqués par l'échange protonique et la recuisson dans $LiNbO_3$ sont étudiés.

L'utilisation d'une fonction Fermi, plutôt que la fonction à saut conventionnelle, a permis de modeler plus précisement le profil d'indice de l'échange protonique. Cette vérification s'est établie en comparant les courbes de dispersions pour chacun des profils mentionnés ci-haut avec les indices de mode mesurés. Les simulations numériques de l'équation de diffusion non linéaire ont démontré que le processus d'échange protonique ne peut pas être décrit de façon adéquate par les équations bien établies de l'échange ionique.

Une fonction de Gauss généralisée a été utilisée pour mieux représenter le profil d'indice des guides fabriqués par la recuisson. Il a été démontré que la recuisson offre beaucoup de flexibilité pour ajuster les paramètres caractérisant les guides . En plus d'établissant les critères de la propagation monomode, les changements de paramètres ont été mis en relation avec les conditions de fabrication utilisant une loi de puissance générale ainsi démontrant que le processus de recuisson n'est pas caractérisé par des mécanismes de diffusion simples.

Acknowledgements

I would like to thank my supervisor, Professor Gar Lam Yip, for proposing the general topics investigated in this thesis and for his helpful suggestions throughout the duration of my stay at McGill.

I am particularly grateful to Dr. Nobuo Goto and Dr. Michel Bélanger for introducing me to some of the waveguide fabrication procedures and to Dr. Jacques Albert and Dr. Kiyoshi Kishioka for teaching me the measurement techniques used in the experimental part of this work. In addition, I must thank Dr. Ishiang Shih for his technical advice and for allowing me the use of his laboratory.

I must also express my gratitude to my colleagues Peter Noutsios, Arthur Vartanian, Feng Xiang, Jian-Yao Chen, and Mike Sekerka-Bajbus for their varied and stimulating conversations.

The contributions of the secretarial and technical staff in providing me with prompt and friendly assistance are also gratefully acknowledged.

This research was supported financially by the Natural Sciences and Engineering Research Council of Canada (NSERC) in the form of a post-graduate scholarship, an operating grant, and a strategic grant.

Contents

1 Introduction 1

1.1 General overview 1

1.2 $LiNbO_3$ technology 3

1.3 Research goal 4

1.4 Outline of original contributions 7

2 The Proton-Exchange (PE) Process 8

2.1 Introduction 8

2.1.1 The $LiNbO_3$ substrate 8

2.1.2 Ion-Exchange in $LiNbO_3$ 10

2.2 The Proton-Exchange (PE) technique 12

2.2.1 Brief overview 12

2.2.2 Waveguide formation using PE 13

2.2.3 Use of buffered melts 19

2.2.4 Use of annealing 21

2.2.5 Origin of the index change 24

2.3 Modeling the PE process 26

2.3.1 The nonlinear diffusion equation 26

2.3.2 Case I: Infinite melt volume assumption 27

2.3.3 Case II: Finite melt volume assumption 35

2.3.4 Case III: Concentration dependent self-diffusion coefficient . . 38

2.4 Modeling the annealing process 39

2.4.1 Analytic model 40

2.4.2 Numerical solution 41

3 Wave Propagation in PE and APE Planar Waveguides 50

3.1 Introduction 50

3.2 Propagation in anisotropic waveguides 50

3.2.1 Wave approach to biaxial anisotropic geometry 51

3.2.2 TM modes ($H_z = 0$) 53

3.2.3 TE modes ($E_z = 0$) 55

3.2.4 Dispersion relation for proton-exchanged waveguides 56

3.2.5 Design considerations 58

3.3 Propagation in inhomogeneous media 59

3.3.1 Scalar wave equation 59

3.3.2 The WKB method 61

3.3.3 Design considerations 63

4 Fabrication and Measurement Techniques **70**

4.1 Introduction 70

4.2 Fabrication 70

4.2.1 Substrate preparation 70

4.2.2 Cleaning procedure 72

4.2.3 Planar waveguide fabrication 73

4.2.4 Annealing of planar waveguides 75

4.3 Measurement techniques 76

4.3.1 Introduction 76

4.3.2 Modal spectroscopy 77

4.3.3 Propagation loss 80

5 Characterization of PE and APE Planar Waveguides in $LiNbO_3$ **91**

5.1 Introduction 91

5.2 Data reduction techniques 92

5.2.1 General considerations 92

5.2.2 Graded-index waveguides 93

5.2.3 Step-index waveguides 95

5.3 Characterization of PE planar waveguides 95

5.3.1 Introduction 95

5.3.2 Calculation of dispersion curves 98

5.3.3 Correlating $(\Delta n_s, d, a)$ with (T, t) 100

5.4 Characterization of APE waveguides 103

5.4.1 Introduction 103

5.4.2 Dispersion curves and single mode design considerations . . . 105

5.4.3 Modeling the refractive index profile 106

5.4.4 Nonlinear dependence of index on concentration 108

5.4.5 Correlating $(\Delta n_s, d, a)$ with (T_a, t_a) 109

6 Discussion and Conclusion **134**

A Prism Coupling Involving Anisotropic Media **138**

List of Figures

2.1 Orientation of crystallographic x, y, and z axes for z-cut $LiNbO_3$. . 44

2.2 Optical waveguide fabrication using proton-exchange. 44

2.3 Relationship between normalized concentration (x) and extraordinary refractive index increase (Δn_e). 45

2.4 Illustration of the shooting technique. 45

2.5 Comparison of 3-level implicit and Runge-Kutta numerical solution of nonlinear diffusion equation. 46

2.6 Effect of $\hat{\alpha}$ on the normalized concentration. 46

2.7 Effect of $\hat{\alpha} < 0$ on the normalized concentration. 47

2.8 Effect of $0.999 < \hat{\alpha} < 1$ on the normalized concentration. 47

2.9 Effect of anneal time on normalized concentration for $\hat{\alpha} = 0$. 48

2.10 Effect of anneal time on normalized surface concentration for various initial depth values (d_o) and $\hat{\alpha} = 0$. 48

2.11 Effect of $\hat{\alpha}$ on normalized annealed concentration profile. 49

3.1 Geometry of asymmetric anisotropic planar waveguide. 66

3.2 Three-layer biaxial geometry in the principal dielectric axes coordinate system where $(\theta, \phi) = (\frac{\pi}{2}, 0)$. 66

3.3 Effect of uniaxial anisotropy on the theoretical step-index dispersion curves as Δn_e ranges from (a) 0.12 to (b) 0.15. 67

3.4 Index profiles and ray trajectories for (a) homogeneous and (b) inhomogeneous waveguides. 68

3.5 Effect of turning point phase shift (ϕ_t) on the cutoff condition. . . . 69

4.1 Cutting the $LiNbO_3$ crystal substrate. 83

4.2 Sonic cleaning procedure. 83

4.3 Fabrication procedure for proton-exchanged waveguides using pyrophosphoric acid. 84

4.4 Annealing procedure for proton-exchanged waveguides: block diagram (top) and actual setup (bottom). 85

4.5 Field distributions in air gap, prism, and waveguide film. 86

4.6 Prism coupling to waveguide. 86

4.7 Experimental setup for measuring synchronous angles: block diagram (top) and actual system (bottom). 87

4.8 Waveguide prism holder (top) mounted on rotational stage (bottom). 88

4.9 Examples of some m-lines. 89

4.10 Experimental setup for measuring propagation loss. 90

5.1 Effect of δ on the shape of the normalized Fermi index profile. . . . 112

5.2 Effect of a on the shape of the normalized generalized Gaussian profile. 112

5.3 Comparison between Fermi and step-index dispersion curves and experiment (•) for $T = 200^oC$. 115

5.4 Comparison between Fermi and step-index dispersion curves and experiment (•) for $T = 230^oC$. 115

5.5 Comparison between Fermi and step-index dispersion curves and experiment (•) for $T = 260^oC$. 116

5.6 Guide depth versus square root of exchange time. Slope of least squares fit (——) yields effective diffusion coefficient (D_e). 116

5.7 Relationship between D_e and inverse temperature (T^{-1}). 117

5.8 Evolution of effective mode indices with anneal time (sample # 17). 121

5.9 Evolution of effective mode indices with anneal time (sample # 20). 121

5.10 Evolution of effective mode indices with anneal time (sample # 23). 122

5.11 Evolution of effective mode indices with anneal time (sample # 24). 122

5.12 Evolution of effective mode indices with anneal time (sample # 16). Waveguide remained single mode for entire anneal period. 123

5.13 Evolution of effective mode indices with anneal time (samples # 18 and # 19). Reducing d_o to $0.23\mu m$ (just above cutoff) extends single mode behaviour. 123

5.14 Evolution of effective mode indices with anneal time (samples # 21 and # 22). To extend single mode behaviour, the required $d_o = 0.20\mu m$ resulted in no modes being supported initially. 124

5.15 (top) Effect of the anneal temperature and time on the shape of the profile (a_{opt}). (bottom) Expanded view of the above figure focusing on $T_a = 300^oC$ and 400^oC. 126

5.16 Evolution of refractive index profile with anneal time (sample # 17). Solid and dotted curves refer to optimized and step approximation results, respectively. 127

5.17 Evolution of refractive index profile with anneal time (sample # 20). Solid and dotted curves refer to optimized and step/Gaussian approximation results, respectively. 127

5.18 Evolution of refractive index profile with anneal time (sample # 23). Solid and dotted curves refer to optimized and Gaussian approximation results, respectively. 128

5.19 Evolution of refractive index profile with anneal time (sample # 24). Solid and dotted curves refer to optimized and Gaussian approximation results, respectively. 128

5.20 Effect of anneal temperature and time on waveguide depth. 129

5.21 Effect of anneal temperature and time on waveguide surface index change. 129

5.22 Effect of anneal temperature and time on the area under the refractive index versus depth curves. 130

5.23 Least squares nonlinear regression fit to evolving surface index changes. Here, Δn_{s_o} is the initial ($t_a = 0$) surface index change. 131

5.24 Least squares nonlinear regression fit to evolving depth changes. Here, d_o is the initial depth. 131

5.25 Comparison of simple diffusion theory with experiment. 132

5.26 Comparison of simple diffusion theory with experiment. 132

A.1 Coupling to a PE $LiNbO_3$ waveguide using a rutile (TiO_2) prism. The vector, $\vec{c}$, refers to the optic axis direction in each medium. . . . 140

List of Tables

2.1 Physical properties of $LiNbO_3$ 10

2.2 Guesses to be used for g_o for various values of $\hat{\alpha} = \omega\hat{c}_s$. 33

4.1 Physical properties of pyrophosphoric acid ($H_4P_2O_7$) 73

5.1 TM effective mode index measurements. 113

5.2 Computed waveguide parameters for a Fermi index profile. 114

5.3 Temperature dependence of effective diffusion coefficient and corresponding waveguide parameters. 117

5.4 TM effective mode index measurements before and after annealing (Note that $T = 200^oC$ for all initial PE waveguides given in Table 5.4-5.6). 118

5.5 TM effective mode index measurements before and after annealing. . 119

5.6 TM effective mode index measurements before and after annealing. . 120

5.7 Single mode propagation criteria for APE waveguides. 124

5.8 Computed anneal waveguide parameters for a generalized Gaussian index profile. 125

5.9 Least squares fitting parameters of evolving depth and surface index changes. 130

5.10 Propagation loss measurements. 133

Chapter 1

Introduction

1.1 General overview

Originally coined in 1969 by S.E. Miller of Bell Laboratories, the term *Integrated Optics* (IO) has come to be associated with a growing field of scientific endeavor whose aim is to provide means for the controlling and processing of the various characteristics of light (eg. phase, polarization, amplitude, frequency, direction of propagation, etc.) using thin film and microfabrication technology. Examples of such integrated optical circuits (IOC) include modulators, filters, switches, power dividers, mode splitters, wavelength demultiplexers, frequency shifters, and directional couplers. Certainly, the beginnings of this area of research were inextricably linked to the rapid development of fiber-optic communication systems in the 1970's. In order to take full advantage of the large bandwidth that such systems provided, a supporting optical technology interfaced to the fiber and electronics was needed. At least initially then, IO was geared toward satisfying this need and, as in integrated electronics, providing increased reliability and performance. The field has since grown tremendously promising, in addition, widespread applications for signal processing, optical sensing, and nonlinear optics [1,2,3].

The fabrication of integrated optical circuits has been achieved in various materials employing a variety of techniques. These materials can be grouped [4,5] in the following distinct categories: glass, inorganic oxide crystals (eg. lithium niobate and tantalate), III-V semiconductors, and organic polymers. Due to its excellent electro-optic, acousto-optic, and waveguiding properties as well as its relative maturity in terms of device performance, fabrication technology, and packaging, lithium niobate ($LiNbO_3$) has been and will continue to be a prime candidate for many integrated optics applications [1,6,7,8]. Since sources and emitters can not be realized in $LiNbO_3$, this technology is characterized as *hybrid.* Although the use of III-V materials not only overcomes this latter drawback but, also, allows for integration with high speed electronics, material limitations and fabrication difficulties have, as of yet, prevented this *monolithic* approach to IOC design from outperforming its hybrid counterpart [9].

The material incompatibility problem associated with $LiNbO_3$ has been recently addressed by Yi-Yan et al. [10] who reported integration of a III-V semiconductor detector with a $LiNbO_3$ waveguide using an epitaxial lift-off technique. In addition, there has been growing interest [11] in polymeric materials which, aside from allowing integration with electronics, have demonstrated tremendous fabrication flexibility resulting in the ability to tailor the electro-optic and waveguiding properties. These advances made in the material and fabrication aspects of IOC technology have been paralleled by similar progress in novel device modeling and computer-aided optimization techniques which have allowed designers to better understand the properties of more complicated integrated optical circuits [6,12,13]. These exciting developments should lead to the design and fabrication of high performance, cost effective, as well as novel optical devices.

It must be emphasized, however, that the future success of the commercialization of IOC technology will be dependent on advances made in both the optical and electrical aspects of package integration. In particular, the precise alignment and rugged attachment of optical fibers (i.e. 'pig-tailing') to the IOC continue to be challenging problems for optical device packagers [6,7,14].

1.2 $LiNbO_3$ technology

As mentioned above, $LiNbO_3$ is an attractive material for the near term commercialization of integrated optical circuits. Commercially available product lines of $LiNbO_3$ based IOC devices include [6,15,16] phase and intensity modulators, directional coupler switches, crossbar switch arrays, and modulator circuits for fiber-optic gyroscopes.

The basic component in all these IOC devices is the optical waveguide. The fabrication of such structures in $LiNbO_3$ has been achieved using a variety of techniques including [1,5,7,17] outdiffsion, metal (eg. Ti, V, Ni) indiffusion, proton-exchange, and ion-implantation. Of these, only Ti indiffusion and, more recently, proton-exchange (PE), have reached an advanced stage of development. The salient features of these fabrication technologies are:

- Ti indiffusion: A rather involved fabrication procedure consisting of vacuum-depositing a thin layer of Ti followed by an elevated temperature diffusion ($T > 950^oC$) results in high quality (i.e. low loss, good electro-optic behaviour) waveguides. Both the extraordinary and ordinary indices of refraction are increased thus allowing the propagation of TE and TM modes. The resulting index profiles are well approximated by a Gaussian function with surface index increases of about 0.01. Recent work [18] has shown that these index increases are nonlinearly related to Ti concentration and, in addition, exhibit some wavelength dependence. Optical damage (i.e. inability to support high power densities) is a serious problem at shorter wavelengths ($< 1.0\mu m$) [7].
- proton-exchange: A convenient and relatively simple fabrication technique

involving a low temperature ($T < 300^oC$) exchange of $LiNbO_3$ immersed in a proton source (typically benzoic acid). The resulting waveguide index profile is approximately a step with changes in the extraordinary and ordinary indices of 0.12 and -0.04, respectively, with slightly smaller values reported for longer wavelenghts [19]. A nonlinear dependence of these index changes on hydrogen concentration has also been observed [20]. The negative change in the ordinary index allows for the propagation of a single polarization. By using buffered melts and/or annealing, many of the problems associated with PE in pure melts (eg. degradation of electro-optic and acousto-optic coefficients, index instabilities, large scattering loss) can be avoided. In addition, these techniques provide for considerable flexibility in the tailoring of the waveguide properties [19]. Of particular note is the greater power handling capability of PE waveguides compared to their Ti indiffused counterparts.

Recently, a combination of PE and Ti indiffusion has been used to improve birefringence control which is needed, for example, in second harmonic generation applications [7]. Hence, it is clear that the proton-exchange technique has helped to complement as well as improve the more established $Ti : LiNbO_3$ technology.

1.3 Research goal

Generally, the goal of this thesis research is to characterize planar optical waveguides made by proton-exchange in $LiNbO_3$. Such characterization studies constitute the necessary first step toward the eventual fabrication and design of integrated optical devices. Indeed, it has been recently shown that the use of more sophisticated computer-aided design (CAD) tools such as the *Beam Propagation Method* (BPM) for the design and optimization of IOC's becomes effective only when accurate and reproducible characterization data is available [13,14].

When this work began, the majority of previous studies had focused on the use of benzoic acid (C_6H_5COOH) as the proton source [19,21,22,23]. Recently, the use of pyrophosphoric acid ($H_4P_2O_7$) as an alternative proton source was found to result in higher index and lower loss waveguides [24,25,26]. Parallel to this, the accuracy of the conventional PE waveguide step-index model was being questioned [27]. In addition, an in depth study of the diffusion modeling of the PE process was still lacking. Hence, the aim of the first stage of the research consists of the following:

- To accurately model the refractive index profile in PE waveguides in order to assess the validity of the conventional step-index assumption and simultaneously address the controversy surrounding the observed higher index increases associated with pyrophosphoric acid compared to benzoic acid.
- To investigate the effectiveness of the proposed proton-exchange diffusion models as design tools.

It was realized from the outset that the fabrication of high quality waveguides necessitated the use of buffered melts or annealing [19]. Although several extensive studies had been performed on the use of buffered melts [28,29], a corresponding effort to better understand the anneal process has concentrated for the most part on reducing waveguide loss and improving electro-optic behaviour [30,31,32,33]. A thorough investigation of the modeling of the diffusion process and the refractive index profiles in annealed proton-exchanged (APE) waveguides was not available. Moreover, it has recently [32] been shown that the APE technique holds certain advantages over the use of buffered melts (eg. reduced fabrication time and complexity). Hence, it is desirable to be able to accurately characterize it. The purpose of the second stage of this research then is also twofold:

- To gain a better understanding of the anneal process by accurately correlating measured index profiles with a more extensive range of fabrication conditions.

- To investigate the effectiveness of the proposed APE diffusion models as design tools.

It is important to note that since this work began several studies have been published which have contributed to improving the understanding of the proton-exchange and annealing processes (see Chapter 5 for references).

The various topics discussed in this thesis are organized as follows:

- Qualitative and quantitative description of the physical mechanisms underlying the proton-exchange and annealing processes (Chapter 2).
- Investigation of the propagation characteristics of PE and APE waveguides including a rigorous treatment of the often neglected uniaxial anisotropy in such structures and an introduction to the WKB method (Chapter 3).
- Description of the proton-exchange surface coating and annealing fabrication procedures as well as the waveguide measurement techniques based on the prism coupler (Chapter 4).
- Characterization of planar PE and APE waveguides. Detailed discussion of data reduction techniques including the modeling of the waveguide refractive index profile, generation of dispersion curves, and correlation of waveguide properties with fabrication conditions (Chapter 5).
- Brief summary and discussion of work as well as comments on future directions in proton-exchange technology (Chapter 6).

1.4 Outline of original contributions

This thesis research has resulted in several original contributions to the field of planar PE $LiNbO_3$ technology. These include:

- A detailed characterization of proton-exchanged waveguides using an improved Fermi index model [34,35].
- A detailed characterization of annealed proton-exchanged waveguides using an improved generalized Gaussian index model [35,36].

Chapter 2

The Proton-Exchange (PE) Process

2.1 Introduction

In this chapter, the physical mechanisms underlying the proton-exchange process are described. After briefly discussing the development of PE, details of waveguide formation as well as the use of the annealed proton-exchange and buffered melt techniques (which, as will be seen shortly, are necessary for the fabrication of high quality waveguides) are introduced from a qualitative point of view. The remaining part of the chapter concentrates on the various diffusion models which have been used to describe some of the quantitative aspects of this process. The effectiveness of these models as design tools is rigorously investigated.

2.1.1 The $LiNbO_3$ substrate

As mentioned in Chapter 1, due to its excellent physical properties (see Table 2-1) including a large electro-optic and acousto-optic figure of merit, a high birefringence as well as its transparency in the near infrared and visible region of the optical spectrum, $LiNbO_3$ has been and will continue to be a prime candidate for integrated optics applications. Of course, the widespread use of this crystal has only been possible due to recent advances in the material development which have allowed the crystal to be available in both acoustic and optical grades [17]. Although the former suffices for surface acoustic wave (SAW) devices, the optical grade with its higher degree of structural integrity and stoichiometric uniformity is necessary for IO applications. Several extensive reviews describing the various material properties of $LiNbO_3$ can be found in the literature [1].

It has been established that lithium niobate has a rhombohedral crystalline structure and, as a result, is a uniaxial crystal with a symmetry axis defined as the z-axis and usually referred to as the *optic* axis. This uniaxial nature allows the crystal to be commercially available in various cuts where the optic axis direction is specified with respect to the polished surface. For example, a crystal substrate with a plane cut normal to the crystallographic z-axis (i.e. optic axis) is called z-cut $LiNbO_3$ [5]. As it is a birefringent crystal, light propagating along the optic axis with polarization in the $x - y$ plane is called an *ordinary* wave; propagation perpendicular to the optic axis is characterized by an *extraordinary* wave. For z-cut $LiNbO_3$ (see Fig. 2.1 at the end of this chapter), the corresponding index tensor becomes,

$$[n] = \begin{bmatrix} n_o & 0 & 0 \\ 0 & n_o & 0 \\ 0 & 0 & n_e \end{bmatrix} \tag{2.1}$$

where n_o and n_e are the *principal* [1] ordinary and extraordinary refractive indices of refraction for $LiNbO_3$. Room temperature measurements of these bulk indices has revealed the following wavelength dependencies [1],

$$n_e(\lambda) = 2.122 + \frac{0.031}{\lambda^2} \tag{2.2}$$

$$n_o(\lambda) = 2.195 + \frac{0.037}{\lambda^2} \tag{2.3}$$

where λ is in microns. For example, at $\lambda = 0.6328\mu m$ (helium-neon laser light), $n_e = 2.200$ and $n_o = 2.287$ giving a birefringence of $n_e - n_o = -0.09$. Note that

---

[1] The index tensor is diagonal because the principal dielectric axes coordinate system is assumed (see Chapter 3).

since $n_e < n_o$, the crystal is described as *negative* uniaxial.

In addition to the various cuts and grades which are available, the crystal can be grown over a range of compositions $(Li_2O)_x(Nb_2O_5)_{1-x}$. For device applications, however, the so-called congruent composition ($x = 0.486$) is preferred because of the high degree of compositional uniformity that can be achieved. As a final comment, the high melting point and Curie temperature of congruent $LiNbO_3$ result in stable room temperature characteristics, yet another attractive feature of this material [1].

Table 2.1: Physical properties of $LiNbO_3$

Curie temperature	$1150°C$
Melting point (congruent)	$1243°C$
Refractive index ($\lambda = 0.6328\mu m$)	$n_e = 2.200$ $n_o = 2.287$
Birefringence	-0.1
Attenuation	$< 0.5\frac{dB}{cm}$
Transparent window	$0.4 - 5\mu m$
Electro-optic coefficient	$r_{33} = 30 \times 10^{-12}\frac{m}{V}$

2.1.2 Ion-Exchange in $LiNbO_3$

As far as the development of integrated optical circuits is concerned, the various attractive properties of lithium niobate discussed above can only be taken advantage of if one is able to confine light power in a well defined region; in other words, it is necessary to have a waveguide. Furthermore, this waveguide should not only possess stable (i.e. time-invariant) optical parameters such as its refractive index profile but, also, be made without significantly degrading the attractive features of the bulk crystal, for example, the electro-optic coefficient [3]. In Chapter 1, the numerous techniques for waveguide formation in $LiNbO_3$ were introduced. Of these, it was pointed out that the $Ti : LiNbO_3$ technology had reached the highest level of maturity. However, the rather involved fabrication procedure as well as the problems [7,17] of optical damage, relatively small Ti indiffusion rates, and unacceptably wide variation in device performance from different batches have spurred interest in new fabrication techniques to complement as well as improve the $Ti : LiNbO_3$ technology. One such technique is the proton-exchange method.

Interestingly, the beginnings of proton-exchange are inextricably linked with the ion-exchange technique well known from glass technology in connection with the improvement of the surface mechanical properties (i.e. strengthening) of glass and, recently (as well as more relevant to the discussion at hand), its ability to produce thin or shallow waveguiding layers on glass surfaces [37]. In this process which is quite different from diffusion, cations from an external source such as a molten salt bath are exchanged (sometimes in the presence of an electric field) with cations in the glass substrate (eg. $K - Na$, $Ag - Na$). Due to the differences in size and chemical properties of the exchanged ions, the physical parameters of the exchanged layer including specific volume, ionic polarizability, stress state, and index of refraction will generally be different from those of the substrate [38].

The first reports of ion-exchange of $LiNbO_3$ in silver nitrate ($AgNO_3$) [39] and thallium nitrate ($TlNO_3$) [40] melts revealed step-like refractive index profiles with an extraordinary refractive index change $\Delta n_e \approx 0.12$. Moreover, no measurable change in the ordinary index of refraction (n_o) was observed. These initial reports attributed the refractive index change to a $Tl - Li/Ag - Li$ exchange. Further study [41] with $TlNO_3$ melts not only revealed little Tl accumulation in the waveguide layer but, rather, a loss of Li/Li_2O as the main result of this exchange process. In addition, these index changes were found to lack reproducibility and, as a result, it soon became apparent that the introduction of the heavy ions Ag and Tl was unconnected with these observed large index changes. By studying the strength of the $O - H$ infrared absorption in the waveguide layer (which is proportional to the hydrogen content present), Jackel and Rice [42] came to the conclusion that an impurity in the thallium and silver nitrate melts, specifically, hydrogen, was responsible for the observed index changes. This $H - Li$ exchange has henceforth been referred to as proton-exchange (which is essentially an ion-exchange involving protons).

2.2 The Proton-Exchange (PE) technique

2.2.1 Brief overview

Originally used as a method for preparing new cubic perovskites from $LiNbO_3$ and $LiTaO_3$ [43], the proton-exchange process [21] was found to be a simple and fast technique for optical waveguide formation in $LiNbO_3$. In addition to their relative ease of fabrication, proton-exchanged optical waveguides possess other advantages as compared to their titanium indiffused counterparts. These include higher index increases,[1] greater power handling capability, polarization control, and the ability to temperatune tune the refractive index profile [44]. Another attractive feature of this technique is the relatively low temperature ($140-300°C$) required for waveguide fabrication. The resulting waveguides have been found to have a high extraordinary refractive index change ($\Delta n_e = 0.12$) [22,23] and a small but significant decrease [45] in the ordinary index of refraction ($\Delta n_o = -0.04$). This anisotropic index change allows for only transverse electric (TE) modes to be guided in PE x and y-cut $LiNbO_3$ and transverse-magnetic (TM) modes in PE z-cut substrates (This property thus opens up interesting possibilities for polarization control optical devices). Various researchers have also reported a general overall improvement in the optical properties for PE waveguides which have been subsequently annealed [32,46] and/or waveguides fabricated from buffered (i.e. diluted) melts [29]. Extensive optical waveguide studies carried out in the different cuts of both $LiNbO_3$ and

---

[1] The higher index increases provided by PE as compared to Ti indiffusion is useful in terms of light confinement, available index mismatch for wavelength filters, and fabrication of bent waveguides with small radii of curvature [5,6].

$LiTaO_3$ using (for the most part) benzoic acid melts as the proton source can be found. See, for example, the excellent review by Wong [19].

Before moving on with the details of waveguide formation in $LiNbO_3$, some brief comments will be made concerning the use of PE in $LiTaO_3$. Compared with $LiNbO_3$, $LiTaO_3$ has similar electro-optic coefficients, a lower birefringence, higher stability, and a lower susceptibility to optical damage. Unfortunately, due to the low Curie temperature of $LiTaO_3$ ($T_c \approx 650^oC$), the crystal must be repoled after a relatively high temperature titanium indiffusion ($T > 1000^oC$) in order to restore domain alignment and maximize the electro-optic effect for active devices [1,19]. This obviously adds to the fabrication complexity and, consequently, has so far reduced interest in $LiTaO_3$ as far as IOC applications are concerned. However, the use of the relatively low temperature PE process avoids this problem and thus allows the possibility of taking advantage of some of its superior properties. Indeed, there have been recent reports of the fabrication of high quality $LiTaO_3$ PE waveguides and devices [47].

2.2.2 Waveguide formation using PE

The proton-exchange process in $LiNbO_3$ is performed (see Fig 2.2) by immersing a $LiNbO_3$ single crystal in a proton source (eg. benzoic, palmitic, pyrophosphoric acid) kept at a fixed temperature ($100 - 300^oC$) for a desired amount of time (5 minutes to several hours). The end result is a depletion of lithium and the replacement with hydrogen in the crystal. Although (as will be discussed shortly) the exact mechanism of the exchange and the structure of the resulting waveguiding layer are quite complex and not fully understood, this process has nonetheless been described [19,28] by the following chemical equilibrium reaction,

$$LiNbO_3 + C_6H_5COOH \longleftrightarrow Li_{1-x}H_xNbO_3 + (C_6H_5COOLi)_x \qquad (2.4)$$

where benzoic acid is assumed as the proton source. The strength of the acid used will determine whether complete or partial exchange has taken place. The former has only been observed in $LiNbO_3$ *powder* using strong acids such as HNO_3 or H_2SO_4. The result is the formation of the cubic perovskite phase $HNbO_3$. This structural transformation (i.e. hexagonal to cubic) does not allow for totally exchanged layers to be obtained on $LiNbO_3$ *single crystal* because the resulting stress prevents any epitaxial adhesion of the new $HNbO_3$ phase on the substrate [3,19]. Hence, for optical waveguide fabrication, only partial exchange is necessary. By using (undiluted) benzoic acid (which is a relatively weak acid) waveguides can be formed in x and z-cut substrates; except for very short exchange times [48], y-cut substrates are destroyed (i.e. etched). In fact, this etching or surface damage has also been observed [49] in x and z-cut samples but only after much longer exchange times (eg. 4hr on x-cut at 220^oC, 15hr in z-cut at 210^oC, compared to a few minutes in y-cut at 220^oC). This surface damage is believed [50] to be caused by lattice stress within the waveguide layer which increases with the exchange time and is only relaxed through the formation of cracks on the crystal surface (i.e. etching). However, by prediffusing the y-cut substrates with Ti, this etching of the crystal surface can be avoided. Several characterization studies can be found on these titanium indiffused proton-exchanged (TiPE) waveguides [45,51,52]. Due to the anisotropic PE index change mentioned earlier, the TiPE process allows for the fabrication of waveguide structures (eg. buried waveguides [53]) which can not be made using the Ti indiffusion or PE techniques alone.

The use of the prism-coupler technique (see Chapter 4) has allowed researchers [22,23] to assess some of the waveguide properties of the PE waveguides. The results can be summarized as follows:

- The extraordinary refractive index profile is approximately a step with $\Delta n_e = 0.12 - 0.13$ ($\lambda = 0.6328\mu m$) for the most part independent of diffusion time, temperature, and particular cut of the crystal. For longer wavelengths, slightly smaller values have been observed.

- Contrary to initial reports, the ordinary index decreases with $\Delta n_o = -0.04$.
- Propagation losses varied between $(1 - 6)\,\frac{dB}{cm}$ with the x-cut values being consistently the lowest.
- As in ion-exchanged glass waveguides, the extent of PE is determined by the time and temperature of the process. Diffusion is fastest in x-cut substrates. Optical depth values are found to be linearly related to the square root of time while diffusion coefficients are found to obey the *Arrhenius Law* as follows,

$$d = \sqrt{D_e t} \tag{2.5}$$

$$D_e = C_1 \exp\left(\frac{-C_2}{T}\right) \tag{2.6}$$

where,

d = optical depth

D_e = effective diffusion coefficient

t = diffusion time

T = diffusion temperature

C_1, C_2 = constants for the PE process

The above results are for waveguides fabricated in neat (i.e. pure) benzoic acid which has been the focus of the majority of studies to date. This is because benzoic acid not only possesses a high boiling point ($T_b = 249°C$) which allows for the use of high processing temperatures and, hence, large diffusion coefficients but, also, stability throughout its liquid range which results in excellent reproducibility [21]. In addition, the acid is cheap and has low toxicity. Other acids have been used, for example, palmitic acid. The resulting waveguides, however, have been found to have properties very similar to those obtained using benzoic acid [45]. Recently, there has been some controversy in the literature about the supposedly higher index increases and lower waveguide losses obtained using pyrophosphoric acid ($H_4P_2O_7$) as a proton source [24,54,55,77]. In addition, the accuracy of the conventional PE step-index model has been questioned [27]. In order to address these topics, an extensive waveguide characterization using pure pyrophosphoric acid was performed and is presented in considerable detail in Chapter 5. This investigation constituted a starting point of this thesis.

In addition to the above studies, numerous researchers have used a variety of microanalytical techniques including Rutherford backscattering spectroscopy (RBS) [49], secondary ion mass spectroscopy (SIMS) [56], X-ray diffraction (XRD) [50,62], elastic recoil detection analysis (ERDA) [3], nuclear reaction analysis (NRA) [29,49] and infrared spectroscopy (IS) [46,57,58], to analyze the structural properties of the PE waveguiding layer. The results from these studies can be summarized as follows:

- Optical waveguide thicknesses measured using RBS, ERDA, NRA, and SIMS are consistent with prism-coupling results.

- These techniques generally reveal step-like hydrogen concentration profiles. Corresponding lithium depletion profiles are not as step-like suggesting that PE is not strictly a one for one ion-exchange.

- ERDA and NRA estimates for the value of x in $Li_{1-x}H_xNbO_3$ (the ratio of H to Li within the waveguide layer) range from $x = 0.65 - 0.80$.

- XRD analysis reveals the existence of positive lattice strains in the waveguide layer. These strains are different for directions parallel and perpendicular to the optic axis and are greatest for y-cut crystals.

- X-ray studies [66] on $LiNbO_3$ powders show that multiple phases (i.e. a phase is characterized by a particular value of x) with lattice constants very different from virgin $LiNbO_3$ can exist for large values of x. Other research groups, however, have not detected such phases in single crystal proton-exchange waveguides [49,59]. These inconsistencies suggest that results for powders can not necessarily be extended to include single crystal $LiNbO_3$.

- Double crystal XRD studies have revealed the existence of some Li deficient phases (eg. $LiNb_3O_8$ and Nb_2O_5) at the diffusion boundary whose formation is dependent on the Li/H ratio and temperature.
- IS studies have shown that hydrogen is incorporated within the crystal in the form of free ($\nu_{max} = 3505cm^{-1}$) and hydrogen-bonded ($\nu_{max} = 3250cm^{-1}$) hydroxyl (OH) groups. Interestingly, the latter group is absent in z-cut waveguides. Although the area of the infrared absorption bands associated with these hydroxyl groups is found generally to be proportional to $\sqrt{t}$, some controversy exists in the literature as to whether a melt-dilution effect occurs (to be elaborated upon later). Furthermore, the linear relationship between band area and temperature suggests that there is a *minimum* temperature associated with PE ($141°C$ for z-cut, $132°C$ for x-cut).
- Recent SIMS results show a pile up of Li at the Li/H boundary and, hence, Li and H profiles which are not compliments of each other. In addition, the ***double-alkali effect*** (to be discussed later) is proposed as the mechanism underlying the PE process.

These findings support the contention that, although its kinetics are described by square root time dependencies, the PE process is not a simple diffusion nor a one for one ion-exchange.

Despite their many attractive features, it was soon realized that PE waveguides fabricated in pure benzoic acid possessed serious problems including [19]:

- short and long term index instabilities
- degradation of electro-optic coefficient and reduced acousto-optic interaction efficiency
- large scattering and, hence, propagation loss
- high insertion loss (large mismatch in numerical aperture)
- increased DC drift
- etching of y-cut substrates
- interaction with ambient water vapour at room temperature (i.e. instability)

Based on their observations of $LiNbO_3$ powders,[2] Jackel and Rice [61] came to the conclusion that these problems are due to the high concentration of hydrogen within the waveguide layer (i.e. a large value of x in $Li_{1-x}H_xNbO_3$). This large $H-Li$ exchange results in the formation of multiple crystal phases (several rhombohedral as well as cubic $HNbO_3$) which, except for the single α phase existing for $x < 0.12$, possess lattice constants considerably different from the virgin $LiNbO_3$. Keeping this model in mind, some of the above problems can be readily explained. For example, the strain produced by the lattice constant change explain the degradation of the electro/acousto-optic coefficients as well as the etching of the y-cut substrates. Moreover, the existence of several phases in equilibrium results in large scattering at their boundaries and the fact that these phases are easily converted suggest possible problems with index instabilities. In short, by reducing the fractional concentration of hydrogen to $x < 0.12$, the resulting waveguide layer will be composed of the single rhombohedral α phase (with lattice constants similar to the

---

[2] The reasons for using powders instead of single crystal material have to do with economics as well as convenience. Powders are not only much cheaper but, also, more readily available in large quantities than their single crystal material counterparts. In addition, certain experiments may be more conveniently performed (from a technical point of view) by using powders [60].

virgin $LiNbO_3$) and, hence, will be structurally well matched to the substrate. The waveguides thus formed will retain the attractive properties offered by the bulk material (eg. low loss, good electro-optic behaviour, etc.) [32,66].

It must be emphasized, however, that this discussion concerns $LiNbO_3$ powders and, as pointed out earlier, there is considerable controversy in the literature about extending results from powders to single crystal material (from which optical waveguides are fabricated). Even though this multiple crystal phase model has not (as of yet) been confirmed for the single crystal material situation, the contention that the fractional concentration, x, of hydrogen must be reduced in order to obtain good quality waveguides is strongly supported by the fact that the use of the annealing as well as buffered melt techniques (which, as will be seen shortly, both result in the reduction of x) have yielded greatly improved overall performance [29,32,46].

2.2.3 Use of buffered melts

The use of so-called buffered melts to reduce the hydrogen ion concentration consists [28] of adding compounds such as potassium nitrate/benzoate (KNO_3, C_6H_5COOK) or various lithium salts ($LiNO_3$, Li_2CO_3, C_6H_5COOLi) to pure benzoic acid. Since the goal of this procedure is to push the equilibrium described by Eq. 2.4 to the left, one expects greater effects to occur for the case of lithium salts. This is seen as follows. Using $LiNO_3$ and Li_2CO_3 as examples, one has:

$$LiNO_3 \longleftrightarrow Li^+ + NO_3^- \tag{2.7}$$

$$Li_2CO_3 \longleftrightarrow 2Li^+ + CO_3^- \tag{2.8}$$

The above chemical equilibrium reactions show that additional Li ions are introduced with the result that the equilibrium is pushed to the left as required. Moreover, the NO_3^- and CO_3^- ions react with the benzoic acid according to,

$$NO_3^- + C_6H_5COOH \longleftrightarrow HNO_3 + C_6H_5COO^- \qquad (2.9)$$

$$CO_3^- + 2(C_6H_5COOH) \longleftrightarrow H_2CO_3 + 2C_6H_5COO^- \qquad (2.10)$$

with the nitric and carbonic acids boiling away. This further reduces the hydrogen concentration in the benzoic acid melt. Notice that the first effect is missing when, for example, KNO_3 is used since K ions do not affect the equilibrium. Extensive characterizations have been performed for the various cuts of $LiNbO_3$. These studies reveal:

- Buffering (sometimes referred to as dilution) slows the PE process by as much as ten times depending on the particular cut of the substrate. The resulting index profiles are step-like (as in the case of PE in pure benzoic acid) but with an extraordinary refractive-index change, Δn_e, which depends on $Li\,\%$ according to a Fermi-type function. This dependency allows for considerable flexibility in terms of birefringence control [29,32].

- Some controversy exists in the literature as to the particular $Li\,\%$ at which stable guides result (i.e. index instabilities disappear). Quoted values range from $2.4 - 3.4\,\%$ with a corresponding range in Δn_e of $0.11 - 0.01$ [46].

- Strong buffering eliminates the etching of y-cut substrates indicating a considerable reduction in the lattice strain within the waveguide layer [28].

- IS studies show that hydrogen bonded OH groups are present to a lesser extent (x-cut) with increase in $Li\,\%$ while free OH groups are unaffected. Interaction with ambient water vapour occurs only for elevated temperatures ($T > 300^oC$) [46].

- Waveguides generally exhibit low propagation loss, restored electro-optic effect and room temperature stability [29,32,46].

2.2.4 Use of annealing

An alternative method to decrease the hydrogen concentration within the waveguide layer is to use the annealed PE technique (APE) or, as is sometimes referred to in the literature, the two-step proton-exchange process (TSPE) [61]. This technique consists of performing an initial exchange in pure benzoic acid and then annealing (i.e. heating outside a source of ions) the resulting waveguide. This heating is, in addition, performed in the presence of flowing oxygen to prevent deoxidization of the waveguide surface. The possibility that annealing may be associated with the improvement of the optical properties of PE waveguides was first suggested from observations [61] that these waveguides were found to be more stable when

- they were cooled slowly after the exchange
- a higher initial exchange temperature was used

In addition to reducing the hydrogen concentration and, hence, the refractive index, the annealing process results in an increase in the depth of the waveguides and, if the temperature is high enough, a change in the shape of the index profile from a step to a graded-index one. The majority of annealing studies to date have concentrated on improving waveguide loss and restoring the electro-optic coefficients [30,31,32,33]. Recently, various groups have attempted to model the annealing process by numerical as well as analytical methods [54,56]. As of yet, however, very little work has been done to accurately correlate a wide range of fabrication conditions with measured refractive index profiles. This need to better understand the anneal process resulted in the second phase of this thesis research. In particular, an extensive characterization of annealed PE waveguides in z-cut $LiNbO_3$ is presented in Chapter 5. Conclusions from the various published reports can be summarized as follows:

- In addition to the annealing temperature and time, the modification of the index profile is slightly dependent on the annealing environment [19].

- Goto and Yip [54] have shown that the anneal process is also dependent on the initial PE depth of the waveguide. In particular, measurements with thin and thick waveguides have revealed discrepancies in the shape of the index profile.

- Low temperature ($T_a = 200 - 250^oC$) annealing results in more stable structures. Profiles retain step nature with small changes in Δn_e and d [3].

- Using double XRD, Gan'shin et. al. [62] have shown that annealing at higher temperatures ($T_a > 300^oC$) results in the Li deficient phases mentioned earlier moving towards the waveguiding region as well as increasing in their volume thus forming interpenetrating lattices of $Li_{1-x}H_xNbO_3$ and $LiNb_3O_8/Nb_2O_5$. These new phases may contribute to some scattering within the waveguide layer.

- Recent SIMS results reveal that the mechanisms associated with the anneal process are considerably different from those that drive the initial exchange process. Especially at higher temperatures, the anneal process, as evidenced by the resulting graded-index profiles, seems to be governed by standard diffusion theory [56].

- High temperature ($T_a \geq 500^oC$) annealing results in the clouding of the waveguide surface indicating that substantial surface damage has occurred [62,63].

- Using IS techniques, Loni et. al. [46] have found that annealing results in a reduction of the infrared band at $3250cm^{-1}$ with no change in the band at $3505cm^{-1}$. These observations suggest a removal of hydrogen bonded OH groups (possibly through a surface reaction producing water), diffusion of free OH groups deeper into the substrate, and the possible migration of lithium ions from adjacent regions of the substrate into the waveguide layer. Also, as in the case of buffered melts, waveguides which have been annealed interact with ambient water vapour only at elevated temperatures ($T_a > 300^oC$).

- The fact that the hydrogen bonded OH groups diminish with annealing suggest [46] that they may be associated with some of the problems with PE waveguides (eg. degradation of the electro-optic coefficient). However, as mentioned earlier, these groups have only been found in x-cut $LiNbO_3$. Consequently, this argument can not be used for z-cut waveguides (This has not been clarified in the literature).
- Although propagation loss studies have been carried out, a correlation between fabrication conditions and loss have not been conclusively established. This is further complicated by the fact that x and z-cut waveguides behaved differently under similar fabrication conditions [33].
- Generally, the APE technique results in stable, low loss waveguides with restored electro-optic coefficient suggesting that the physical and chemical properties of the annealed PE layer is more similar to the virgin $LiNbO_3$ than the initial PE waveguide region [32,46].

Recently, it was shown that both the APE and the buffered melt techniques have resulted in high quality waveguides [32]. The APE method, however, offers certain distinct advantages including:

- The fabrication time required is only a few hours compared to several hundred hours using the buffered melt technique [32].
- Although both techniques provide for birefringence control, APE allows for tailoring the mode profile by altering the shape of the index profile [44].

- Since the diffusion coefficient is strongly concentration dependent, the use of buffered melts requires very accurately defined melt composition if reproducibility is to be achieved. This means that the melt must be sealed otherwise melt composition would change during exchange due to differential evaporation of melt constituents. Hence, fabrication complexity is increased [61].

Nevertheless, it is clear that a combination of the APE and buffered melt techniques allows for considerable flexibility in the optimization of waveguide characteristics for a variety of IO applications.

2.2.5 Origin of the index change

Although a great deal has been said about the characteristics of both the concentration and refractive index profiles in PE waveguides, the exact relationship between these two important parameters has not as of yet been addressed. Annealing studies [21] on PE refractive index profiles have revealed one interesting common feature: the area under the index versus depth curves for APE wavegides is greater than that for the initial PE waveguides. This phenomenon of the area not being conserved has been attributed to a nonlinear dependence of the extraordinary index of refraction on the hydrogen concentration. Initial work [64] with deuterium revealed a concentration dependence which is approximately linear for $x < 0.20$ but shows saturation for $x > 0.30$. Later work [65] confirmed this saturation phenomenon. Recently, Howerton et al. [20] have found discrepancies between deuterium and hydrogen studies. Based on their ERDA observations, the following simple empirical relationship between the refractive index and concentration profiles is proposed,

$$\Delta n_e(x) = \alpha_1 \left(1 - \exp(-\alpha_2 \, x^{\alpha_3})\right) \tag{2.11}$$

where

x = normalized (i.e. fractional) concentration ($0 < x < 1$)
$\Delta n_e(x)$ = extraordinary refractive index change
$\alpha_1, \alpha_2, \alpha_3$ = fitting parameters

Note that x (as in $Li_{1-x}H_xNbO_3$) is not to be confused with the transverse or depth coordinate to be discussed later. Using a least squares procedure, one finds that $(\alpha_1, \alpha_2, \alpha_3) = (0.1317, 3.4576, 1.75)$. Although an empirical relationship has been previously reported for the deuterium data, this is the first time that any such relationship has been proposed for the hydrogen data. The above equation with the latter parameters is sketched in Fig. 2.3. The deuterium curve along with the α phase region (i.e. $x \leq 0.12$) are also shown for reference. Comparison of these curves shows significant differences in the predicted index increases in the α phase region as well as the saturation regions. It is important to realize that published studies have so far exclusively focused on the extraordinary refractive index. Similar work to understand the relationship between the reported negative ordinary index change and hydrogen concentration has not as of yet been undertaken.

Although this nonlinear dependence of index on concentration has also been observed [18] in $Ti:LiNbO_3$ waveguides, it is absent by contrast in ion-exchanged glass waveguides. This fact suggests that the mechanisms of index change in PE and ion-exchanged waveguides are different. Generally, the net index of refraction will depend on the following contributions [8,47]:

1. a difference in the polarizability of the two exchanging ions
2. changes in the stress state caused by ionic size difference
3. a change in molar volume or density

4. changes in the polarization of the crystal due to differential site preference of the exchanging ions in the lattice
5. a change in the lattice parameters due to a phase change

In PE waveguides, IS studies [66] have shown that the differences in site preference of H and Li may result in polarizability changes of the neighbouring oxygen atoms. In addition, as mentioned earlier, XRD analysis [50] has revealed considerable straining of the lattice resulting in lattice constant changes. Hence, the last three effects seem to be predominant in PE [8]. Although much work has been done to model all of the above effects in ion-exchanged glass waveguides, a corresponding effort in PE in lithium niobate is still lacking.

2.3 Modeling the PE process

2.3.1 The nonlinear diffusion equation

Although the PE process is quite complex and not characterized by a simple one for one ion-exchange, the various mathematical models that have been proposed to describe this process are based on the ion-exchange equations. These equations reflect the fact that, in the ion-exchange process, the driving force behind the ionic flux consists of the concentration gradient of the ionic species and the gradient of the local electric potential which arises due to the generally unequal mobilities of the indiffusing and outdiffusing ions. This intrinsic electric field has the effect of equalizing the fluxes of the two ions and, hence, maintaining charge neutrality. This phenomenon results in the diffusion equation being nonlinear [67],

$$\frac{\partial \hat{c}}{\partial t} = \vec{\nabla} \cdot \left(\frac{D_H}{1 - \alpha \hat{c}} \vec{\nabla} \hat{c} \right) \tag{2.12}$$

where,

$$\hat{c} = \frac{c_H}{c_o} \tag{2.13}$$

$$\alpha = 1 - \frac{D_H}{D_{Li}} \tag{2.14}$$

and

c_H = concentration of indiffusing H ions in the $LiNbO_3$ crystal (2.15)

D_H = self-diffusion coefficient of H (2.16)

D_{Li} = self-diffusion coefficient of out-diffusing Li (2.17)

c_o = total concentration of diffusing ions (2.18)

Note that in the derivation of the above equation, the electroneutrality requirement has been invoked, namely,

$$c_H + c_{Li} = c_o \tag{2.19}$$

As will be seen in Chapter 4, the $LiNbO_3$ substrates used have approximate dimensions of $5\,mm$ by $25\,mm$ by $1\,mm$ and, hence, a corresponding surface area of about $1\,cm^2$. In addition, the PE process results in a diffusion layer which extends not more than a few microns into the substrate. Consequently, one can make the reasonable assumption that this process is one-dimensional. Taking x as the depth direction (as is usually done in the literature), the above equation reduces to,

$$\frac{\partial \hat{c}}{\partial t} = \frac{\partial}{\partial x}\left(\frac{D_H}{1 - \alpha\hat{c}}\frac{\partial \hat{c}}{\partial x}\right) \tag{2.20}$$

This nonlinear partial differential equation which has been applied successfully to describe ion-exchange in glass waveguides [68,69,70] is used to model the PE process for slab (i.e. planar) waveguides.

2.3.2 Case I: Infinite melt volume assumption

As this is a parabolic equation, a well-posed problem consists of specifying one Cauchy (i.e. initial) and two boundary conditions. Since the concentration of H ions in the slab is initially zero, the Cauchy condition becomes,

$$\hat{c}(x, 0) = 0 \tag{2.21}$$

As for the boundary conditions, since $d \ll d_t$ where d is the diffusion depth and d_t is the thickness of the $LiNbO_3$ slab, this yields the following boundary condition,

$$\lim_{x \to \infty} \hat{c}(x,t) = 0 \tag{2.22}$$

Moreover, if one assumes that the melt volume is large enough (i.e. effectively infinite) so that the effect of the outdiffusing Li ions is negligible, then a constant supply of H ions will exist at the surface of the crystal resulting in the following boundary condition [69],

$$\hat{c}(0,t) = \hat{c}_s \tag{2.23}$$

The value of $\hat{c}_s$ above represents the fraction of H ions which are effectively exchanging with the Li ions at the surface. As mentioned earlier, for PE in benzoic acid, various microanalytical measurements have revealed that $\hat{c}_s = 0.65 - 0.80$. With the formulation of the problem now complete, one proceeds to solve the diffusion equation by noting that the solution of a nonlinear partial differential equation is usually simplified if it can be transformed into an ordinary differential equation. To this end, the following *similarity* variable (also known as the Boltzmann transformation) is introduced [71],

$$\gamma = \frac{x}{2\sqrt{D_H t}} \tag{2.24}$$

so that,

$$\frac{\partial}{\partial x} = \frac{\partial}{\partial \gamma}\frac{\partial \gamma}{\partial x} = \frac{1}{2\sqrt{D_H t}}\frac{\partial}{\partial \gamma} \tag{2.25}$$

$$\frac{\partial}{\partial t} = \frac{\partial}{\partial \gamma}\frac{\partial \gamma}{\partial t} = -\frac{x}{4\sqrt{D_H t^3}}\frac{\partial}{\partial \gamma} \tag{2.26}$$

In applying the chain rule above, the hydrogen self-diffusion coefficient is assumed *constant*. Eq. 2.20 reduces to the following nonlinear ordinary differential equation,

$$-2\gamma\frac{d\hat{c}}{d\gamma} = \frac{d}{d\gamma}\left(\frac{1}{1-\alpha\hat{c}}\frac{d\hat{c}}{d\gamma}\right) \tag{2.27}$$

This transformation will work only when two of the auxiliary conditions (i.e. one boundary and one initial condition) can be consolidated into one. Consequently, since both $t = 0$ and $x \rightarrow \infty$ correspond to $\gamma \rightarrow \infty$, this requires,

$$\hat{c}(x,0) = \lim_{x \rightarrow \infty} \hat{c}(x,t) \tag{2.28}$$

Fortunately, this consolidation condition is fulfilled in the PE case. This transformation, however, can not be used for a nonzero initial concentration distribution, for example, in analyzing the *annealing* or *backdiffusion* processes. For the transformed equation, the appropriate boundary conditions become,

$$\hat{c}(\gamma = 0) = \hat{c}_s \tag{2.29}$$

$$\lim_{\gamma \rightarrow \infty} \hat{c}(\gamma) = 0 \tag{2.30}$$

Keeping the above boundary conditions in mind, one proceeds to solve Eq. 2.27. First, the following convenient normalization is introduced,

$$c = \frac{\hat{c}}{\hat{c}_s} \tag{2.31}$$

so that Eq. 2.27 becomes,

$$-2\gamma \frac{dc}{d\gamma} = \frac{d}{d\gamma}\left(\frac{1}{1 - \hat{\alpha} c} \frac{dc}{d\gamma}\right) \tag{2.32}$$

$$c(\gamma = 0) = 1 \tag{2.33}$$

$$\lim_{\gamma \rightarrow \infty} c(\gamma) = 0 \tag{2.34}$$

$$\hat{\alpha} = \alpha \hat{c}_s \tag{2.35}$$

Analytic solutions

Analytic solutions to the above problem come in one of two forms. The first of these is a parametric solution derived in Crank [72] and given below,

$$\gamma(\theta) = -\frac{1}{\sqrt{2\mu}}(\theta - (\theta^2 - \mu \ln \theta^2)^{\frac{1}{2}}) \exp\left(\int_0^\theta (\phi^2 - \mu \ln \phi^2)^{-\frac{1}{2}} d\phi\right) \tag{2.36}$$

$$c(\theta) = \frac{1}{\hat{\alpha}}\left(1 - \exp\left(-2\int_0^\theta (\phi^2 - \mu \ln \phi^2)^{-\frac{1}{2}} d\phi\right)\right) \tag{2.37}$$

where μ is found by solving,

$$\ln(1-\hat{\alpha}) + 2\int_0^1 (\phi^2 - \mu \ln \phi^2)^{-\frac{1}{2}} d\phi = 0 \tag{2.38}$$

The other analytic form of the solution consists of using a Taylor series expansion near $\gamma = 0$ of the above parametric solution,

$$c(\gamma) = \sum_{k=0}^{\infty} \frac{c^{(k)}(0)}{k!}\gamma^k \tag{2.39}$$

Note that the chain rule is invoked to evaluate the derivatives (i.e. the Taylor coefficients),

$$\frac{dc}{d\gamma} = \frac{dc}{d\theta}\left(\frac{d\gamma}{d\theta}\right)^{-1} \tag{2.40}$$

This yields the following result [68,73],

$$c(\gamma) = 1 + \left(\frac{-2\sqrt{2}}{\hat{\alpha}\sqrt{\mu}}(1-\hat{\alpha})^{\frac{3}{2}}\right)\gamma + \left(\frac{-4}{\hat{\alpha}\mu}(1-\hat{\alpha})^2\right)\gamma^2 + \left(\frac{2\sqrt{2}}{3\hat{\alpha}\mu\sqrt{\mu}}(1-\hat{\alpha})^{\frac{5}{2}}(\mu-4)\right)\gamma^3 + \cdots \tag{2.41}$$

As pointed out elsewhere [74], the convergence properties of this series as well as the effect of the higher order terms (which become increasingly tedious to evaluate) are difficult to assess and, hence, restrict its usefulness. Nevertheless, numerous investigators [68,69] have used the first three terms of this series (i.e. 2nd order polynomial) as an analytic model for the concentration profile. For PE, however, the profile (as mentioned previously) is approximately a step function and, consequently, this truncated series approximation is not a valid one.

The rather inconvenient form of the parametric solution as well as the problems inherent in the series solution compel one to look for an alternative, in particular, an efficient numerical technique employing a fourth order Runge-Kutta scheme with shooting.

Numerical solution

In order to solve the diffusion equation numerically, some preliminary analytic manipulations are required. First, upon expanding Eq. 2.32, one obtains,

$$-2\gamma\frac{dc}{d\gamma} = \frac{1}{1-\hat{\alpha}c}\frac{d^2c}{d\gamma^2} + \frac{\hat{\alpha}}{(1-\hat{\alpha}c)^2}\left(\frac{dc}{d\gamma}\right)^2 \tag{2.42}$$

To use the proposed fourth order Runge-Kutta scheme, one must express the above equation as a system of first order equations as follows,

$$\frac{dc}{d\gamma} = g \tag{2.43}$$

$$\frac{dg}{d\gamma} = -2g\gamma(1-\hat{\alpha}c) - \frac{\hat{\alpha}g^2}{(1-\hat{\alpha}c)} \tag{2.44}$$

To facilitate computation purposes, the following transformation is introduced [73],

$$\rho = \frac{\gamma}{1+\gamma} \Longleftrightarrow \gamma = \frac{\rho}{1-\rho} \tag{2.45}$$

$$\longrightarrow \quad \frac{d}{d\gamma} = \frac{d}{d\rho}\frac{d\rho}{d\gamma} = (1-\rho)^2\frac{d}{d\rho} \tag{2.46}$$

This brings the domain to a more practical form,

$$\gamma \in (0,\infty) \Longleftrightarrow \rho \in (0,1) \tag{2.47}$$

With this transformation, the first order system becomes,

$$\frac{dc}{d\rho} = F(\rho,g) = \frac{g}{(1-\rho)^2} \tag{2.48}$$

$$\frac{dg}{d\rho} = G(\rho,g,c) = -2g(1-\hat{\alpha}c)\frac{\rho}{(1-\rho)^3} - \frac{\hat{\alpha}g^2}{(1-\hat{\alpha}c)(1-\rho)^2} \tag{2.49}$$

$$c(\rho=0) = 1 \tag{2.50}$$

$$c(\rho=1) = 0 \tag{2.51}$$

To solve the above system, the following fourth-order Runge-Kutta scheme is used,

$$c_1 = c_o + \frac{1}{6}(k_1 + 2k_2 + 2k_3 + k_4) \tag{2.52}$$

$$g_1 = g_o + \frac{1}{6}(l_1 + 2l_2 + 2l_3 + l_4) \tag{2.53}$$

$$k_1 = hF(\rho_o, g_o) \tag{2.54}$$

$$l_1 = hG(\rho_o, g_o, c_o) \tag{2.55}$$

$$k_2 = hF(\rho_o + \frac{h}{2}, g_o + \frac{l_1}{2}) \tag{2.56}$$

$$l_2 = hG(\rho_o + \frac{h}{2}, g_o + \frac{l_1}{2}, c_o + \frac{k_1}{2}) \tag{2.57}$$

$$k_3 = hF(\rho_o + \frac{h}{2}, g_o + \frac{l_2}{2}) \tag{2.58}$$

$$l_3 = hG(\rho_o + \frac{h}{2}, g_o + \frac{l_2}{2}, c_o + \frac{k_2}{2}) \tag{2.59}$$

$$k_4 = hF(\rho_o + h, g_o + l_3) \tag{2.60}$$

$$l_4 = hG(\rho_o + h, g_o + l_3, c_o + k_3) \tag{2.61}$$

where (c_1, g_1) are the values of (c, g) after a step size of h has been taken. This scheme is popular because each k and l is only explicitly dependent on the previous k and l. Furthermore, the associated truncation error is $\sim h^5$ [75] and, as a result, for $h = 0.01$, one expects around 8 significant figures for the result which is adequate for the task at hand. Note also that at the first step,

$$c_o = c(\rho_o) = c(\rho = 0) = 1 \tag{2.62}$$

$$g_o = g(\rho_o) = g(\rho = 0) = ?? \tag{2.63}$$

Similarly, at the last step,

$$c_f = c(\rho_f) = c(\rho = 1) = 0 \tag{2.64}$$

$$g_f = g(\rho_f) = g(\rho = 1) = ?? \tag{2.65}$$

Since Eq. 2.62 and Eq. 2.64 constitute a *2-point* boundary condition, the so-called *shooting* technique will have to be used in conjunction with Eq. 2.52 and Eq. 2.53. In essence, this technique involves adjusting the starting value of g or g_o so that the boundary condition at the other end is satisfied (i.e. shooting for $c(\rho_f) = 0$) as illustrated in Fig. 2.4. Note that from Eq. 2.48,

$$\left.\frac{dc}{d\rho}\right|_{\rho=0} = g_o \tag{2.66}$$

Table 2.2: Guesses to be used for g_o for various values of $\hat{\alpha} = \alpha\hat{c}_s$.

$\hat{\alpha}$	g_o
-100.0	-16.670
-10.0	-5.011
-1.0	-1.787
0.0	-1.128
0.33	-0.855
0.75	-0.416
0.95	-0.115
0.99	-0.029
0.999	-0.36×10^{-2}
0.9999	-0.42×10^{-3}
$1 - 10^{-6}$	-0.52×10^{-5}
$1 - 10^{-9}$	-0.64×10^{-8}

Furthermore, since $c_o > c_f$, this suggests that $g_o < 0$. This shooting technique will result in a root search of the form,

$$R(g_o) = (\text{value obtained for } c_f \text{ after guessing for } g_o) - c_f(= 0) \; = \; 0 \qquad (2.67)$$

To perform this root search, the familiar Secant method was employed. Table 2.2 summarizes the appropriate guesses to be used for g_o for various values of $\hat{\alpha}$. Note that these guesses were arrived at strictly by trial and error. In addition, it was found that for $\hat{\alpha}$ values close to 1 as well as for large negative values, the selection of the initial guesses was critical in terms of the convergence of the root searching technique. The value of $\rho = 0.8$ was found to suffice since for all practical purposes, the normalized concentration, c, decays rapidly to 0 for $\rho > 0.8$ (i.e. $\gamma > 4$). One important question to be asked concerns the validity and accuracy of the above numerical scheme. In Fig. 2.5, a comparison between the numerical solutions obtained using the Runge-Kutta shooting technique and a 3-level implicit finite difference method (to be discussed later) shows excellent agreement. Although this latter technique is more flexible in that it can handle annealing or backdiffusion problems, a tradeoff exists because the computing time necessary for comparable accuracy is relatively large. A typical simulation run on an IBM AT compatible requires $1 - 10$ *hrs* of computing time (depending on the value of $\hat{\alpha}$) compared to less than 30 seconds for the Runge-Kutta shooting technique.

The only free parameter in the above diffusion model is $\hat{\alpha}$. Note that in the special case of $\hat{\alpha} = 0$, the self-diffusion coefficients of Li and H are equal and the diffusion equation becomes linear which results in an analytic solution in the form of a complimentary error function. The effect of $\hat{\alpha}$ on the normalized concentration profile is shown in Fig. 2.6. The profile is graded for small values of $\hat{\alpha}$ and approaches a step for $\hat{\alpha} \approx 1$. One could also try negative values of $\hat{\alpha}$ arguing that H is smaller than Li and, hence, should have a correspondingly larger self-diffusion coefficient. From Fig. 2.7, one sees that negative values of $\hat{\alpha}$ do not lead to step profiles which suggests more complex mechanisms at work. Although $\hat{\alpha} = 0.999$ has been used by Clark et. al. [22] and recently by Goto and Yip [54] to model the PE process, the associated profile (see Fig. 2.6) is characterized by a very distinct tail. This phenomenon has not been observed in the measured concentration profiles [56]. This suggests that one might try $\hat{\alpha}$ values in the range $0.999 < \hat{\alpha} < 1$. This situation is illustrated in Fig. 2.8. Although the shape of the concentration profile becomes increasingly sharp (i.e. step-like) as $\hat{\alpha}$ approaches 1, the resulting ratio of the self-diffusion coefficients is relatively large with $\frac{D_{Li}}{D_H} \gg 1000$. From a physical point of view, it is difficult to explain why there should be such a large disparity between these coefficients. Note also that the electroneutrality requirement predicts that the Li profile is an exact compliment of the H profile. The measured H and Li profiles, however, have not been found to be complimentary. These results clearly reveal some difficiencies in this model [56].

In the above discussion, one must not forget that the single free parameter, $\hat{\alpha}$, is really a product of two quantities, specifically, α and $\hat{c}_s$. In the past [22,54], studies have focused on the determination of $\hat{\alpha}$ while implicitly assuming $\hat{c}_s = 1$.

Recently, Nikolopoulos and Yip [34] studied the effect of $\hat{c}_s$ on the profile keeping $\alpha = 0.999$. Since $\hat{\alpha} = \alpha\hat{c}_s$, the curves in Fig. 2.6 can also describe this effect if α is assumed constant. For a profile as close to a step as possible, one needs $\hat{\alpha} \approx 1$ which requires that both α and $\hat{c}_s \approx 1$. However, for PE in benzoic acid, the values of $\hat{c}_s$ quoted have been in the range $0.65 < \hat{c}_s < 0.80$ which result in graded concentration profiles. In addition, as mentioned previously, studies involving buffered melts have shown that $\hat{c}_s$ can be reduced while allowing the profiles to retain their step nature. This contradicts with theory which again predicts graded profiles. These points have never been clarified in the literature. These results conclusively show that the ion-exchange model (with the assumption of constant self-diffusion coefficients) is inadequate as far as describing the PE process is concerned. This does not imply, however, that one must reject this model altogether. In fact, by keeping the basic structure of the model intact and only changing some assumptions that have been made, in particular, infinite source and constant self-diffusion coefficients, Vohra and Mickelson [58,56] have recently shown that better insight can thus be gained about the PE process.

2.3.3 Case II: Finite melt volume assumption

Previously, while discussing the details of waveguide formation, it was mentioned that infrared spectroscopy (IS) studies suggested the possibility of a melt-dilution effect occuring in PE waveguides. These studies consisted of observing the infrared absorption frequencies associated with the formation of free and hydrogen bonded hydroxyl groups within the PE waveguide layer. By recording the time evolution of the free OH peak in z-cut waveguides, Vohra and Mickelson [58] concluded that a saturation effect was taking place. Later, by considering both absorption bands as well as the area of the latter as opposed to the peak height in determining the overall rate of PE, Loni et al. [46] found no evidence for such saturation. Some controversy, however, still remains. For z-cut $LiNbO_3$, the hydrogen bonded band is absent and, moreover, if a correction is made for band area, the resulting curves continue to show [76] some saturation (for volumes of about 50 ml). Furthermore, recent experiments with spin and surface coated pyrophosphoric acid samples (where the amount of acid used is typically $0.1ml$) have resulted in diffusion coefficients smaller than expected thus suggesting melt-dilution effects [77]. Finally, it was also observed that the etching of y-cut $LiTaO_3$ crystal took much longer in a 'used' melt thus again supporting the contention that the outdiffusing Li is diluting the melt [58].

As a first attempt, this saturation phenomenon has been modeled using the standard diffusion equation (i.e. $\alpha = 0$) and a boundary condition which takes into account the time-independent nature of the total amount of hydrogen in the melt and crystal. Following Vohra and Mickelson [58], one assumes a $LiNbO_3$ slab occupying the space $0 \leq x < \infty$ with the melt occupying $x < 0$. The concentration of H in the slab is described by

$$\frac{\partial c}{\partial t} = D_H \frac{\partial^2 c}{\partial x^2} \tag{2.68}$$

The amount of free protons between x and ∞ is defined by

$$y(x,t) = \int_x^\infty c(\xi,t)d\xi \tag{2.69}$$

With this transformation, the PDE becomes,

$$\frac{\partial y}{\partial t} = D_H \frac{\partial^2 y}{\partial x^2} \tag{2.70}$$

The corresponding boundary and initial conditions are:

$$\begin{aligned} y(x,0) &= 0 && (2.71) \\ y(0,t) + \frac{l}{k}\left[\frac{dy}{dx}\right]_{x=0} &= y_o && (2.72) \\ \lim_{x\to\infty} y(x,t) &= 0 && (2.73) \end{aligned}$$

where

$y(0,t)$ = total amount of protons in the slab

l = size of the bath

y_o = total amount of protons in the system (melt + slab)

k = partition factor

The partition factor, k, reflects the fact that the concentration of hydrogen at the surface of the crystal is k times that in the melt [58]. Note that Eq. 2.72 constitutes a boundary condition of the third kind (also known as a Robin condition). The solution of the above PDE with these new BCs is obtained by using the Laplace Transform (LT) technique yielding [78],

$$y(x,t) = y_o\left\{erfc\left(\frac{x}{2\sqrt{D_H t}}\right) - \exp\left(-\frac{x}{\gamma\sqrt{D_H}}\right)\exp\left(\frac{t}{\gamma^2}\right)erfc\left(-\frac{\sqrt{t}}{\gamma}+\frac{x}{2\sqrt{D_H t}}\right)\right\} \tag{2.74}$$

where

$$erfc\,x = \frac{2}{\sqrt{\pi}}\int_x^\infty e^{-u^2}du \tag{2.75}$$

$$\gamma = \frac{l}{k\sqrt{D_H}} \tag{2.76}$$

Now, the total amount of hydrogen in the $LiNbO_3$ slab is found by evaluating the above expression at $x = 0$. Taking $y(t) \equiv y(0,t)$ and noting that $erfc(0) = 1 - erf(0) = 1$, one obtains the result [58],

$$y(t) = y_o\left\{1 - \exp\left(\frac{k^2}{l^2}D_H t\right) erfc\left(\frac{k}{l}\sqrt{D_H t}\right)\right\} \tag{2.77}$$

Note that the application of *l'Hôpital's Rule* leads to $\lim_{t\to\infty} y(t) = y_o$ (i.e. saturation) as expected. The degree of saturation increases as the volume of the melt decreases. Although this model is successful in taking account the finite nature of the melt, the resulting concentration profiles are not step [72]. This, however, is not surprising considering the simplicity of the mathematical model (i.e. linear diffusion). Of course, the reason for using such a simple model lies with the convenient analytical solution which can be easily obtained thus allowing one to readily assess the effect of altering the boundary condition at $x = 0$. The information thus gained allows one to better understand one aspect of the PE process, specifically, diffusion from a melt of finite volume. The implication here is that once an adequate model is found, its generalization to include the effects of finite melts may be accomplished by a simple alteration of the appropriate boundary condition.

2.3.4 Case III: Concentration dependent self-diffusion coefficient

In the nonlinear diffusion model considered earlier, one important assumption was made: the self-diffusion coefficients are independent of concentration (i.e. constant). In other words, no interaction between the two counter diffusing ions is assumed to occur. This results in complimentary H and Li concentration profiles with characteristic tails. The experimentally observed step-index profiles led Rice et. al. [64] to propose concentration dependent self-diffusion coefficients. This interesting idea was further investigated very recently by Vohra and Mickelson [56].

The concept of concentration dependent self-diffusion coefficients is not new. It is well known [79,80] that ion-exchange in glass involving alkali ions results in an interaction between the indiffusing and outdiffusing ions. This phenomenon is usually referred to as the *double-alkali* effect. This effect which increases as the size difference between the exchanging ions increases results in changes in the shape of the index profile. For example, in $K - Na$ exchange, the ions are of similar size yielding negligible interaction and thus smooth graded-index profiles. In $Cs - Na$ exchange, however, the ionic size difference is appreciable resulting in strong interaction and, hence, step-index profiles.

Based on these observations, Vohra and Mickelson [56] proposed the following model for PE. Initially, due to the high Li concentration, the hydrogen self-diffusion coefficient is small compared to that of lithium (i.e. $D_H \ll D_{Li}$). Due to the large concentration gradient between the melt and $LiNbO_3$ crystal, hydrogen begins to slowly accumulate in the surface layer (The latter may be enhanced through a surface chemical reaction). The hydrogen concentration increases until a certain critical concentration is attained at which time $D_{Li}(c_t) = D_H(c_t)$, thus allowing the actual ion-exchange to occur. This results in a sharp (i.e. step-like) diffusion front which propagates into the substrate according to a square root time behaviour. The mathematical model describing the above mechanism is given by the following equation,

$$\frac{\partial c_H}{\partial t} = \frac{\partial}{\partial x}\left(\frac{D_H(c_{Li})}{1-\alpha c_H}\frac{\partial c_H}{\partial x}\right) \tag{2.78}$$

where

$$\alpha = 1 - \frac{D_H(c_{Li})}{D_{Li}(c_H)} \tag{2.79}$$

All the parameters in the above model have been defined before. Notice the explicit dependence of the self-diffusion coefficients on concentration. Using a suitable choice of the above parameters, this model can readily yield step concentration profiles. In addition, by assuming different concentration dependencies of the self-diffusion coefficients, one finds that the resulting H and Li profiles are not compliments of each other. Based on SIMS data, Vohra and Mickelson [56] have sketched these dependencies and have obtained good agreement between theory and experiment. However, much work remains in order to independently confirm these results as well as analyzing the effects of diffusion temperature and time. Due to the very recent nature of these developments (Jan '90), these topics were not explored.

2.4 Modeling the annealing process

As emphasized earlier, the annealing process is a necessary step in the fabrication of high quality waveguides. Hence, it is desirable to be able to mathematically model such a process. Two distinct diffusion models have been recently reported in the literature [54,56].

2.4.1 Analytic model

Recent SIMS data has shown [56] that the mechanisms driving the anneal process are significantly different from those associated with the initial PE. The former, as evidenced by the graded profiles especially at higher anneal temperatures, seem to be governed by standard diffusion theory. As such, the anneal process is modeled by considering the diffusion of an initial impurity (i.e. hydrogen) distribution occupying the space $0 \leq x \leq d$ in a semi-infinite slab,

$$\frac{\partial c_H}{\partial t} = D_{H_a} \frac{\partial^2 c_H}{\partial x^2} \tag{2.80}$$

$$\begin{aligned} c_H(x,0) &= f(x) && (2.81) \\ \left.\frac{\partial c_H}{\partial x}\right|_{x=0} &= 0 && (2.82) \\ \lim_{x \to \infty} c_H(x,t) &= 0 && (2.83) \end{aligned}$$

The Neumann boudary condition at $x = 0$ expresses the fact that there is no ionic flux across the surface of the waveguide which is what one expects in the case of heating outside a source of ions. Using the standard Fourier cosine transform technique [81], one can readily derive the analytic solution to the above problem,

$$c_H(x,t) = \sqrt{\frac{\pi}{4D_{H_a}}} \int_0^\infty f(\xi) \left[\exp\left\{ -\frac{(\xi + x)^2}{4D_{H_a}t} \right\} + \exp\left\{ -\frac{(\xi - x)^2}{4D_{H_a}t} \right\} \right] d\xi \tag{2.84}$$

If one assumes (as a first approximation) that the initial PE results in a step concentration profile, then

$$f(x) = \begin{cases} c_s & 0 \leq x \leq d \\ 0 & x > d \end{cases}$$

and

$$c_H(x,t) = c_s \left[erf\left\{ \frac{(d - x)}{2\sqrt{D_{H_a}t}} \right\} + erf\left\{ \frac{(d + x)}{2\sqrt{D_{H_a}t}} \right\} \right] \tag{2.85}$$

where

$$erf\, u = \frac{2}{\sqrt{\pi}} \int_0^u e^{-s^2} ds \tag{2.86}$$

The effect of the anneal time, t_a, on the concentration profile for a given initial depth, d, and anneal diffusion coefficient, D_{H_a}, is shown in Fig. 2.9. As expected, the surface concentration decreases as t_a increases and the profile shape changes from step to Gaussian. In Fig. 2.10, the change in the surface concentration versus anneal time is plotted for various initial depth values. This plot reveals that thinner waveguides behave differently than their thicker counterparts for a given anneal time and diffusion coefficient. The recent results of Goto and Yip [54] are consistent with this theoretical prediction. Note that if one models the initial Li depletion profile as a step, then

$$f(x) = \begin{cases} 0 & 0 \leq x \leq d \\ c_{Li_s} & x > d \end{cases}$$

and one obtains [56],

$$c_{Li} = c_{Li_s} \left[erfc \left\{ \frac{(d-x)}{2\sqrt{D_{Li_a} t}} \right\} + erfc \left\{ \frac{(d+x)}{2\sqrt{D_{Li_a} t}} \right\} \right] \tag{2.87}$$

where $erfc\, u = 1 - erf\, u$. Vohra and Mickelson [56] fitted their SIMS data to the above two equations and found $D_{H_a} = 0.77$ and $D_{Li_a} = 0.45 \frac{\mu m^2}{hr}$ for $T_a = 360^o C$.

2.4.2 Numerical solution

Although the above model is attractive in that it is simple (i.e. D_{H_a} is the only free parameter) and an analytic solution is available, it does neglect the fact that the mobilities of the indiffusing and outdiffusing ions are unequal. The fact that $D_{H_a} > D_{Li_a}$ suggests that one might try solving the nonlinear diffusion equation for $\hat{\alpha} < 0$,

$$\frac{\partial c}{\partial t} = \frac{\partial}{\partial x}\left(\frac{D_{H_a}}{1 - \hat{\alpha} c} \frac{\partial c}{\partial x} \right) \tag{2.88}$$

$$\begin{aligned} c(x,0) &= f(x) && (2.89) \\ \left.\frac{\partial c}{\partial x}\right|_{x=0} &= 0 && (2.90) \\ \lim_{x \to \infty} c(x,t) &= 0 && (2.91) \end{aligned}$$

Unfortunately, due to the nonzero initial concentration distribution, the consolidation condition given by Eq. 2.28 is not satisfied and, hence, one can not use the Runge-Kutta shooting technique described earlier. To solve this diffusion equation numerically, a three-level implicit finite difference method [82] is used, in particular,

$$\begin{aligned} c_m^{n+1} - c_m^{n-1} = \frac{2r}{3}\{ & A^+ \left[(c_{m+1}^{n+1} - c_m^{n+1}) + (c_{m+1}^{n} - c_m^{n}) + (c_{m+1}^{n-1} - c_m^{n-1}) \right] \\ & -A^- \left[(c_m^{n+1} - c_{m-1}^{n+1}) + (c_m^{n} - c_{m-1}^{n}) + (c_m^{n-1} - c_{m-1}^{n-1}) \right] \} \end{aligned} \qquad (2.92)$$

where

$$A^+ = \frac{D_{H_a}}{1 - \frac{\hat{\alpha}}{2}(c_{m+1}^n + c_m^n)} \qquad (2.93)$$

$$A^- = \frac{D_{H_a}}{1 - \frac{\hat{\alpha}}{2}(c_m^n + c_{m-1}^n)} \qquad (2.94)$$

$$r = \frac{k}{h^2} \text{ (mesh ratio)} \qquad (2.95)$$

$$(x_m, t_n) = (mh, nk) \qquad (2.96)$$

$$c_m^n = c(mh, nk) \qquad (2.97)$$

The details of the matrix formulation of this difference equation including the treatment of the boundary and initial conditions are given elsewhere [83]. Note that the implicit nature of this numerical scheme requires the inversion of a tridiagonal system at every time step and, hence, is very computationally intensive. Although such a scheme generally results in unconditionally stable solutions in cases of linear parabolic problems (and, hence, motivates its use here), the nonlinear nature of this particular diffusion problem resulted in conditional stability. It was found that the value of the mesh ratio, r, had to be decreased as $\hat{\alpha}$ or D_{H_a} increased [83]. It is possible that less computation intensive explicit schemes may result in comparable stability characteristics; this, however, was not investigated.

The effect of $\hat{\alpha}$ on the concentration profile is shown in Fig. 2.11. The value of $\hat{\alpha} = 0.999$ has been previously used by Goto and Yip [54] to model the anneal process. In addition, $\hat{\alpha} = -0.711$ comes from the diffusion coefficients quoted above while $\hat{\alpha} = 0$ corresponds to the analytic solution discussed earlier. This graph shows that as $\hat{\alpha}$ increases (positively), the profile becomes increasingly flat. Note that in this model, there exists two free parameters (i.e. D_{H_a}, $\hat{\alpha}$) and, consequently, an optimizing routine will have to be used in the data fitting.

One final comment concerns the nature of the data used in the modeling of PE and APE waveguides. Two approaches can be distinguished. In the first case, a direct measurement of the concentration profile is feasible and, consequently, one can directly compare this set of data with the appropriate diffusion model. In the second case, a direct measurement of the concentration is not feasible due to, for example, the need for very elaborate and expensive equipment (eg. SIMS). Instead, the refractive index profile is measured using a standard and relatively inexpensive prism coupler setup (see Chapter 4). Now, in order to compare these measured index profiles with theoretical simulations based on the above models, one must be able to convert the theoretical concentration profile to its corresponding refractive index profile. Fortunately, this is readily accomplished by using Eq. 2.11. The presentation of some preliminary diffusion modeling results in Chapter 5 will follow this latter approach.

In concluding, it is clear that although a variety of mathematical models have been proposed to describe the PE (in pure and diluted melts) and APE processes, much work remains in order to conclusively establish their validity as effective design tools.

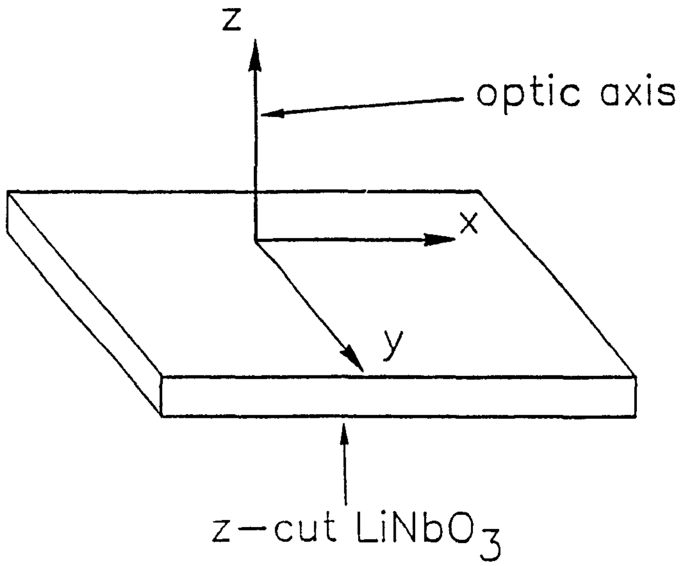

Figure 2.1: Orientation of crystallographic x, y, and z axes for z-cut $LiNbO_3$.

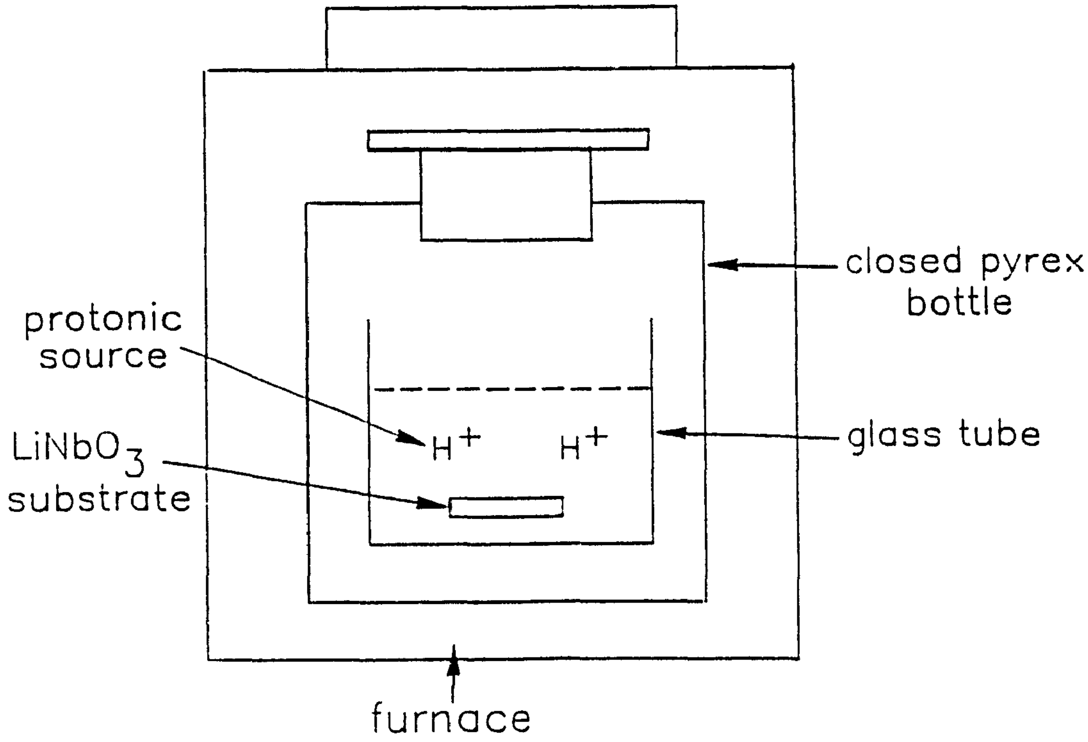

Figure 2.2: Optical waveguide fabrication using proton-exchange.

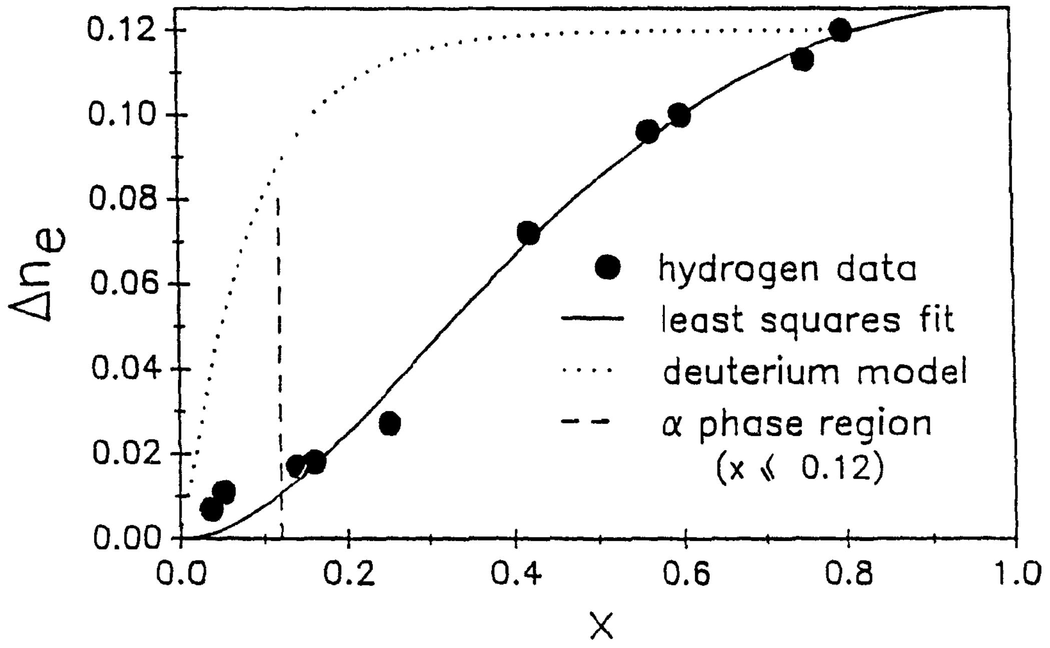

Figure 2.3: Relationship between normalized concentration (x) and extraordinary refractive index increase (Δn_e).

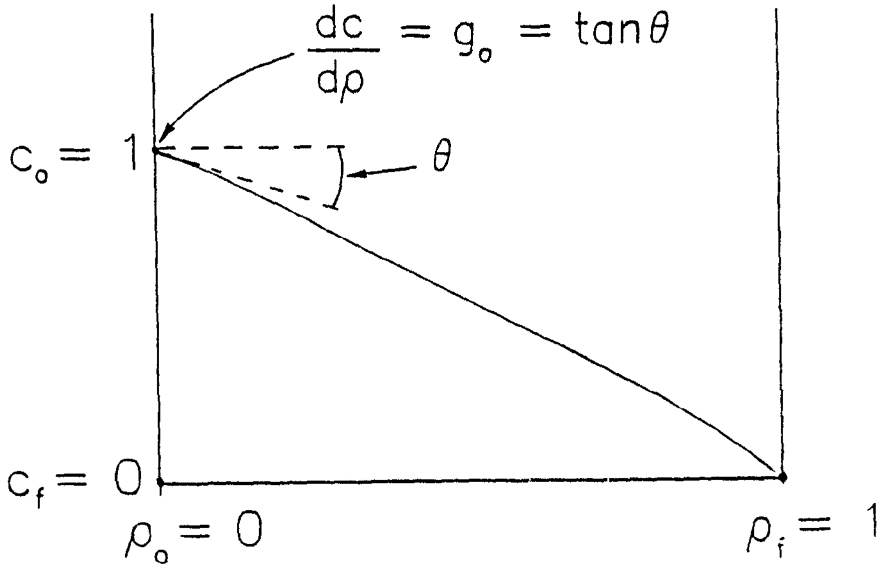

Figure 2.4: Illustration of the shooting technique.

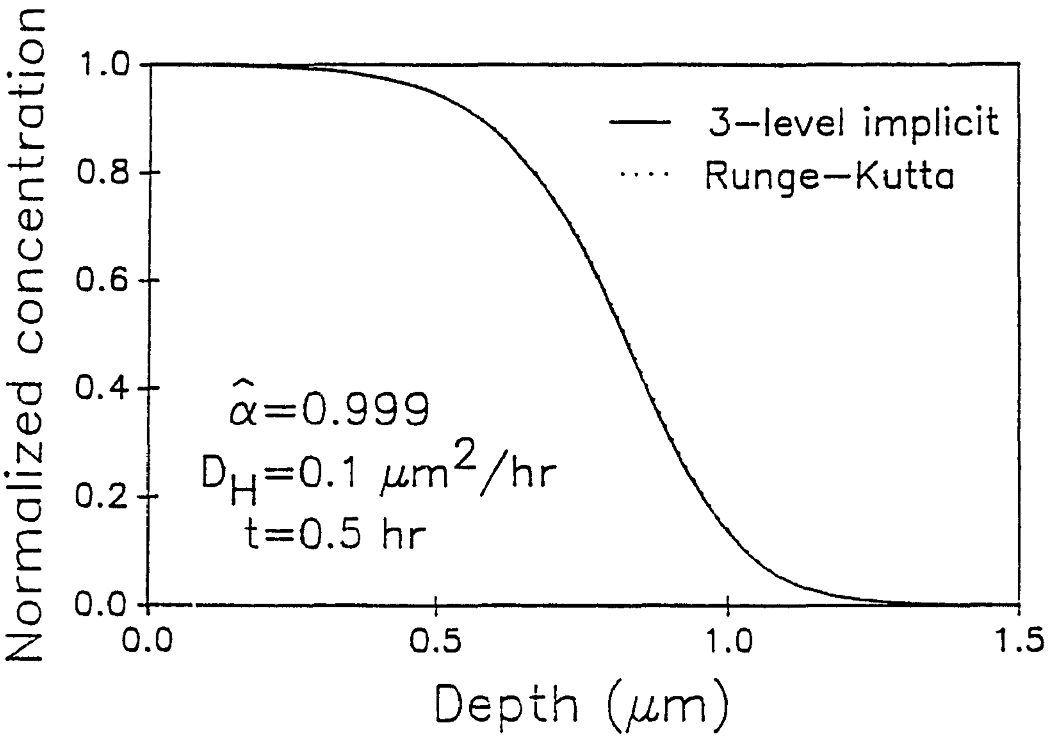

Figure 2.5: Comparison of 3-level implicit and Runge-Kutta numerical solution of nonlinear diffusion equation.

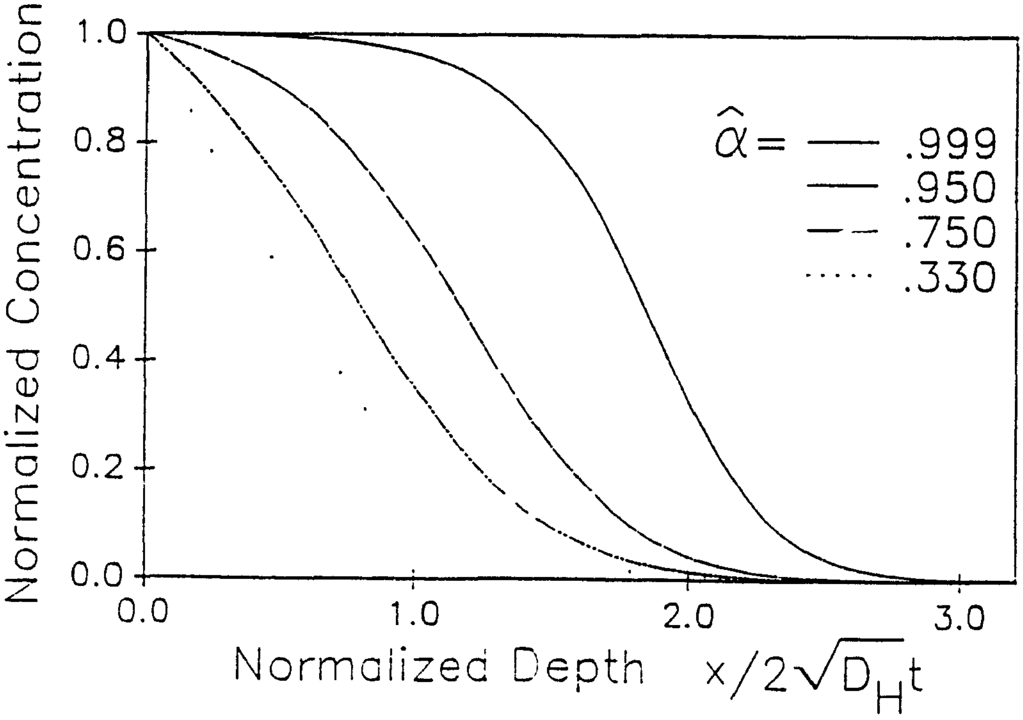

Figure 2.6: Effect of $\hat{\alpha}$ on the normalized concentration.

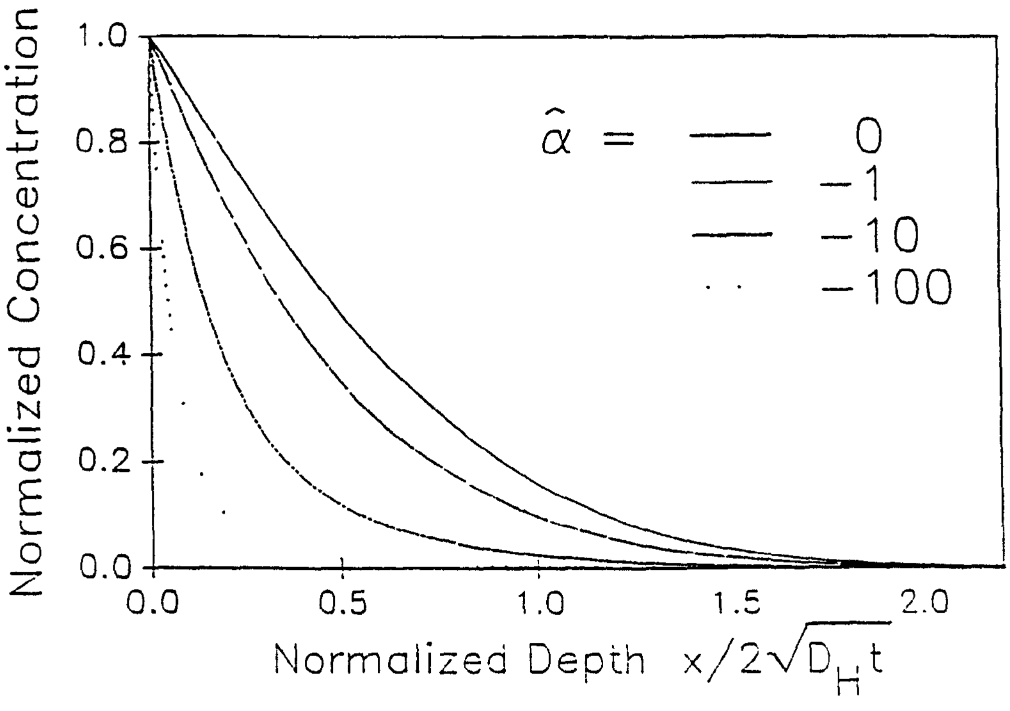

Figure 2.7: Effect of $\hat{\alpha} < 0$ on the normalized concentration.

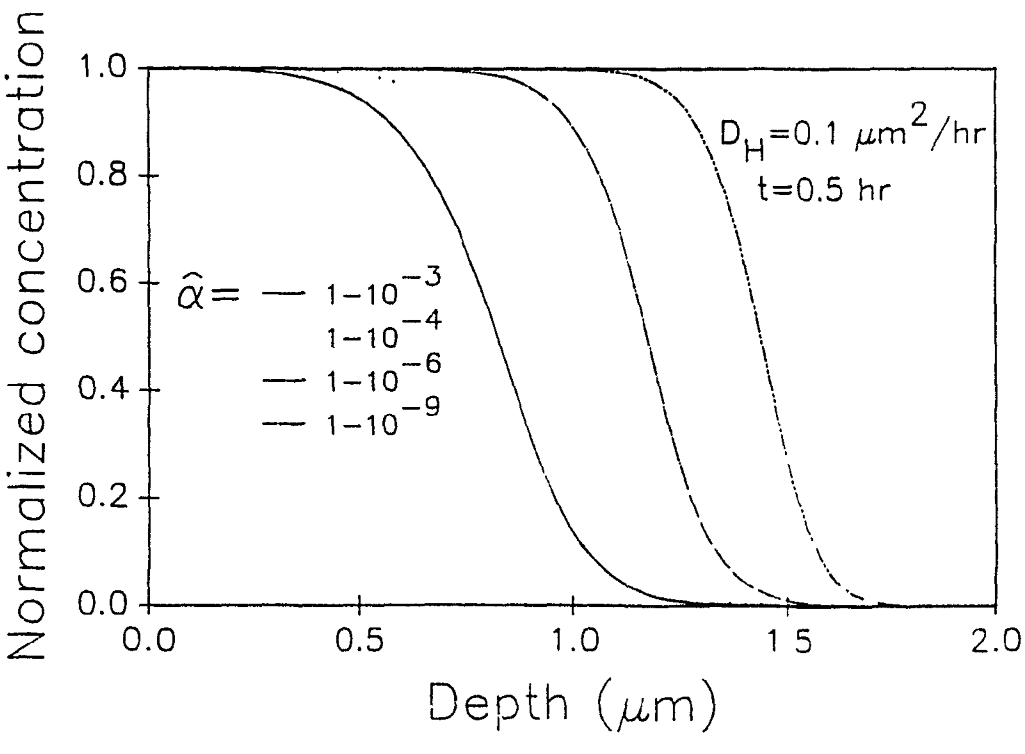

Figure 2.8: Effect of $0.999 < \hat{\alpha} < 1$ on the normalized concentration.

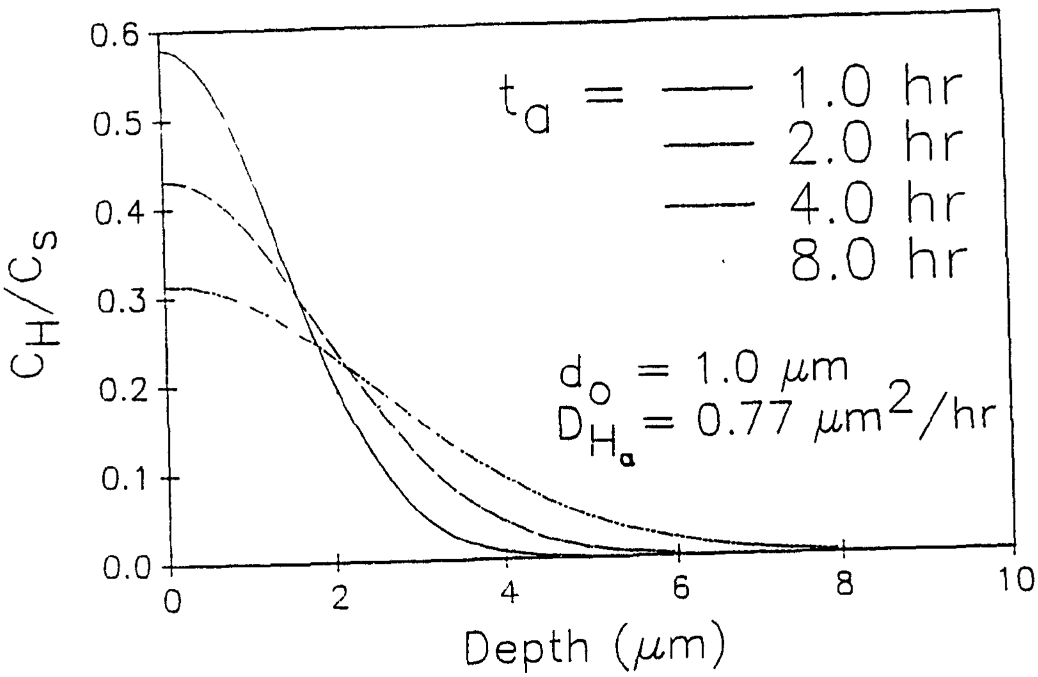

Figure 2.9: Effect of anneal time on normalized concentration for $\hat{\alpha} = 0$.

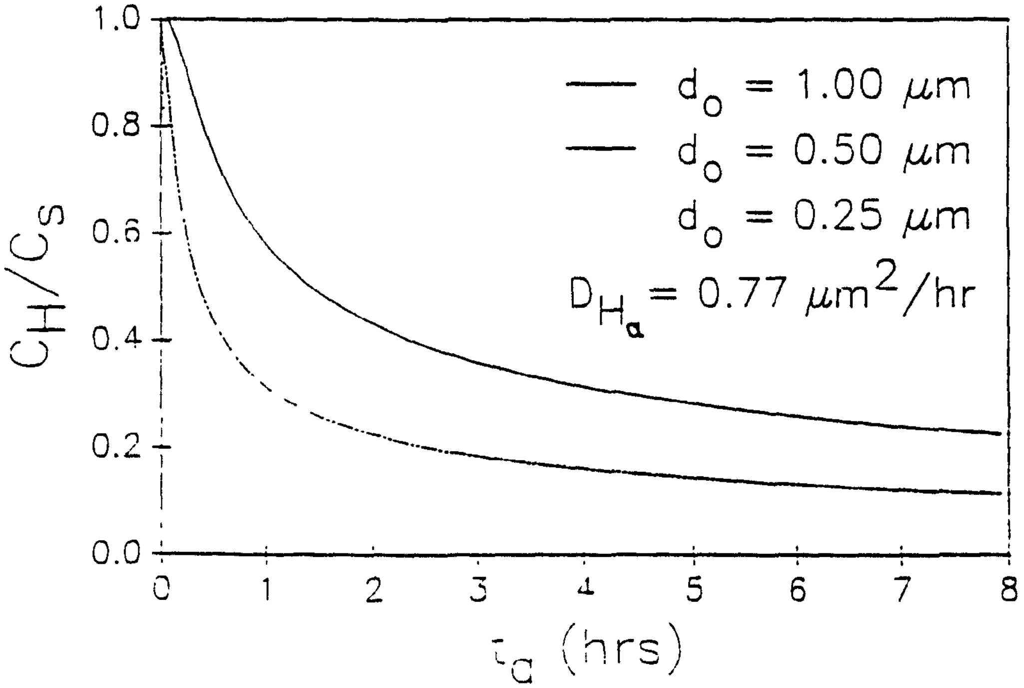

Figure 2.10: Effect of anneal time on normalized surface concentration for various initial depth values (d_o) and $\hat{\alpha} = 0$.

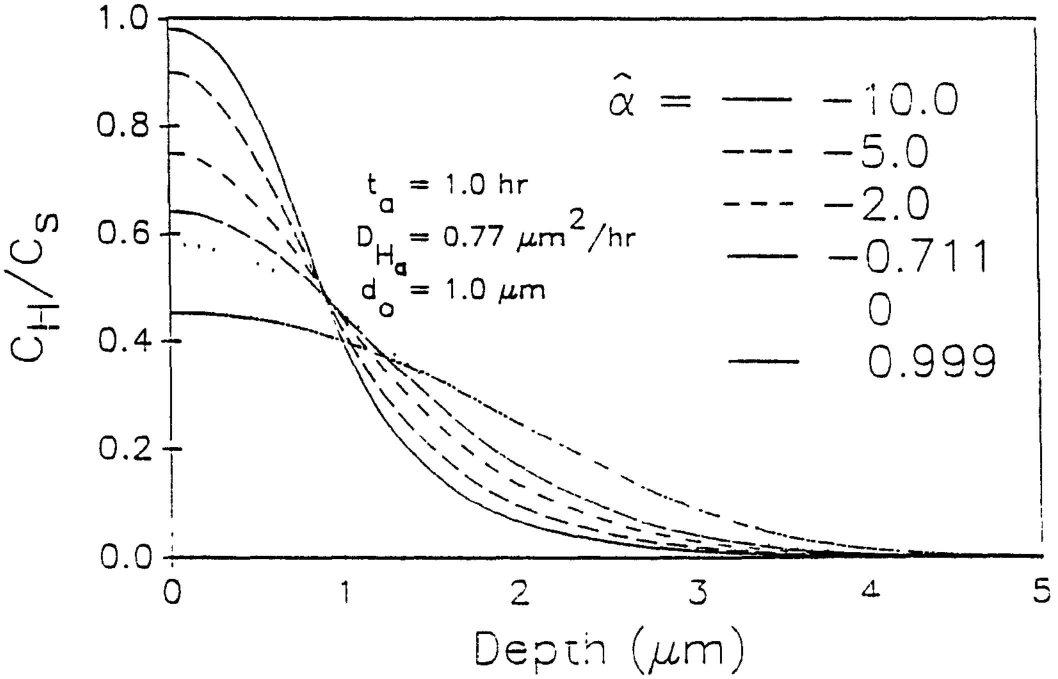

Figure 2.11: Effect of $\hat{\alpha}$ on normalized annealed concentration profile.

Chapter 3

Wave Propagation in PE and APE Planar Waveguides

3.1 Introduction

This chapter discusses wave propagation in both homogeneous and inhomogeneous dielectric media. As was mentioned previously, the PE process results in approximately step-index waveguides. In the past [21,22,23], the anisotropic nature of the $LiNbO_3$ substrate as well as the waveguide layer have been neglected. The validity of this assumption is investigated rigorously by considering the asymmetric anisotropic step-index waveguide. Although the step profile provides a reasonable first-order approximation for PE waveguides, the characterization presented in Chapter 5 will show that a Fermi index model results in a better agreement between theory and experiment. In addition, a generalized Gaussian profile will be used to model APE waveguides. Hence, in order to understand propagation in such graded-index media, the well established WKB method is introduced.

3.2 Propagation in anisotropic waveguides

Waveguide mode propagation in uniaxial anisotropic media such as $LiNbO_3$ has been studied by several authors [84,85,86,87,88]. Generally, it is found that the modes in uniaxial planar waveguides differ considerably from those in isotropic waveguides. In particular, this uniaxial anisotropy results in so-called ***hybrid*** guided modes in addition to the standard TE and TM modes. The nature of the guided mode (i.e. hybrid, TE/TM) is sensitive to the direction of the optic axis in each of the uniaxial layers (see Fig. 3.1 at the end of this chapter). Here, z is taken as the direction of propagation and the spherical angles (θ, ϕ) are used to describe the optic axis direction vector $(\vec{c})$. As will be seen in the waveguide characterization presented in Chapter 5, the depth and index of the step profile are determined from the measured normal (i.e. pure TE/TM) modes of propagation. Hence, in order to simplify the mathematical treatment below, it is desirable to know the optic axis orientations which result in only pure TE and TM modes. It is well established [84,87] that such ***decoupled*** orientations occur for the optic axis lying:

1. in the xz plane $(\phi = 0, 0 \leq \theta \leq \pi)$
2. along the y-axis $\left(\theta = \phi = \frac{\pi}{2}\right)$

For z-cut $LiNbO_3$, the first case is relevant because the optic axis in the waveguide layer and substrate both lie in the direction $(\theta, \phi) = \left(\frac{\pi}{2}, 0\right)$. In the analysis which follows, the discussion is restricted to this special case.

3.2.1 Wave approach to biaxial anisotropic geometry

In this section, a three-layer ***biaxially*** anisotropic geometry in the ***principal*** dielectric axes coordinate system [86] is considered. In this coordinate system, one of the principal dielectric axes in each of the layers is oriented in the direction of propagation (z-axis here) and the other two perpendicular to this direction (See Fig. 3.2). The refractive indices given in Fig. 3.2 are defined along the principal directions. Since the principal dielectric axes coordinate system is used, the permittivity tensor characterizing each of the layers will be ***diagonal*** [89,90],

$$[\epsilon] = \epsilon_o [K] = \epsilon_o \begin{bmatrix} K_{xx} & 0 & 0 \\ 0 & K_{yy} & 0 \\ 0 & 0 & K_{zz} \end{bmatrix} \tag{3.1}$$

$$= \epsilon_o \begin{bmatrix} n_{xx}^2 & 0 & 0 \\ 0 & n_{yy}^2 & 0 \\ 0 & 0 & n_{zz}^2 \end{bmatrix} \tag{3.2}$$

where $\{K_{ii}, n_{ii}, i = x, y, z\}$ are the *principal* relative dielectric constant and refractive index, respectively. Note also that the tensor nature of the dielectric constant will result in the following constitutive relation holding,

$$\vec{D} = [\epsilon]\,\vec{E} \tag{3.3}$$

As with any guided wave problem, the derivation of the dispersion relation begins with *Maxwell's Equations*,

$$\vec{\nabla} \times \vec{E} = -\mu_o \frac{\partial \vec{H}}{\partial t} \tag{3.4}$$

$$\vec{\nabla} \times \vec{H} = \vec{J} + \frac{\partial \vec{D}}{\partial t} \tag{3.5}$$

$$\vec{\nabla} \cdot \vec{D} = 0 \tag{3.6}$$

$$\vec{\nabla} \cdot \vec{H} = 0 \tag{3.7}$$

Since a planar waveguide geometry is assumed, one takes $\frac{\partial}{\partial y} = 0$ and expresses the fields as follows,

$$\begin{bmatrix} \vec{E} \\ \vec{H} \end{bmatrix} = \begin{bmatrix} \vec{E}(x) \\ \vec{H}(x) \end{bmatrix} \exp(j(\omega t - \beta z)) \tag{3.8}$$

Keeping the above in mind (and noting that $\vec{J} = 0$ here), one expands Eq. 3.4 and Eq. 3.5,

$$j\beta E_y = -\mu_o j\omega H_x \tag{3.9}$$

$$j\beta E_x + \frac{\partial E_z}{\partial x} = \mu_o j\omega H_y \tag{3.10}$$

$$\frac{\partial E_y}{\partial x} = -\mu_o j\omega H_z \tag{3.11}$$

$$j\beta H_y = \epsilon_o K_{xx} j\omega E_x \tag{3.12}$$

$$j\beta H_x + \frac{\partial H_z}{\partial x} = -\epsilon_o K_{yy} j\omega E_y \tag{3.13}$$

$$\frac{\partial H_y}{\partial x} = \epsilon_o K_{zz} j\omega E_z \tag{3.14}$$

where $\frac{\partial}{\partial z} = -j\beta$ has already been substituted. As will soon be shown, the lack of y dependence along with the diagonal nature of the dielectric tensor result in the uncoupling of the y component of the fields from the x and z components. Consequently, the modal properties of this anisotropic waveguide can be classified into TE and TM modes as in the isotropic case [86,88]. Note that by taking the divergence of Eq. 3.4 and Eq. 3.5 and using the vector identity $\vec{\nabla} \cdot (\vec{\nabla} \times \vec{A}) = 0$, it follows that Eq. 3.6 and Eq. 3.7 are satisfied. Consequently, in the subsequent analysis, it suffices to consider Eq. 3.4 and Eq. 3.5 only.

3.2.2 TM modes ($H_z = 0$)

From Eq. 3.11 and Eq. 3.9,

$$H_x = E_y = 0 \tag{3.15}$$

From Eq. 3.14 and Eq. 3.12,

$$E_z = \frac{1}{\epsilon_o K_{zz} j\omega} \frac{\partial H_y}{\partial x} \tag{3.16}$$

$$E_x = \frac{\beta}{\omega \epsilon_o K_{xx}} H_y \tag{3.17}$$

Substituting Eq. 3.16 and Eq. 3.17 in Eq. 3.10, one obtains,

$$\frac{d^2 H_y}{dx^2} + (k_o^2 K_{zz} - \frac{K_{zz}}{K_{xx}} \beta^2) H_y = 0 \tag{3.18}$$

where $k_o^2 = \omega^2 \epsilon_o \mu_o$. The above equation is the so-called *Reduced Wave Equation* for the *anisotropic* case. By defining the following quantities,

$$\alpha_i^2 = \frac{K_{izz}}{K_{ixx}} \beta^2 - k_o^2 K_{izz} \quad (i = c, s) \tag{3.19}$$

$$\gamma_f^2 = k_o^2 K_{fzz} - \frac{K_{fzz}}{K_{fxx}}\beta^2 \tag{3.20}$$

where c, s, and f denote the cover, substrate, and film, respectively, one can write the solution to Eq. 3.18 in each of the three regions as follows,

$$H_y = \begin{cases} A\ \exp(\alpha_s x) & \text{(substrate)} \\ B\ \cos(\gamma_f x + \phi) & \text{(film)} \\ C\ \exp(\alpha_c(d - x)) & \text{(cover)} \end{cases} \tag{3.21}$$

Note that the phase shift, ϕ, is introduced to indicate that the solutions are generally neither even or odd. Applying *continuity* of the tangential field (H_y) at $x = 0$ and $x = d$ yields,

$$x = 0: \quad A = B\ \cos\phi \tag{3.22}$$

$$x = d: \quad B\ \cos(\gamma_f d + \phi) = C \tag{3.23}$$

Substituting Eq. 3.22 and Eq. 3.23 in Eq. 3.21 ,

$$H_y = \begin{cases} B\ \cos\phi\ \exp(\alpha_s x) & \text{(substrate)} \\ B\ \cos(\gamma_f x + \phi) & \text{(film)} \\ B\ \cos\xi\ \exp(\alpha_c(d - x)) & \text{(cover)} \end{cases} \tag{3.24}$$

where $\xi = \gamma_f d + \phi$. From Eq. 3.24,

$$E_z = \frac{1}{\epsilon_o K_{izz} j\omega}\frac{\partial H_y}{\partial x} \tag{3.25}$$

$$= \begin{cases} \dfrac{\alpha_s B\ \cos\phi}{\epsilon_o K_{szz} j\omega}\exp(\alpha_s x) & \text{(substrate)} \\[2ex] -\dfrac{B\gamma_f}{\epsilon_o K_{fzz} j\omega}\sin(\gamma_f x + \phi) & \text{(film)} \\[2ex] -\dfrac{\alpha_c B\ \cos\xi}{\epsilon_o K_{czz} j\omega}\exp(\alpha_c(x - d)) & \text{(cover)} \end{cases} \tag{3.26}$$

Applying continuity of E_z at $x = 0$ and $x = d$,

$$x = 0: \quad \frac{\alpha_s B\ \cos\phi}{\epsilon_o K_{szz} j\omega} = -\frac{\gamma_f B \sin\phi}{\epsilon_o K_{fzz} j\omega}$$

$$\Longrightarrow \quad \tan\phi = -\frac{K_{fzz}}{K_{szz}}\frac{\alpha_s}{\gamma_f} \tag{3.27}$$

or

$$\phi = -\tan^{-1}\left\{\frac{K_{fzz}}{K_{szz}}\frac{\alpha_s}{\gamma_f}\right\} \tag{3.28}$$

$$x = d: \; -\frac{B\gamma_f \sin(\gamma_f d + \phi)}{\epsilon_o K_{fzz} j\omega} = -\frac{\alpha_c B \cos\xi}{\epsilon_o K_{czz} j\omega}$$

$$\Longrightarrow \quad \tan\xi = \tan(\gamma_f d + \phi) = \frac{K_{fzz}}{K_{czz}}\frac{\alpha_c}{\gamma_f} \tag{3.29}$$

Using the trigonometric identity,

$$\tan x = \tan(x \pm m\pi) \tag{3.30}$$

and substituting Eq. 3.28 in Eq. 3.29, one obtains,

$$\tan^{-1}\left\{\frac{K_{fzz}}{K_{czz}}\frac{\alpha_c}{\gamma_f}\right\} + \tan^{-1}\left\{\frac{K_{fzz}}{K_{szz}}\frac{\alpha_s}{\gamma_f}\right\} + m\pi = \gamma_f d \quad (m = 0, 1, 2, \ldots) \tag{3.31}$$

Eq. 3.31 is the TM dispersion relation for the three-layer anisotropic geometry [88].

3.2.3 TE modes ($E_z = 0$)

From Eq. 3.14 and Eq. 3.12,

$$H_y = E_x = 0 \tag{3.32}$$

From Eq. 3.9 and Eq. 3.11,

$$H_x = -\frac{\beta}{\omega\mu_o}E_y \tag{3.33}$$

$$H_z = \frac{j}{\omega\mu_o}\frac{\partial E_y}{\partial x} \tag{3.34}$$

Substituting in Eq. 3.13,

$$\frac{d^2E_y}{dx^2} + (k_o^2 K_{yy} - \beta^2)E_y = 0 \tag{3.35}$$

Following a procedure similar to that in the TM case, one defines,

$$\alpha_i^2 = \beta^2 - k_o^2 K_{iyy} \quad (i = c, s) \tag{3.36}$$

$$\gamma_f^2 = k_o^2 K_{fyy} - \beta^2 \tag{3.37}$$

and one can readily write down the field solutions and apply the continuity conditions to yield the following TE dispersion relation [88],

$$\tan^{-1}\left\{\frac{\alpha_s}{\gamma_f}\right\}+\tan^{-1}\left\{\frac{\alpha_c}{\gamma_f}\right\}+m\pi=\gamma_f d \quad (m=0,1,2,\ldots) \tag{3.38}$$

Note that the derivation of these dispersion relations using the *wave* approach is consistent with the results obtained by using the *geometric optics* approach [86].

3.2.4 Dispersion relation for proton-exchanged waveguides

As will be seen in Chapter 5, the characterization of proton-exchanged (PE) waveguides is performed using z-cut (x-propagating) $LiNbO_3$ substrates. For this type of substrate, the associated permittivity tensor is given as follows (see Chapter 2),

$$[\epsilon_s]=\epsilon_o\begin{bmatrix} n_{so}^2 & 0 & 0 \\ 0 & n_{so}^2 & 0 \\ 0 & 0 & n_{se}^2 \end{bmatrix} \tag{3.39}$$

where n_{so} and n_{se} are the principal *ordinary* and *extraordinary* indices of refraction, respectively. Note that the diagonal elements above are defined along the *crystallographic* x, y, and z axes (eg. x-axis in Fig. 3.1 coincides with the optic z axis). In the PE layer, the permittivity tensor takes the following form,

$$[\epsilon_f]=\epsilon_o\begin{bmatrix} n_{fo}^2 & 0 & 0 \\ 0 & n_{fo}^2 & 0 \\ 0 & 0 & n_{fe}^2 \end{bmatrix} \tag{3.40}$$

where $n_{fe} > n_{se}$ and $n_{fo} < n_{so}$. In other words, the extraordinary index is *increased* while the ordinary index has *decreased.* Consequently, only TM waves can be guided in these structures [4]. Furthermore, since

$$n_{fxx}=n_{fe}$$

$$n_{fii}=n_{fo} \quad (\, i=y,z\,)$$

$$n_{sxx}=n_{se}$$

$$n_{sjj}=n_{so} \quad (\, j=y,z\,)$$

$$n_{ckk} = n_o \quad (k = x, y, z)$$

Eq. 3.31 reduces to the following,

$$\phi_s + \phi_c + m\pi = \frac{n_{fo}}{n_{fe}} k_o d \sqrt{n_{fe}^2 - N_e^2} \quad (m = 0, 1, 2, \ldots) \tag{3.41}$$

where

$$\phi_s = \tan^{-1}\left\{\left(\frac{n_{fo} n_{fe}}{n_{so} n_{se}}\right)\sqrt{\frac{N_e^2 - n_{se}^2}{n_{fe}^2 - N_e^2}}\right\} \tag{3.42}$$

$$\phi_c = \tan^{-1}\left\{\left(\frac{n_{fo} n_{fe}}{n_o^2}\right)\sqrt{\frac{N_e^2 - n_o^2}{n_{fe}^2 - N_e^2}}\right\} \tag{3.43}$$

This is the TM dispersion relation for the uniaxially anisotropic PE waveguide. Notice that with

$$n_{fo} = n_{fe} = n_f$$

$$n_{so} = n_{se} = n_b$$

Eq. 3.41 becomes,

$$\phi_s + \phi_c + m\pi = k_o d \sqrt{n_f^2 - N_e^2} \quad (m = 0, 1, 2, \ldots) \tag{3.44}$$

where

$$\phi_s = \tan^{-1}\left\{\left(\frac{n_f}{n_b}\right)^2 \sqrt{\frac{N_e^2 - n_b^2}{n_f^2 - N_e^2}}\right\} \tag{3.45}$$

$$\phi_c = \tan^{-1}\left\{\left(\frac{n_f}{n_o}\right)^2 \sqrt{\frac{N_e^2 - n_o^2}{n_f^2 - N_e^2}}\right\} \tag{3.46}$$

which, as expected, is the TM dispersion relation for the *isotropic* case [4]. Note that in both Eq. 3.41 and Eq. 3.44,

$$k_o = \frac{2\pi}{\lambda_o} \tag{3.47}$$

$$N_e = \frac{\beta}{k_o} \tag{3.48}$$

where N_e is the *effective* index of refraction for mode order m. Using $n_{se} = 2.200$ and $n_{so} = 2.287$ (i.e. the principal refractive indices for $LiNbO_3$ at $\lambda = 0.6328\,\mu m$), one can generate the theoretical step-index dispersion curves for various values of $\Delta n_e = n_{fe} - n_{se}$ and $\Delta n_o = n_{fo} - n_{so}$ as shown in Fig. 3.3. These curves reveal that the isotropic model, although being a good approximation in the ***single mode*** region, begins to break down as:

1. mode order increases
2. Δn_e increases
3. Δn_o increases (negatively)

In short, for a particular value of Δn_e, the sensitivity of the anisotropic TM dispersion relation to the value of Δn_o increases as the mode order increases. This leads to the rather interesting possibility of determining the change in the ordinary index by optimizing Eq. 3.41 for n_{fo} and n_{fe} so that the best fit between the measured mode indices and theoretical curves is obtained. Similar optimization techniques have been reported previously [91,92] (although in these studies both TE and TM modes were involved). The practicality of this technique as far as z-cut PE $LiNbO_3$ waveguides is concerned will be assessed in more detail in Chapter 5. Using the value $\Delta n_o \approx -0.04$ quoted by De Micheli [44], Nutt [104] found in his study of leaky modes in PE waveguides that this decrease in n_o is significant and should not be neglected as was so often done in the past.

3.2.5 Design considerations

As a final comment, it is frequently necessary in waveguide design to know the number of modes that can be supported by such structures. For a particular waveguide mode, cutoff occurs when $N_e = n_{se}$. Substituting this condition in Eq. 3.41, one finds that the total number of modes is $M = m + 1$ or

$$M = 1 + \frac{1}{\pi}\left[\frac{n_{fo}}{n_{fe}}k_o d\sqrt{n_{fe}^2 - n_{se}^2} - \tan^{-1}\left\{\left(\frac{n_{fo}n_{fe}}{n_o^2}\right)\sqrt{\frac{n_{se}^2 - n_o^2}{n_{fe}^2 - n_{se}^2}}\right\}\right]_{int} \tag{3.49}$$

where *int* refers to integer truncation (An alternative expression for the above cutoff condition will be discussed in the next section). The above equation shows that for a given depth and film index, the number of modes decreases as the wavelength increases.

3.3 Propagation in inhomogeneous media

The extension of the above discussion to propagation in inhomogeneous anisotropic waveguides is quite complicated [93,94,95] and, therefore, will not be presented here. In what follows, the assumption of isotropic inhomogeneous media is made. This is a reasonable assumption because:

1. The previous discussion showed that anisotropy results in some discrepancies for only very multimoded waveguides.
2. Annealing reduces the birefringence in the waveguide film (see Chapter 5) and, hence, the effects of anisotropy will be correspondingly smaller.

3.3.1 Scalar wave equation

By manipulating *Maxwell's Equations* in graded-index media, one can derive the following *generalized* vector wave equations [98],

$$\vec{\nabla}^2\vec{E} + \vec{\nabla}\left(\frac{\vec{\nabla}n^2(\vec{r})\cdot\vec{E}}{n^2(\vec{r})}\right) + k_o^2 n^2(\vec{r})\vec{E} = 0 \qquad (3.50)$$

$$\vec{\nabla}^2\vec{H} + \frac{1}{n^2(\vec{r})}(\vec{\nabla}n^2(\vec{r})) \times (\vec{\nabla}\times\vec{H}) + k_o^2 n^2(\vec{r})\vec{H} = 0 \qquad (3.51)$$

where $n(\vec{r})$ is the refractive index at the position $\vec{r} = x\hat{i} + y\hat{j} + z\hat{k}$. For the case of a planar waveguide, one takes $\frac{d}{dy} = 0$ and $n(\vec{r}) = n(x)$. These assumptions result in the following uncoupled scalar wave equations,

$$\frac{d^2H_z}{dx^2} + (k_o^2 n^2(x) - \beta^2)H_z = 0 \qquad (3.52)$$

$$\frac{d^2E_x}{dx^2}+\frac{d}{dx}\left(\frac{E_x}{n^2(x)}\frac{dn^2(x)}{dx^2}\right)+(k_o^2n^2(x)-\beta^2)E_x \;=\; 0 \qquad (3.53)$$

As a further simplification, one usually introduces the transformation $\bar{E}_x = \dfrac{E_x}{n(x)}$ so that the first derivative term is eliminated,

$$\frac{d^2\bar{E}_x}{dx^2}+\left(\frac{1}{2n^2(x)}\frac{d^2n^2(x)}{dx^2}-\frac{3}{4n^4(x)}\left(\frac{dn^2(x)}{dx}\right)^2+k_o^2n^2(x)-\beta^2\right)\bar{E}_x=0 \qquad (3.54)$$

For TE modes, one has

$$E_x \;=\; E_z \;=\; H_y \;=\; 0 \qquad (3.55)$$

$$E_y \;=\; -\frac{\omega\mu_o}{\beta}H_x \qquad (3.56)$$

$$H_z \;=\; \frac{1}{j\beta}\frac{dH_x}{dx} \qquad (3.57)$$

where H_x is found by solving Eq. 3.52. Similarly, for TM modes,

$$H_x \;=\; E_y \;=\; H_z \;=\; 0 \qquad (3.58)$$

$$E_z \;=\; \frac{1}{j\beta n^2(x)}\frac{d}{dx}(n^2(x)E_x) \qquad (3.59)$$

$$H_y \;=\; \frac{\omega n^2(x)\epsilon_o}{\beta}E_x \qquad (3.60)$$

and E_x is given by Eq. 3.54.

Note that the solution for the TE and TM modes involves the solution of a second-order ordinary differential equation with varying coefficient, namely,

$$\frac{d^2\Psi}{dx^2}+q^2(x)\Psi=0 \qquad (3.61)$$

where

$$q^2(x)=\begin{cases} k_o^2n^2(x)-\beta^2 & \text{TE modes}\\ k_o^2n^2(x)-\beta^2+\left(\dfrac{1}{2n^2(x)}\dfrac{d^2n^2(x)}{dx^2}-\dfrac{3}{4n^4(x)}\left(\dfrac{dn^2(x)}{dx}\right)^2\right) & \text{TM modes}\end{cases} \qquad (3.62)$$

$$\Psi=\begin{cases} H_x & \text{TE modes}\\ \dfrac{E_x}{n(x)} & \text{TM modes}\end{cases} \qquad (3.63)$$

Furthermore, the refractive index is usually expressed as,

$$n(x) = \begin{cases} n_c & x < 0 \\ n_b + \Delta n_s f(x) & x > 0 \end{cases} \tag{3.64}$$

$$\begin{aligned} \Delta n_s &= n_s - n_b \\ n_c &= \text{refractive index of cover (=1 for air)} \\ n_s &= \text{surface refractive index} \\ n_b &= \text{substrate or bulk refractive index} \\ f(x) &= \text{normalized profile function } (0 \leq f \leq 1) \end{aligned}$$

Exact[1] analytical solutions to the above problem exist for only a few refractive index profiles (eg. exponential, parabolic, secant-hyperbolic, etc.). In practice, however, ion-exchange and APE waveguides are frequently modeled by Gaussian and complimentary error function profiles which are not amenable to an analytic solution. Consequently, various numerical and approximate techniques [96,97] have been used to determine the waveguide modal characteristics. The discussion which follows will concentrate on one such approximate technique, in particular, the WKB method.

3.3.2 The WKB method

Also referred to as the phase-integral method, the WKB (Wentzel, Kramers, Brillouin) approximation which first arose in the context of quantum mechanics has found widespread use in optical waveguide problems. Although the resulting dispersion relation can also be derived from *geometric optics*, the WKB method yields, in addition, approximate field expressions. If the variation of the refractive index

---

[1] Although they are termed 'exact', these analytic solutions are approximate in the TM case since the first and second derivative terms are neglected yielding a scalar wave equation identical in form to the TE case.

is small, then the well known WKB approximation [98]

$$\frac{1}{q^2}\left[\frac{1}{2q}\frac{d^2q}{dx^2}-\frac{3}{4q^2}\left(\frac{dq}{dx}\right)^2\right] \ll 1 \tag{3.65}$$

is valid resulting in the solution,

$$\Psi = \begin{cases} A\exp(\gamma_c) & x<0 \\ \dfrac{B}{\sqrt{q(x)}}\cos\left(\displaystyle\int_x^{x_t} q(x)\;dx-\frac{\pi}{4}\right) & 0<x<x_t \\ \dfrac{B}{2\sqrt{\gamma_s(x)}}\exp(-\displaystyle\int_{x_t}^{x}\gamma_s(x)\;dx) & x>x_t \end{cases} \tag{3.66}$$

where A and B are constants and

$$\gamma_c^2 = \beta^2 - k_o^2 n_c^2 \tag{3.67}$$

$$\gamma_s(x) = \beta^2 - k_o^2 n^2(x) \tag{3.68}$$

$$q(x_t) = 0 \tag{3.69}$$

In practice, one usually neglects the first and second derivative terms in $q(x)$ for the TM case. Numerical solution of the scalar wave equation has shown that the resulting errors are well within the approximation given by Eq. 3.65 [96]. In the above solution, the turning point, x_t, represents the equivalent boundary for the graded-index waveguide. At this point, it is instructive to analyze this phenomenon in terms of geometric optics. The ray associated with a discrete waveguide mode traverses a curved path as it penetrates into the inhomogeneous region eventually reaching a point at which $\theta(x_t) = \frac{\pi}{2}$ (i.e. $n(x_t) = N_e$) where the angle $\theta(x)$ is defined with respect to the x axis (see Fig. 3.4). The ray subsequently returns to the surface where it is totally internally reflected. This contrasts with the homogeneous waveguide case where straight ray trajectories result in total internal reflection at both the substrate and cover interfaces. Note that the phase shift of $\frac{\pi}{4}$ in the oscillatory region (i.e. $0 < x < x_t$) reflects the fact that a linear approximation in $q(x)$ has been used in the vicinity of the turning point to avoid the singularity (i.e.

$[q(x_t)]^{-1} \rightarrow \infty)$. By matching solutions in the oscillatory and evanescent regions, one can readily derive the following WKB dispersion relation [98],

$$k_o \int_0^{x_t} \sqrt{n^2(x) - N_e^2}\, dx = m\pi + \phi_c + \phi_t \quad (m = 0, 1, 2, \ldots) \tag{3.70}$$

where ϕ_c and ϕ_t are one half the phase change at the cover surface and turning point, respectively,

$$\phi_c = \tan^{-1}\left\{\nu\sqrt{\frac{N_e^2 - n_c^2}{n_s^2 - N_e^2}}\right\} \tag{3.71}$$

$$\phi_t = \frac{\pi}{4} \tag{3.72}$$

$$\nu = \begin{cases} 1 & \text{TE} \\ \dfrac{n_s^2}{n_c^2} & \text{TM} \end{cases} \tag{3.73}$$

3.3.3 Design considerations

In waveguide characterization studies, it is usually convenient to express the above dispersion relation in terms of the normalized parameters, specifically,

$$V = k_o d\sqrt{n_s^2 - n_b^2} \tag{3.74}$$

$$b = \frac{N_e^2 - n_b^2}{n_s^2 - n_b^2} \tag{3.75}$$

$$\xi = \frac{x}{d} \tag{3.76}$$

In addition, the refractive index in the film is approximated as,

$$n^2(x) = \left[n_b + \Delta n_s f\left(\frac{x}{d}\right)\right]^2 \tag{3.77}$$

$$\approx n_b^2 + 2n_b\Delta n_s f\left(\frac{x}{d}\right) \quad (\Delta n_s \ll n_b) \tag{3.78}$$

$$\rightarrow \quad n_s^2 - n_b^2 \approx 2n_b\Delta n_s \tag{3.79}$$

Upon substitution of the above expressions, the dispersion relation becomes [99],

$$V \int_0^{\xi_t} \sqrt{f(\xi) - b}\, d\xi = \phi_c + \phi_t + m\pi \tag{3.80}$$

Comparison with rigorous numerical results [100,101] has shown that the WKB dispersion relation gives excellent results far from cutoff and for multimode waveguides with $E = |N_{e_{WKB}} - N_{e_{EXACT}}|/\Delta n_s \sim 1\%$ which is usually within experimental error (see Chapter 4). The inaccuracy of this technique in the cutoff and single mode region (where $E \sim 5\%$) has been attributed to an erroneous assumption of a constant phase shift of $\frac{\pi}{4}$ at the turning point. Recently, by substituting the exact b vs V values in the WKB dispersion relation, it has been found [102,103] that the effective phase shift at the turning point can be expressed as,

$$\begin{aligned} \phi_t &= \phi_t(b, m, f(\xi)) && (3.81) \\ \lim_{b \to 0} \phi_t &\to 0 && (3.82) \\ \lim_{b \to 1} \phi_t &\to \frac{\pi}{4} && (3.83) \end{aligned}$$

The exact functional dependence of ϕ_t, however, has not been conclusively established. Keeping the above in mind, one can investigate the cutoff behaviour of graded-index waveguides to determine the number of guided modes. Since at cutoff $b = 0$ (or $N_e = n_b$) and $\xi_t \to \infty$, one has

$$M = 1 + \frac{1}{\pi}\left[k_o d\sqrt{n_s^2 - n_b^2}\int_0^\infty \sqrt{f(\xi)}\, d\xi - \tan^{-1}\left\{\nu\sqrt{\frac{n_b^2 - n_c^2}{n_s^2 - n_b^2}}\right\} - \phi_t|_{b=0}\right]_{int} \tag{3.84}$$

Alternatively, one can express the cutoff condition as follows [99],

$$\frac{d}{\lambda} = \frac{m\pi + \tan^{-1}\left\{\nu\sqrt{\frac{n_b^2 - n_c^2}{n_s^2 - n_b^2}}\right\} + \phi_t|_{b=0}}{2\sqrt{n_s^2 - n_b^2}\int_0^\infty \sqrt{f(\xi)}\, d\xi} \tag{3.85}$$

This useful design equation allows one to generate theoretical normalized cutoff depth curves for various mode orders, index increases, and profile shapes. As an example, for a Gaussian profile,

$$\begin{aligned} f(\xi) &= \exp(-\xi^2) && (3.86) \\ \int_0^\infty \sqrt{f(\xi)}\, d\xi &= \int_0^\infty \exp\left(-\frac{\xi^2}{2}\right) d\xi = \sqrt{\frac{\pi}{2}} && (3.87) \end{aligned}$$

The resulting normalized cutoff depth curves are shown in Fig. 3.5. From this graph, one can easily determine the number of modes that a waveguide with arbitrary parameters (i.e. Δn_s, d) can support. Note that the value $\phi_t = 0$ represents a lower bound on the cutoff. In any case, it is important to realize that the relevant parameter as far as the number of modes is concerned is the value of the above integral which depends on the particular profile. By taking $\phi_t = 0$ and noting that the above integral equals one for a step-index profile, the above cutoff expressions reduce to those corresponding to the homogeneous slab case discussed in the previous section.

As will be seen in the waveguide characterization in Chapter 5, a numerical optimization routine of the simple and convenient analytic homogeneous and inhomogeneous waveguide dispersion relations discussed above will be used in conjunction with the measured effective mode indices to determine the important waveguide design parameters, in particular, $n(x)$.

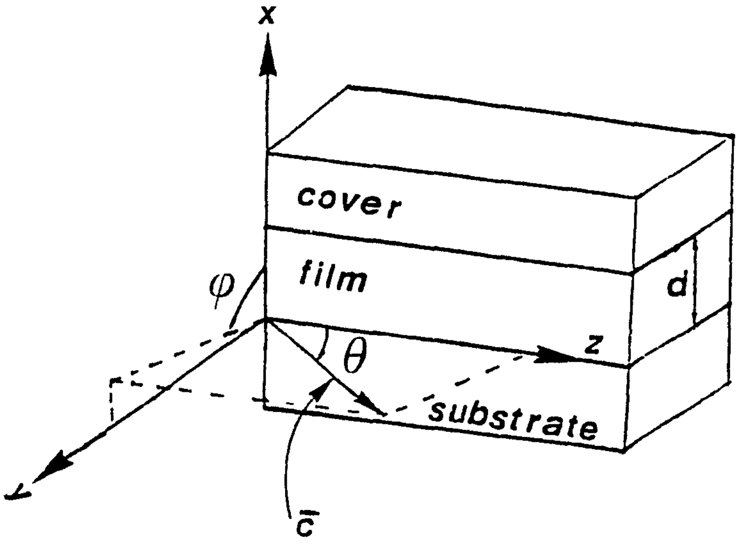

Figure 3.1: Geometry of asymmetric anisotropic planar waveguide.

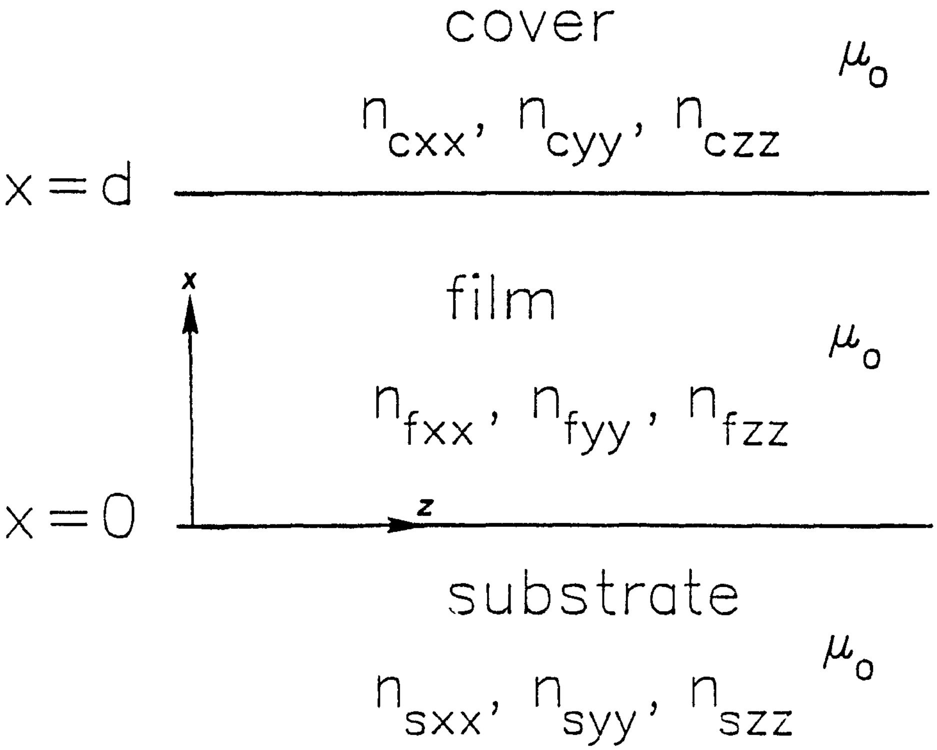

Figure 3.2: Three-layer biaxial geometry in the principal dielectric axes coordinate system where $(\theta, \phi) = (\frac{\pi}{2}, 0)$.

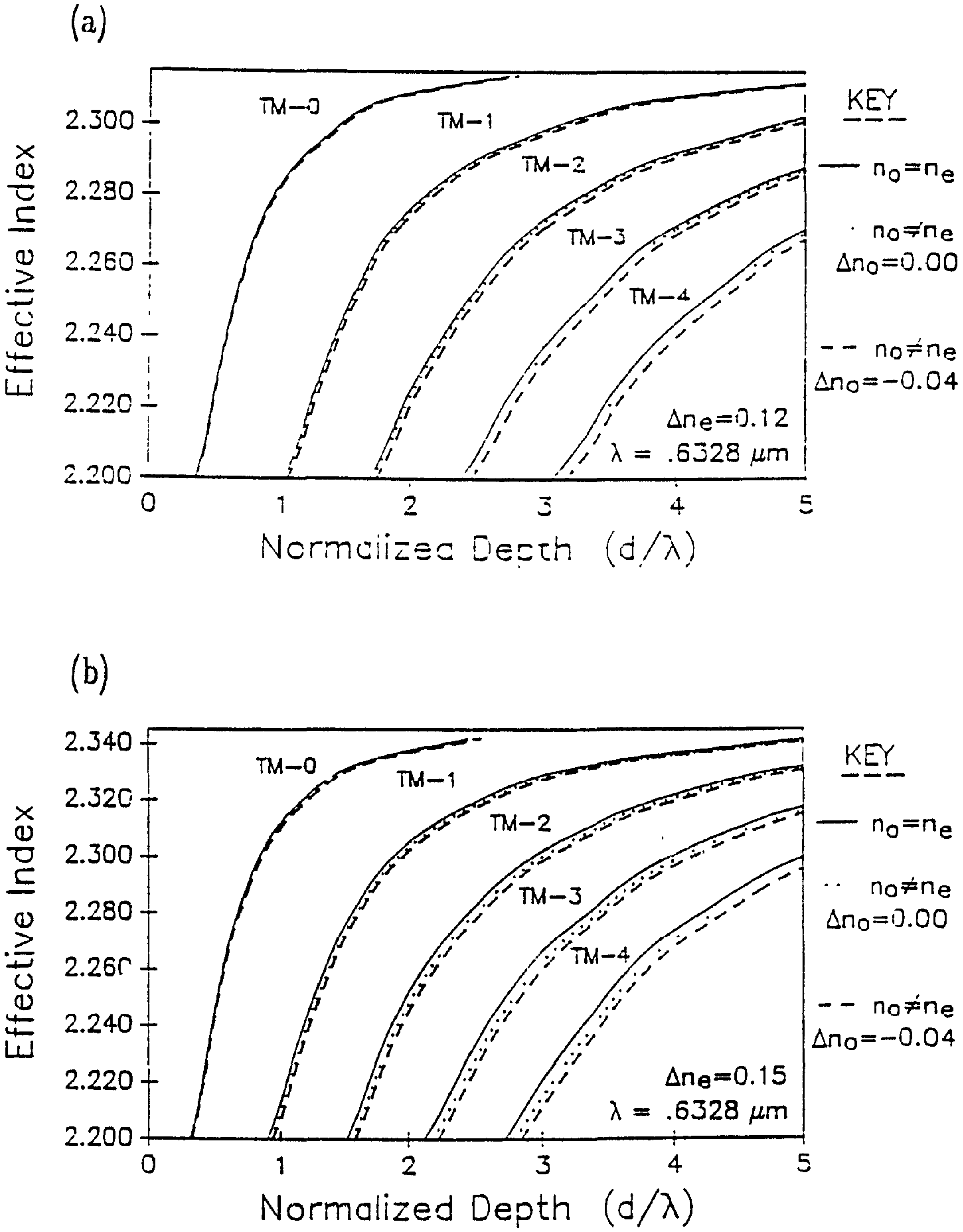

Figure 3.3: Effect of uniaxial anisotropy on the theoretical step-index dispersion curves as Δn_e ranges from (a) 0.12 to (b) 0.15.

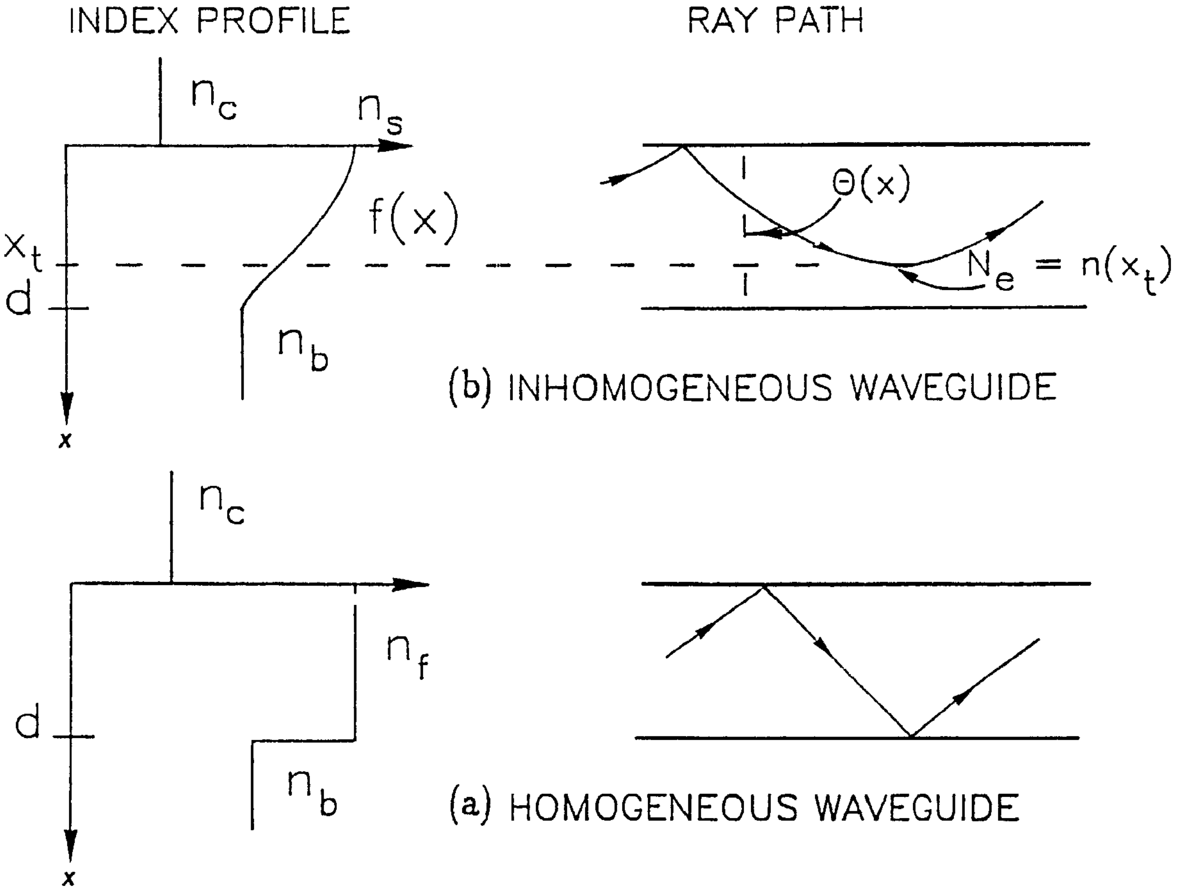

Figure 3.4: Index profiles and ray trajectories for (a) homogeneous and (b) inhomogeneous waveguides.

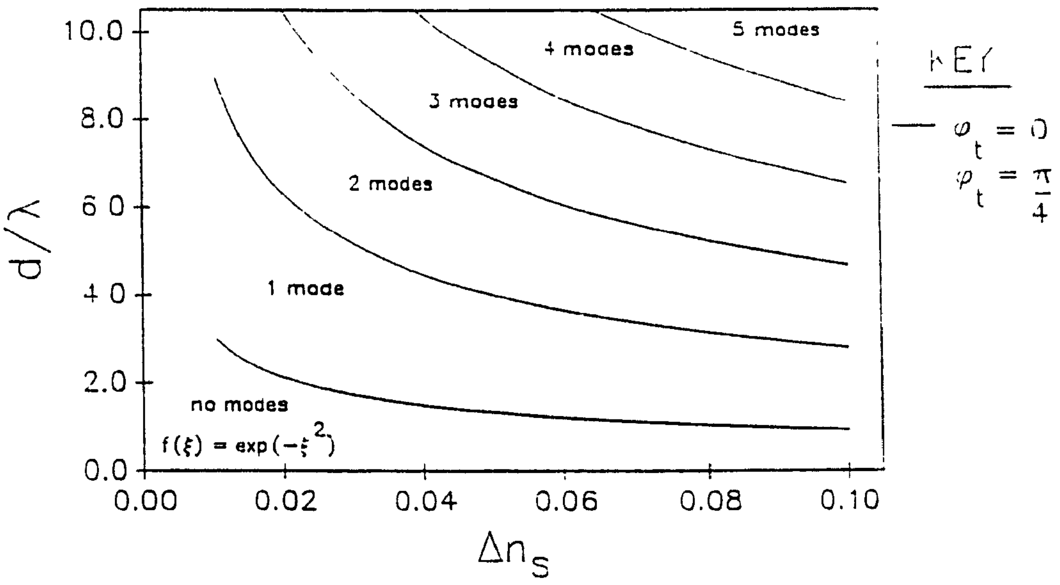

Figure 3.5: Effect of turning point phase shift (ϕ_t) on the cutoff condition.

Chapter 4

Fabrication and Measurement Techniques

4.1 Introduction

In this chapter, a detailed discussion of the fabrication and measurement of proton-exchanged optical waveguides in $LiNbO_3$ is presented. In particular, the fabrication is treated as a four stage process involving the preparation of the substrates, cleaning of the $LiNbO_3$ crystal, creation of the dielectric waveguiding layer (i.e. initial PE), and subsequent annealing of the waveguide. As for the measurement of these waveguides, standard prism-coupling techniques to determine the important waveguide parameters including modal propagation constant and propagation loss are introduced.

4.2 Fabrication

4.2.1 Substrate preparation

The substrate material used in the fabrication of PE waveguides is z-cut $LiNbO_3$, as mentioned previously, a uniaxial crystal with electro-optic, acousto-optic, and waveguiding properties which are of considerable interest in OIC's. Manufactured by Crystal Technology, the substrate ($50\,mm$ by $25\,mm$ by $1\,mm$) is an optical grade, well polished and defect free crystal. Unfortunately, in direct contrast to soda lime glass (which is used extensively in ion-exchange research), the cost involved is relatively high (\$300 *U.S.* per $LiNbO_3$ substrate as compared to < \$0.50 per soda lime substrate as of Sept. '89). Consequently, to reduce this cost, the single crystal of $LiNbO_3$ must first be cut into smaller substrates. Due to the crystalline nature of the $LiNbO_3$ substrate, great care must be taken in the cutting procedure to avoid any damage. This procedure involves the following steps:

- Coat a $5\,cm$ square piece of polyethelene (plastic) with paraffin wax.
- Place the $LiNbO_3$ single crystal on the wax before it has dried.
- Coat the top of the $LiNbO_3$ crystal with a second layer of paraffin wax. The function of these two layers of wax is two-fold. In addition to ensuring that the crystal is kept fixed on the plastic base, they absorb some of the vibrations caused by the friction between the cutting blade and crystal and, hence, reduce the chances of any damage (see Fig. 4.1 at the end of this chapter).
- Once the wax has completely dried, fix this setup on the cutter's x-y translational stage. Make sure that the speed at which the cutter advances across the crystal is small. Too large a speed results in greater vibrations and, hence, increases the chances of cracking the crystal. In addition, constant water flow over the setup reduces any heating of the blade.

Using this procedure, 10 substrates with approximate dimensions of $5\,mm$ by $25\,mm$ by $1\,mm$ are produced from this single crystal (the cost of each substrate has, as a result, been reduced to about \$30 a piece). With the substrates prepared as such, one proceeds with the next step in the fabrication, specifically, the cleaning of the substrate.

4.2.2 Cleaning procedure

Before the planar waveguide can be fabricated by PE, the substrates must be made as immaculately clean as possible. This is necessary because the diffusion of organic and inorganic impurities on the surface of the substrates can contaminate the waveguiding layer. One must keep in mind, however, that a cleaning procedure that is too aggressive may actually degrade the surface quality of the substrate [2].

The cleaning procedure begins with rinsing the substrate in deionized (D.I.) water followed by a spraying of N_2 gas. Using a cotton swab (i.e. Q-tip), the substrate is then cleaned with a solution of mild, non-abrasive detergent (Sparkleen) and rinsed again in D.I. water. The remaining steps are similar to those used in the cleaning of Si and $GaAs$ wafers. These include:

- Clean the substrate in trichloroethylene (TCE) for about 10 minutes using a (Bransonic) sonic cleaner. Rinse thoroughly in D.I. water.
- Repeat the above procedure with acetone.
- Repeat the above procedure with methanol.
- Dry with N_2 gas.

Note that one must be particularly careful when using the sonic cleaner. The level of the liquid (i.e. organic/inorganic cleaning agent) within the beaker containing the crystal substrate as well as the surrounding water level must be high enough (about 3/4) so as to reduce the intensity of the sonic vibrations which could otherwise lead to the cracking of the crystal (see Fig. 4.2). To assess the quality of the cleaning, a simple inspection technique known as the water break method [2] is used. This involves spraying the substrate with D.I. water and observing the interference pattern as the water slowly evaporates. If the substrate is judged clean, it is placed in an oven (set at $80\,^{o}C$) for a few minutes to ensure that it is completely dry before the PE.

4.2.3 Planar waveguide fabrication

Preliminary considerations

In this study, the proton source chosen for the PE fabrication is pure (i.e. undiluted) pyrophosphoric acid crystal (purchased from Fluka Chemical Co.). As mentioned earlier, the use of this acid has been shown to lead to low loss and high index waveguides. Some of its physical properties are listed below (Table 4.1). At room temperature, the acid is a solid. As a result, slight heating ($50-60\,^{o}C$) is needed to convert the crystal into its more practical viscous liquid form. Note that care must be exercised in the handling of the acid which can cause severe burns on contact.

Table 4.1: Physical properties of pyrophosphoric acid ($H_4P_2O_7$)

Melting point (^{o}C)	61
Boiling point (^{o}C)	300
Dissociation constant (K_a)	2.0×10^{-2}
Atomic weight	177.98
Purity (%)	97

Fabrication of PE waveguide

The fabrication of the PE waveguide using pyrophosphoric acid was performed using the surface coating technique [24,54] which consists of the following steps:

- Using a glass rod, coat a cleaned $LiNbO_3$ substrate with pyrophosphoric acid.
- Put the coated substrate on a glass plate at the bottom of a pyrex bottle making sure that the plate is placed in horizontally. This ensures that the

substrate rests on a flat surface so that an approximately uniform coat exists throughout the duration of the proton-exchange process (see Fig. 4.3).

- Insert the pyrex bottle in a (Lindberg) vertical furnace preheated at the desired diffusion temperature.

- With the proton-exchange complete, remove the bottle from the furnace and allow it to cool down without removing the cover.

- After 10 – 15 minutes, take the waveguide out of the bottle and clean it in D.I. water to remove any excess acid.

Notice that in using this technique, the substrate and acid are *not* preheated to the desired diffusion temperature. This of course results in a very simple and quick fabrication procedure. Any problem with thermal shock is overcome by the fact that the coated substrate is placed in a pyrex bottle which takes a finite time to heat up and, consequently, smoothes out any large temperature gradient that the substrate may otherwise experience. The cost of simplifying the fabrication procedure, however, is the further complication of the analytic modeling of the diffusion process. This is due to two reasons:

1. Since the diffusion temperatures used in the characterization (see Chapter 5) are higher than the minimum temperature associated with PE, some diffusion has already taken place before the desired diffusion temperature is reached.

2. Since the exact starting and ending points of the diffusion process are not known, the PE diffusion time is conveniently defined as the time during which the pyrex bottle containing the coated $LiNbO_3$ substrate is inserted and subsequently removed from the furnace.

These points will be elaborated upon in the next chapter where the analytic modeling is discussed in detail.

4.2.4 Annealing of planar waveguides

As mentioned in Chapter 2, many of the problems inherent in PE waveguides can be overcome with an annealing process. Hence, this is a necessary step in the fabrication of high quality waveguides. The annealing of the PE waveguides was performed as follows [54]:

- Preheat a horizontal furnace at the desired annealing temperature.
- Allow dry oxygen to flow through the furnace tube (about $1100\frac{cc}{min}$). This helps to prevent deoxidization of the surface of the PE waveguide.
- Place the (cleaned) PE waveguide in a small quartz tube which has been washed in acetone and D.I. water.
- Insert this small tube in the large furnace tube. To avoid the problem of thermal shock on both entry and removal of the waveguide, move the small tube to and from the furnace hot spot over a time period of about 1 minute (see Fig. 4.4).
- With the annealing completed, remove the small quartz tube from the furnace and allow it to cool on a ceramic plate (while keeping the annealed PE waveguide in it).
- After $10 - 15$ minutes, remove the waveguide from the small quartz tube and check that the surface of the waveguide is transparent. If deoxidization has occurred, the surface shows a slightly yellow or even brown color. In such a case, the annealing must be repeated with a new waveguide.

The annealing time is defined as the time during which the sample reaches the furnace hot spot and its subsequent removal. The dry O_2 flow was maintained during the entire annealing process. It is worth noting that recently (see Chapter

2) it was pointed out that the use of different annealing environments can result in some discrepancies in the waveguide parameters. For this work, it was found that the dry O_2 atmosphere yielded good quality waveguides and, consequently, other annealing conditions were not used.

4.3 Measurement techniques

4.3.1 Introduction

Once the PE/APE waveguide is fabricated, its waveguiding properties need to be measured. These include the refractive index profile (eg. thickness and index of the film) as well as the waveguide propagation loss. In this study, these parameters were determined through the use of two standard techniques both based on the prism coupler: modal spectroscopy and the two-prism sliding method. Due to the lack of availability of facilities on campus, other characterization techniques (eg. NRA, SIMS, ERDA) mentioned in Chapter 2 were not explored. Recently, a fellow researcher in the Guided Wave Optics group at McGill initiated the use of some microanalytical techniques [106] including SEM and EPMA to analyze the concentration profile in ion-exchanged glass waveguides. Unfortunately, due to a phenomenon known as the berylium window [107], these techniques could not be used to measure concentrations of the lighter elements such as lithium and hydrogen which are of particular interest in PE waveguides. Although information obtained from such techniques would be helpful in understanding the PE process at a more fundamental level, one must keep in mind that the end goal of such work is the determination of the waveguide parameters relevant in the design of optical devices. To this end, the prism-coupling techniques mentioned above have been found to suffice and, indeed, have been successfully used in this laboratory in design work involving both proton and ion-exchange devices [54,105,108].

4.3.2 Modal spectroscopy

Qualitative discussion

The essence of this technique involves using a prism coupler to excite the individual modes propagating in the planar waveguide. By measuring the so-called ***synchronous*** angles associated with each mode, one can then obtain the corresponding ***effective*** index values (i.e. modal propagation constants) which, as will be seen in Chapter 5, can be used to construct the refractive index profile in the waveguide film.

Generally then, the prism coupling technique involves placing a high refractive index prism close to a planar waveguide. When an optical beam is incident upon the prism's base at an angle exceeding its critical angle, a standing wave distribution within the prism and an exponentially decaying (i.e. evanescent) field in the gap region are created which propagate parallel to the base of the prism with a phase velocity,

$$v_p = \frac{c_o}{n_p \sin\theta} \tag{4.1}$$

where c_o is the speed of light in vacuum, n_p is the prism index, and θ is the incident angle at the base of the prism. If the waveguide is sufficiently close to the prism, the evanescent field underneath the prism base penetrates the waveguide. If the horizontal phase velocity of the incident beam matches the phase velocity of a particular mode (see Fig. 4.5),

$$v_{pm} = \frac{c_o}{n_f \sin\theta_m} \tag{4.2}$$

then that waveguide mode will be excited (Here, n_f and θ_m are the film index and mode angle, respectively). By reciprocity, if a second prism is placed a distance away in the direction of propagation, the propagating mode will be coupled out of the waveguide at an angle that is characteristic of that mode (see Fig. 4.6). This phenomenon of time-average power being transmitted through the air gap is usually referred to as *optical tunneling* [4]. Mathematically, this phase-matching condition is expressed as follows,

$$n_p \sin\theta = n_f \sin\theta_m \tag{4.3}$$

where the subscript m refers to the mode order. Under this condition, the guided waves are said to be *synchronous.* In short, to couple to a particular waveguide mode, one must use an incident beam phase-matched to that mode. Taking $N_e = n_f \sin\theta_m$, one can derive from *geometric optics* the following useful result [2],

$$N_e = n_p \sin\left\{\alpha_p + \sin^{-1}\left(\frac{\sin\theta_i}{n_p}\right)\right\} \tag{4.4}$$

where α_p is the base angle of the prism and θ_i is the external incident angle. Note that since the effective index satisfies $n_b \leq N_e \leq n_f$, then $n_p > n_f$ is required to ensure that the incident angles at the prism base are considerably less than 90° and, hence, more practical to deal with. In measuring PE $LiNbO_3$ waveguides, the prism used is uniaxially anisotropic in nature (see below) and, consequently, one must be careful to distinguish between the ordinary and extraordinary indices of refraction of the prism and film (see Appendix A).

Measurement setup

The measurement of the synchronous mode angles was performed using the configuration in Fig. 4.7. Laser light from a helium-neon source ($\lambda = 0.6328\,\mu m$) passes through a polarizer and is coupled into the waveguide using a rutile (TiO_2) prism (The relevant prism paramters are $\alpha_p = 45^o$ and $n_{p_o} = 2.5837$ at $\lambda = 0.6328\,\mu m$). An output prism located a short distance away then couples the light out of the waveguide and the resulting far field radiation pattern is observed on a white screen. The prism waveguide holder rests on a goniometer with 5 degrees of freedom (i.e. x, y, z, θ, ϕ) thus allowing for easy adjustment of the incident angle and, hence, the ability to selectively excite each waveguide mode. The detailed procedure to measure these synchronous angles consists of the following steps:

- Make sure that both prisms as well as the waveguide are thoroughly cleaned in acetone and D.I. water. This is necessary because any contamination in the interface between the prism and waveguide can result in a significant reduction in the coupling efficiency.

- Using a pair of tweezers, mount the prisms and waveguide in the specially designed holder (Fig. 4.8). Adjust the pins on the holder so that a light pressure is applied to the prism. Note that applying too much pressure not only increases the *loading* of the prism (thus reducing the measurement accuracy [2]) but, also, can result in the cracking of the substrate and/or prism.

- Carefully place the waveguide-prism holder on the micropositioner.

- Measure first the zero reference angle by adjusting the rotational stage until the incoming beam is reflected back onto itself.

- Rotate the stage until the phase-matching criterion is satisfied, i.e. a mode is excited. A bright line also known as an m-line which is the far field radiation pattern of the guided mode then appears on the white screen. Record the angular measurement at which the m-line appears brightest.

- Compute the synchronous angle of the particular waveguide mode by subtracting the above 2 quantities from each other. The use of Eq. 4.4 then leads to the corresponding effective mode index.

Examples of some m-lines are shown in Fig. 4.9. Only TM modes were observed to propagate along the waveguide thus supporting the contention (see Chapter 2) that only the extraordinary refractive index (n_e) increases. One final note concerns the measurement error. By repeating the measurement for each waveguide mode several times, an error of about 2-3 minutes of arc results. This produces a corresponding error in N_e of about $\pm 3 \times 10^{-4}$. Moreover, errors in the prism parameters (i.e. α_p and n_p) lead to an additional uncertainty of about $\pm 3 \times 10^{-4}$.

4.3.3 Propagation loss

Overview

Optical propagation loss in dielectric waveguides is an essential characterization parameter because it can often limit the performance of optical integrated circuits. Two categories of losses can be distinguished: absorptive and scattering.

Since bulk $LiNbO_3$ is transparent in the visible and near infrared region (0.5 to $4\mu m$) of the optical spectrum, the little absorption loss that exists is mostly due to impurities (eg. Fe^{2+} and OH^-). As for scattering loss, it comes in one of two forms. Volume scattering occurs because of local fluctuations in the index of refraction. In crystals such as $LiNbO_3$, these fluctuations may be due to a number of factors including random dislocations, faults, impurities, or compositional variations within the volume of the waveguide. Moreover, stresses in the waveguide layer can also result in increased scattering . Surface scattering due to surface roughness or dimensional fluctuations (eg. in the height and/or width) of the waveguide constitutes the second form of scattering loss. It is generally accepted that scattering loss is more important than absorption loss in $LiNbO_3$ waveguides [1].

Measurement setup

A variety of techniques have been developed to measure the propagation loss. These include the cut-back method [109], the two and three-prism sliding methods [110,111], and, recently, scattering detection methods [112]. In this characterization, the two-prism sliding technique was used to measure propagation loss in PE waveguides.

The measurement configuration is shown in Fig. 4.10. The same prism-coupler arrangement described in the previous section is used to excite a waveguide mode. A (Hamamatsu) video camera is then used to image the m-line on the white screen. The camera's output video signal is then displayed on a video monitor whose analog output is subsequently fed into an oscilloscope. The measurement procedure involves the following steps:

- Make sure that both prisms as well as the waveguide have been thoroughly cleaned (since dust particles on the surface of the waveguide and/or prism can contribute to additional scattering and, hence, affect the accuracy of the measurement)
- After exciting the waveguide mode on the white screen, locate the corresponding m-line pattern on the oscilloscope. This is done by scanning in Horizontal Mode A which allows for one frame of the video signal to be displayed as a set of sharp vertical lines. Record the voltage level corresponding to the m-line (Note that an attenuator may be needed so as not to saturate the video camera).
- Move (i.e. slide) the output prism towards the input prism in steps of $1 - 2\,mm$ recording each time the voltage level of the m-line. Make sure that the input prism is kept fixed so that the input coupling coefficient remains approximately constant (Unfortunately, since the output prism is moved, its coupling coefficient changes resulting in some measurement error).

Calculating propagation loss

When light propagates along a waveguide it becomes attenuated according to [113],

$$P = P_i e^{-\alpha L} \tag{4.5}$$

where

$$\begin{aligned} P_i &= \text{input power} \\ \alpha &= \text{attenuation coefficient} \\ L &= \text{propagation length} \\ P &= \text{output power } (\propto\ (voltage)^2) \end{aligned}$$

Since losses are usually expressed in $\frac{dB}{cm}$,

$$\rightarrow \quad 10\log_{10} P = 10\log_{10} P_i - \alpha_{dB} L$$

or

$$\begin{aligned} 10\log_{10}\frac{P}{P_i} &= -\alpha_{dB} L & (4.6) \\ \alpha_{dB} &= 10\,\alpha\log_{10} e & (4.7) \end{aligned}$$

Hence, by plotting the data points (V^2, L) according to Eq. 4.6, an estimate on the propagation loss, α_{dB}, can be obtained from a simple linear regression fit.

Results of these fabrication and measurement procedures will be presented in the next chapter which deals with analytic modeling and subsequent data reduction.

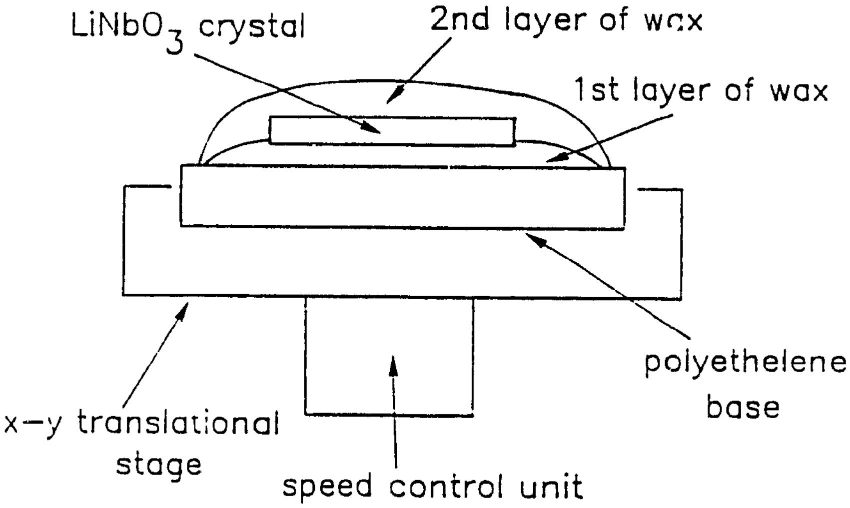

Figure 4.1: Cutting the $LiNbO_3$ crystal substrate.

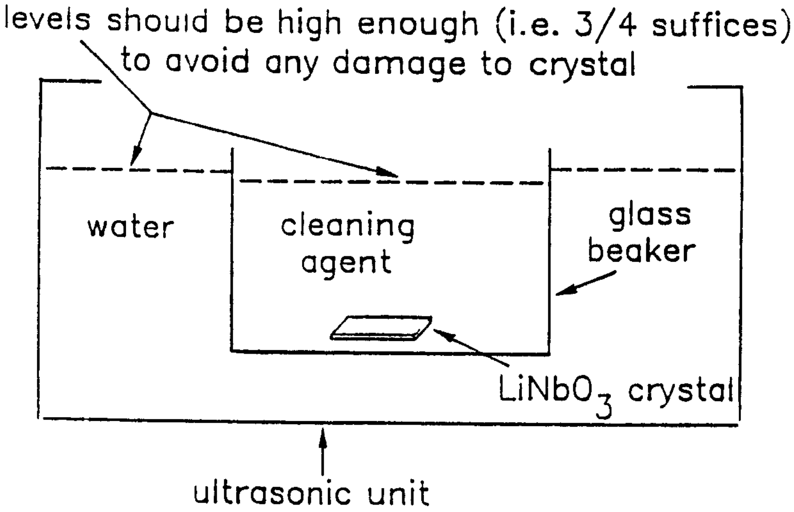

Figure 4.2: Sonic cleaning procedure.

STEP 1

– Using a glass rod, coat the $LiNbO_3$ substrate with pyrophosphoric acid ($H_4P_2O_7$).

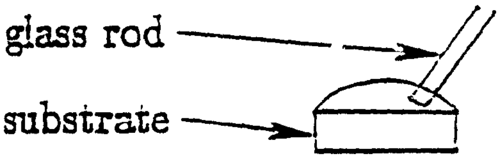

STEP 2

– Place the coated substrate on a glass plate at the bottom of a pyrex bottle.

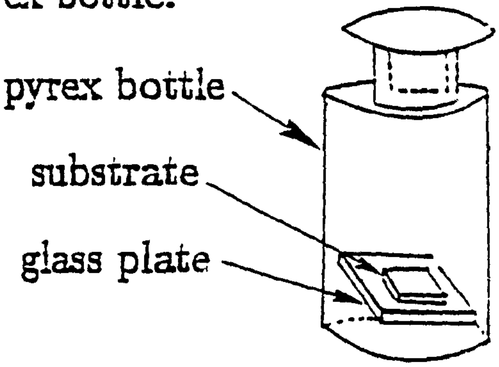

STEP 3

– Put the pyrex bottle in a vertical furnace preset at the desired diffusion temperature.

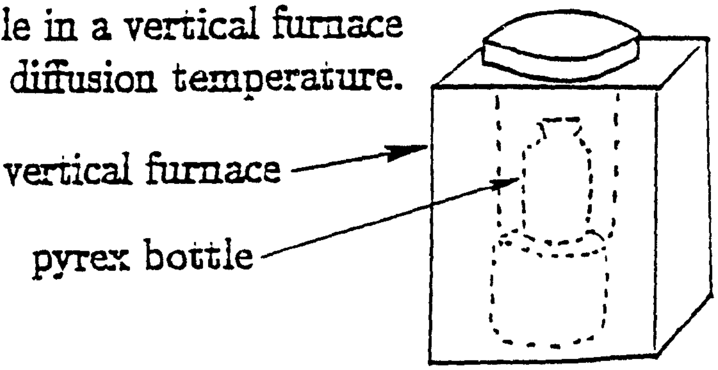

Figure 4.3: Fabrication procedure for proton-exchanged waveguides using pyrophosphoric acid.

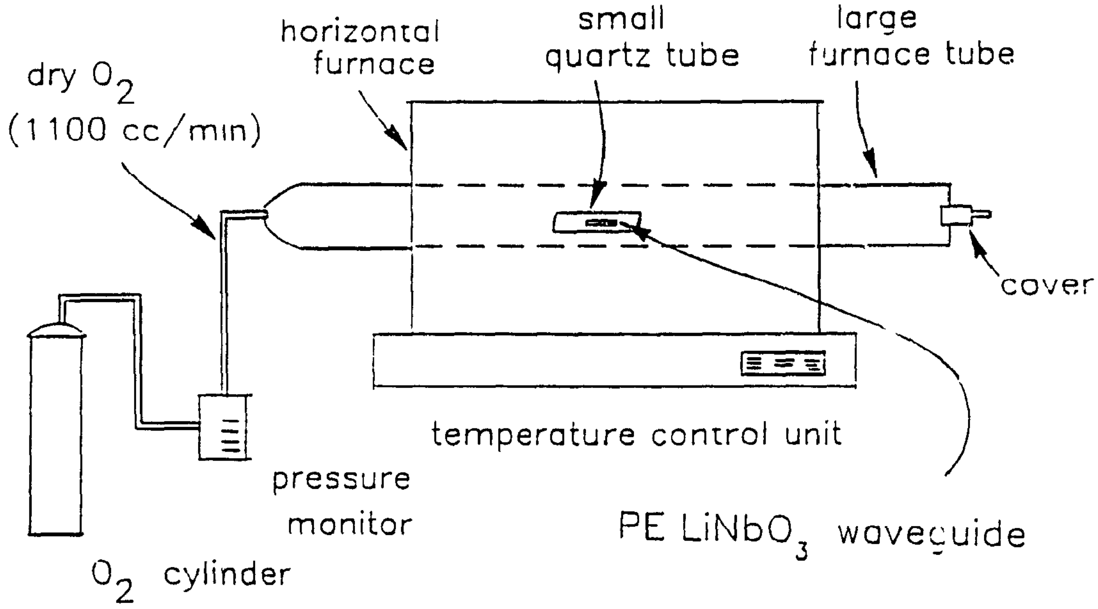

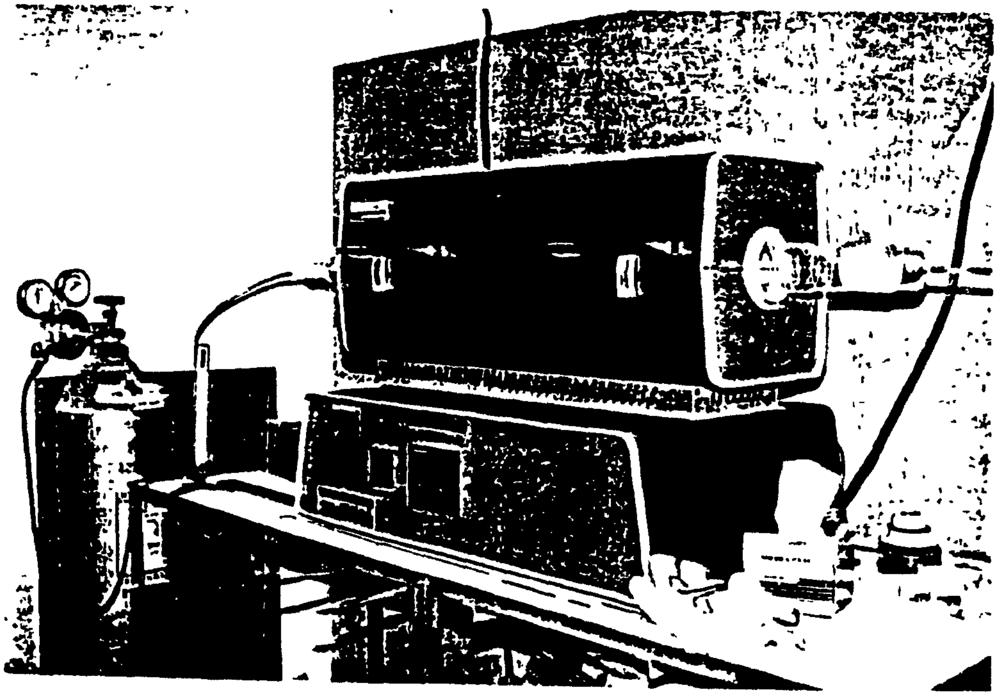

Figure 4.4: Annealing procedure for proton-exchanged waveguides: block diagram (top) and actual setup (bottom).

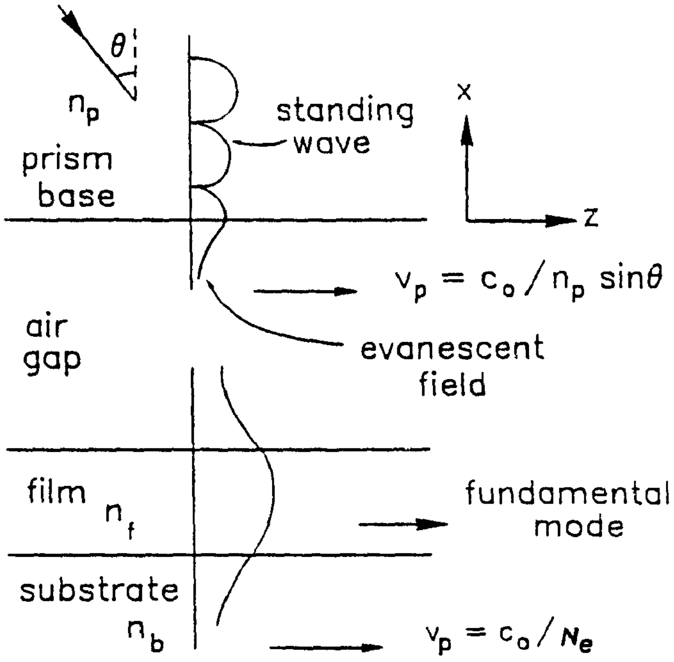

Figure 4.5: Field distributions in air gap, prism, and waveguide film.

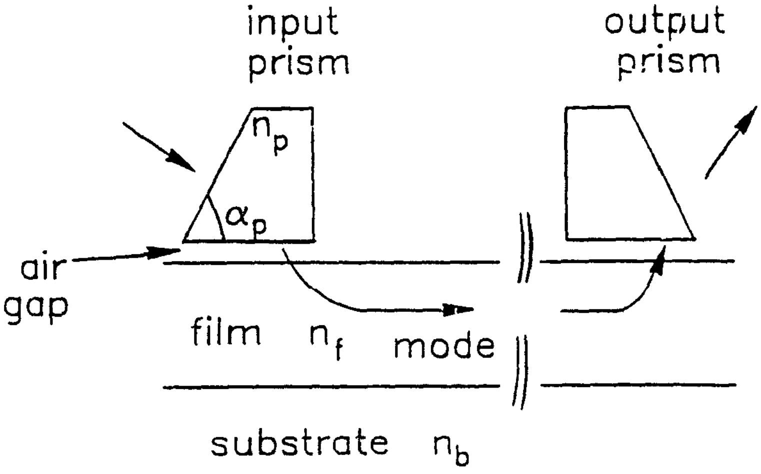

Figure 4.6: Prism coupling to waveguide.

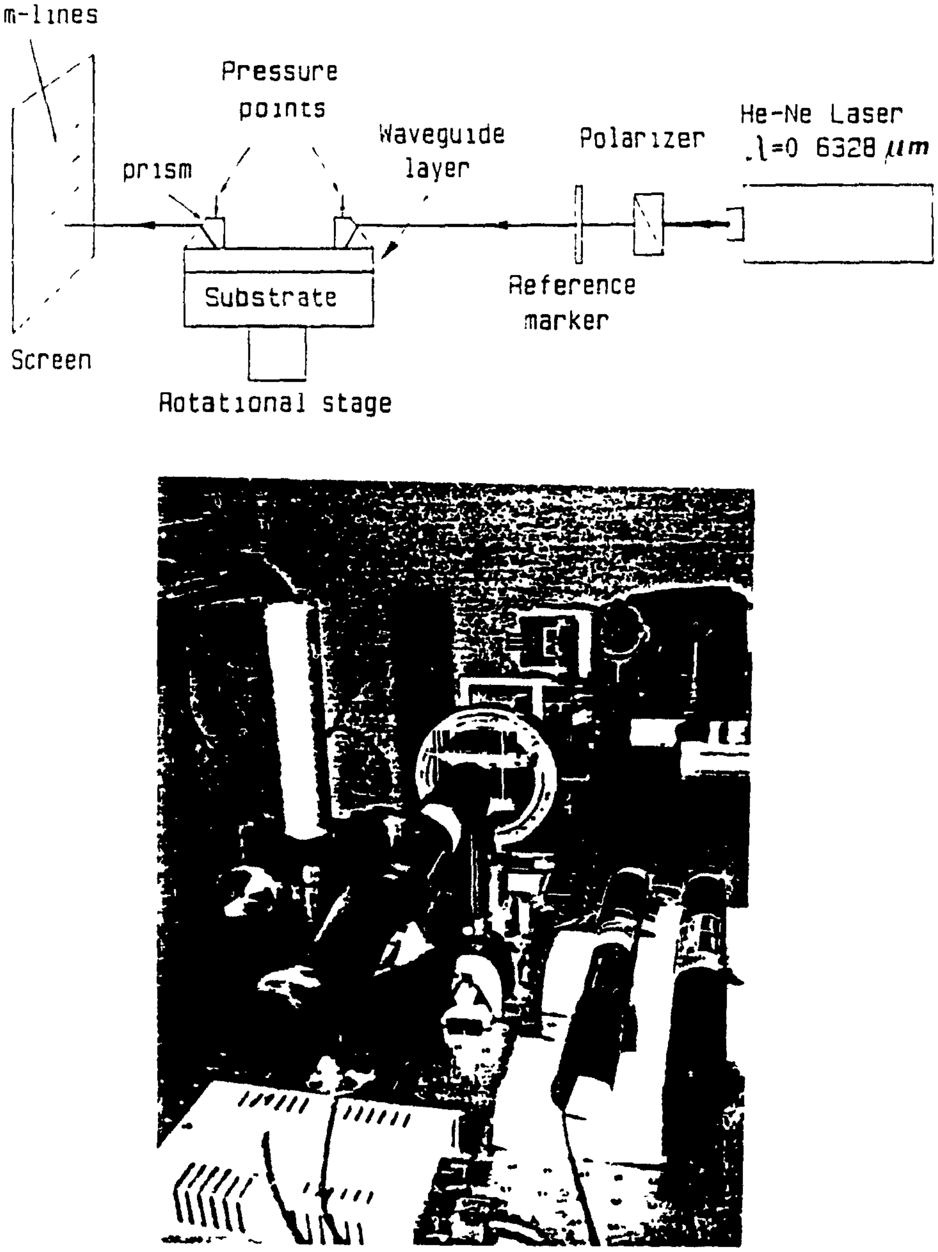

Figure 4.7: Experimental setup for measuring synchronous angles: block diagram (top) and actual system (bottom).

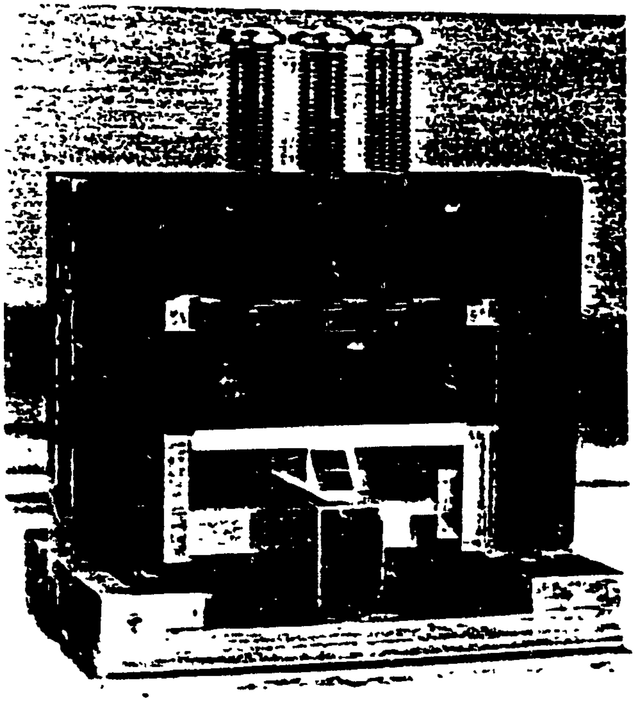

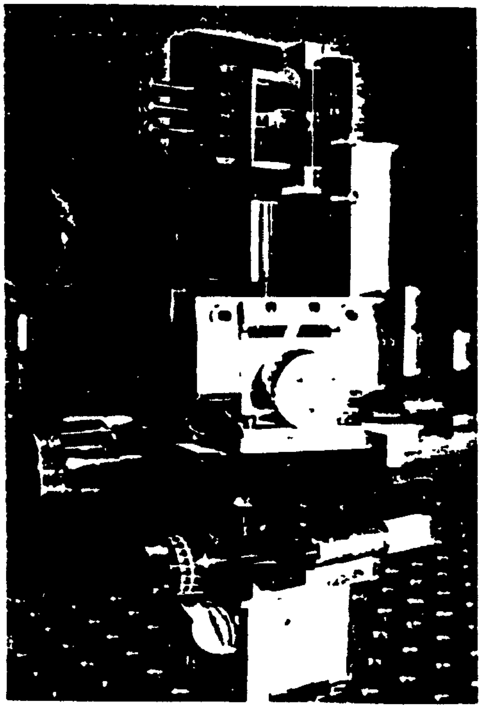

Figure 4.8: Waveguide prism holder (top) mounted on rotational stage (bottom).

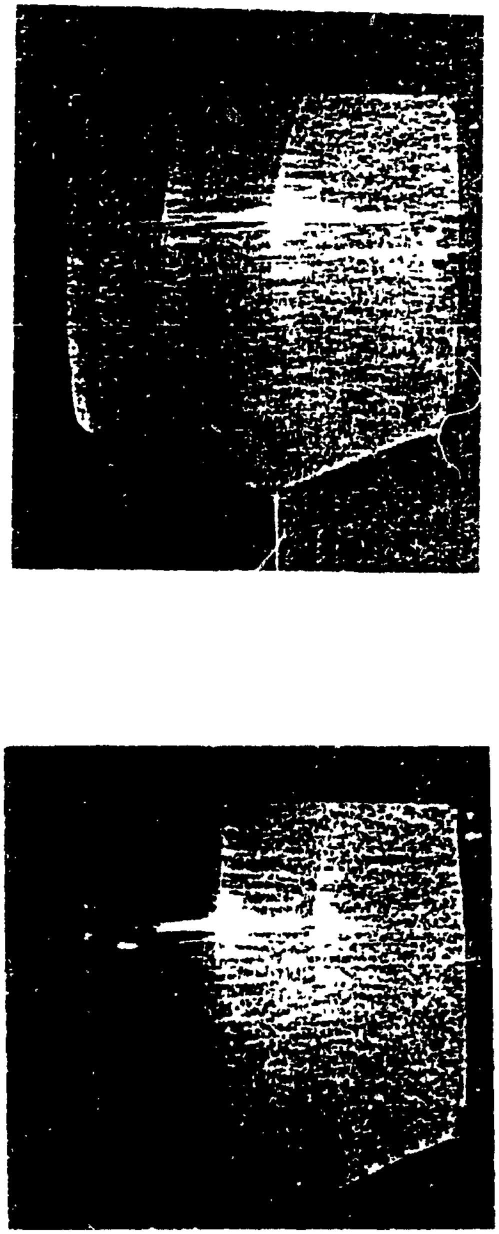

Figure 4.9: Examples of some m-lines.

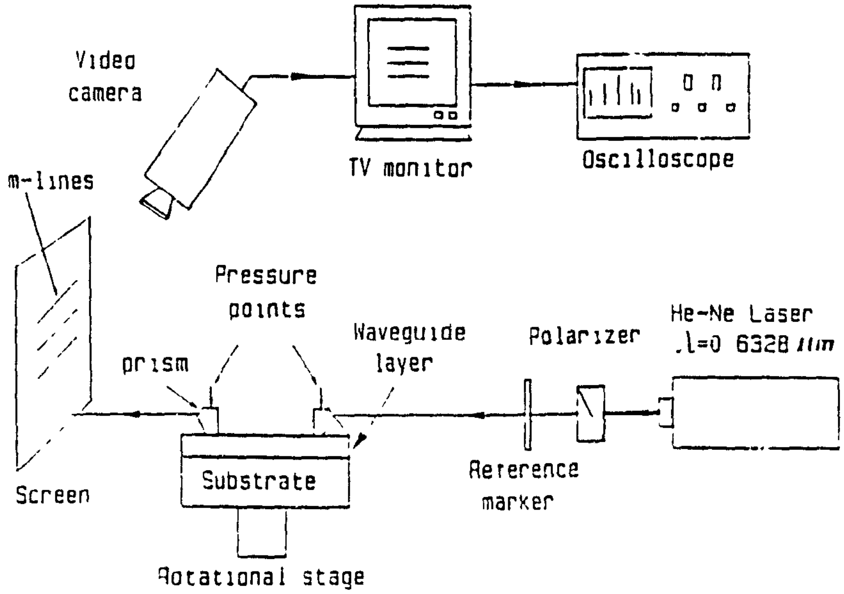

Figure 4.10: Experimental setup for measuring propagation loss

Chapter 5

Characterization of PE and APE Planar Waveguides in $LiNbO_3$

5.1 Introduction

In this chapter, an extensive characterization of proton-exchanged planar waveguides in $LiNbO_3$ is presented. The general goal of this characterization is to accurately model the waveguide properties and correlate them with the corresponding fabrication conditions. The characterization itself consists of two stages, in particular, the inital PE followed by the APE. The latter is especially important since, as was emphasized in Chapter 2, annealing is a necessary step in the fabrication of high quality waveguides. As will be seen below, some of the data reduction techniques which are used to analyze PE and APE waveguides have similar features. Consequently, the chapter begins by first introducing these techniques and then moves on to discuss the details of the two stages of the characterization.

5.2 Data reduction techniques

5.2.1 General considerations

As will become increasingly clear, an essential aspect of the characterization of both PE and APE waveguides involves finding the appropriate refractive index profile from the measured effective mode indices. To perform this task, two distinct approaches can be taken. The inverse WKB (IWKB) methods [114,115] consist of approximating the refractive index profile using piecewise linear segments. The accuracy of these techniques becomes acceptable for only very multimoded waveguides ($m \gg 5$) and for smooth index profiles. The alternative approach involves selecting a refractive index profile which, upon substitution in the appropriate waveguide dispersion relation, results in theoretical effective mode indices which agree as closely as possible with their measured counterparts. Although an obvious shortcoming of this method is that the profile must be selected in advance, its inherent statistical nature allows for it to be easily adapted to handle both single and multimode waveguides. For reasons to be elaborated upon in the subsequent section, very multimoded waveguides were not fabricated. Consequently, the latter more flexible approach to profile reconstruction must be used.

In the waveguide characterization which follows, three types of index profiles will be considered: step, Fermi, and generalized Gaussian (this choice will be justified later). These profiles are expressed in mathematical form as follows,

$$n(x) = n_b + \Delta n_s f(x) \tag{5.1}$$

where $\Delta n_s = n_s - n_b$, n_s and n_b are the surface and bulk refractive indices, respectively, and the profile shape function is given by,

$$f(x) = \begin{cases} 1 \quad (0 \le x \le d) & \text{step} \\ \left[1 - \exp\left(-\dfrac{d}{a}\right) + \exp\left(\dfrac{x-d}{a}\right)\right]^{-1} & \text{Fermi} \\ \exp\left(-\left(\dfrac{x}{d}\right)^{a}\right) & \text{generalized Gaussian} \end{cases} \tag{5.2}$$

Note that the condition $f(0) = 1$ is satisfied by all three profiles so that $\Delta n(0) = \Delta n_s$. Here, d is the depth and a is a parameter associated with the steepness of the profile. As can be seen from the above expressions, the step profile is a *two* parameter model (i.e. Δn_s, d) whereas both the Fermi and generalized Gaussian profiles are *three* parameter models (i.e. Δn_s, d, a). Although this extra parameter in the latter case increases the amount of data reduction, the greater flexibility that it offers results (as will be seen shortly) in more accurate data fitting.

5.2.2 Graded-index waveguides

The data reduction procedure begins with the manipulation of the appropriate dispersion relation discussed in Chapter 3. For a graded-index waveguide, one has (after substituting $\xi = \dfrac{x}{d}$ and $\phi_t = \dfrac{\pi}{4}$ into Eq. 3.70),

$$d = \frac{\left(m + \frac{1}{4}\right)\pi + \phi_c}{k_o \int_0^{\xi_t} \sqrt{n^2(\xi) - N_e^2 d\xi}} \tag{5.3}$$

Since this equation involves the use of the normalized coordinate, $\xi = \dfrac{x}{d}$, one must express the Fermi and generalized Gaussian profile shapes accordingly,

$$f(\xi) = \begin{cases} (1 - \delta + \delta \exp(-\xi \ln \delta))^{-1} & \text{Fermi} \\ \exp(-\xi^a) & \text{generalized Gaussian} \end{cases} \tag{5.4}$$

where $\delta = \exp\left(-\dfrac{d}{a}\right) \to a = -\dfrac{d}{\ln \delta}$ has been substituted for the Fermi function. These normalized profile shape functions are sketched in Fig. 5.1-5.2 (see the end of this chapter) for various values of δ and a, respectively. The corresponding normalized turning points are defined by $n(\xi_t) = N_e$ yielding

$$\xi_t = \begin{cases} -\ln\left(\dfrac{n_s - N_e}{\delta(N_e - n_b)} + 1\right) / \ln\delta & \text{Fermi} \\ \sqrt[a]{\ln\left(\dfrac{\Delta n_s}{N_e - n_b}\right)} & \text{generalized Gaussian} \end{cases} \tag{5.5}$$

Now, in Eq. 5.3, there are three unknowns, specifically, d, n_s, and a or δ (note that m and N_e are determined from experiment). Since the waveguide depth, d, is independent of the mode order, m, one can eliminate this variable using a mode pair to obtain,

$$\frac{\left(m_i + \frac{1}{4}\right)\pi + \phi_{c_i}}{\int_0^{\xi_{t_i}} \sqrt{n^2(\xi) - N_{e_i}^2}\,d\xi} = \frac{\left(m_j + \frac{1}{4}\right)\pi + \phi_{c_j}}{\int_0^{\xi_{t_j}} \sqrt{n^2(\xi) - N_{e_j}^2}\,d\xi} \tag{5.6}$$

where $i \neq j$ and $0 \leq m_i, m_j \leq M - 1$. Since M is the total number of modes that the waveguide supports, the number of independent equations that can be generated is

$$C_2^M = \frac{M!}{2!(M-2)!} \quad (M \geq 2) \tag{5.7}$$

Note that each of these generated equations (i.e. Eq. 5.6) still contains two unknowns (n_s, a or δ). The approach used to determine them involves inputting a range of a or δ values in all these equations and then solving for the various n_s values (This has the effect of reducing the dimension of the root search to one). The corresponding d values are then computed from Eq. 5.3 (For the Fermi profile, a is then found from $a = -\dfrac{d}{\ln\delta}$). The value of a resulting in the smallest standard deviation in n_s and d is deemed the best or optimized value and is denoted by a_{opt}. Of course, in order for this optimization procedure to be effective, a waveguide which supports at least three modes is needed. For two mode waveguides, a and n_s are chosen which agree as closely as possible with the optimized values obtained from waveguides with $M \geq 3$. The assumption here is that the surface index (n_s) and the profile shape (a) are independent of the waveguide depth (The validity of this assumption will be examined later). For single mode waveguides, the average [1]

---

[1] The average values are computed as follows: $a_{avg}, n_{s_{avg}} = \left\{\sum_{k=1}^{N} (C_2^M)_k (a_{opt}, n_{s_{avg}})_k\right\} / N$. Here k refers to a particular waveguide sample and N is the total number of multimode waveguides

value of a and n_s determined from the multimode samples is used to compute the corresponding depth from Eq. 5.3.

5.2.3 Step-index waveguides

For the step-index profile, the corresponding dispersion relation is given by (see Chapter 3),

$$d = \frac{m\pi + \phi_c + \phi_s}{k_o\sqrt{n_f^2 - N_e^2}} \tag{5.8}$$

which upon eliminating d becomes,

$$\frac{m\pi + \phi_{c_i} + \phi_{s_i}}{k_o\sqrt{n_f^2 - N_{e_i}^2}} = \frac{m\pi + \phi_{c_j} + \phi_{s_j}}{k_o\sqrt{n_f^2 - N_{e_j}^2}} \tag{5.9}$$

Since the step profile is a two parameter model, the only unknown in Eq. 5.9 is the film index, n_f, which can be obtained by a simple root search. The depth is then found from Eq. 5.8. As before, the average value of n_f obtained from all the mode pairs of the multimode samples is used to compute the depth for single mode waveguides. Note that the simple step profile does not require any optimization procedure as was the case with the three parameter graded-index models.

With the index profile parameters determined, one can readily replace $n(x)$ in the appropriate dispersion relation (i.e. Eq. 5.3 or Eq. 5.8) and generate the important theoretical dispersion curves and compare them to the measured data.

5.3 Characterization of PE planar waveguides

5.3.1 Introduction

When this work began, published studies on the use of pyrophosphoric acid ($H_4P_2O_7$) as an alternative proton source in the PE process were preliminary and incomplete [25,26]. Originally proposed by Yamamoto et al. [24], this acid was found to result in higher index increases and lower losses compared to benzoic acid (C_6H_5COOH)

which had been the focus of previous PE studies [19,21,22,23]. Parallel to this, the accuracy of the conventional step-index PE waveguide model was being questioned [27]. Hence, the aim of the first stage of the characterization (i.e. initial PE) is twofold:

1. To accurately model the refractive index profile in PE waveguides and thus assess the validity of the conventional step-index assumption.
2. To address the controversy about the supposedly higher index increases associated with pyrophosphoric acid as compared to benzoic acid (Although a thorough investigation of propagation loss was not part of the aim of this study, some preliminary results will be presented in the section dealing with annealing).

In addition to parts of this characterization [34,35] which have been reported elsewhere, more recent studies [20,54,55,56,77,116] have been performed resulting in improving the understanding of the PE process.

The fabrication parameters that can be varied in the PE process include:

- type and strength of proton source (eg. pure or diluted benzoic and pyrophosphoric acids)
- particular cut substrate (eg. x, y, or z)
- process technique (eg. spin coating, surface coating, or immersion)
- exchange temperature (T)
- exchange time (t)
- exchange environment (eg. sealed beaker or flowing wet O_2)

A total of fifteen z-cut $LiNbO_3$ waveguides were fabricated using the surface coating technique described in detail in the previous chapter. Pure pyrophosphoric acid was used as the proton source. Since annealing was subsequently studied in detail, an investigation into dilute melts was not performed. The exchange temperatures and times ranged from 200^oC to 260^oC and 15 minutes to 4 hours, respectively. Note that the temperature range used is well above the quoted minimum temperature [46] associated with PE for this particular cut crystal ($T_{min} \approx 140^oC$) and below the boiling point of pyrophosphoric acid ($T_b = 300^oC$) [24]. Very long exchange times (which are needed to produce very multimoded waveguides) were avoided for a number of reasons including:

- The pyrophosphoric acid was found to degrade as evidenced by its discoloration resulting in a black residue on the surface of the sample. This degradation which is believed [117] to be caused by impurities in the form of polyphosphoric acids is an important factor that needs to be considered as far as the reproducibility and, hence, quality of the fabrication process is concerned.
- Due to the small volumes of acid used in the surface coating technique (typically $\approx 0.1\ ml$), some annealing and/or melt dilution effects may occur resulting in changes in the refractive index profile [77].
- Larger stresses in the waveguide layer (associated with the larger exchange depths) may also result in changes in the refractive index profile [63,118].

The last two reasons point to the need for being careful about extending very multimoded ($m \gg 5$) waveguide results to the important single mode region within which the majority of optical waveguide devices operate. In the characterization which follows, $m \leq 5$ and, consequently, the assumption that the surface index increase (Δn_s) and the profile shape ($f(x)$) are independent of the exchange depth (i.e. time) but not necessarily of temperature is made [108]. This assumption allows one to generate the important dispersion curves discussed in the previous section.

5.3.2 Calculation of dispersion curves

The prism coupler technique described in the previous chapter was used to measure the effective mode indices. Only TM modes were observed to propagate supporting the contention that only the extraordinary index of refraction increases. The results for each exchange temperature are given in Table 5.1 (see the end of this chapter).

Dispersion curves were calculated for both a Fermi and step-index profile and are shown in Fig. 5.3-5.5. Note that the use of the three parameter Fermi model here was motivated by earlier work [27] which found improvement in the data fitting of PE waveguides using a more complicated four parameter modified Fermi function. The Fermi index profile parameters (i.e. d, n_s, a) for each sample are given in Table 5.2. Maximum computing time required on an IBM AT compatible is 2 and 20 minutes for the step and Fermi profiles, respectively. The extra computing associated with the Fermi profile, however, results in an improved fit to the measured effective mode indices. In particular, the average difference between the measured (39 data points) and calculated theoretical effective mode indices was found to be $(27.7 \pm 22.4) \times 10^{-4}$ and $(17.5 \pm 15.9) \times 10^{-4}$ for the step and Fermi profiles, respectively.

Besides being less accurate, the step profile was found to slightly underestimate the surface index increase for higher exchange temperatures. For example at $T = 230^{o}C$, $\Delta n_s = 0.129$ (step) and 0.132 (Fermi). Although Goto and Yip [54] (who used a similar surface coating technique) reported $\Delta n_s = 0.131$ (step) for $T = 200^{o}C$ which is consistent with the above, these results are considerably different from the values $\Delta n_s = 0.145$ (IWKB) initially reported by Yamamoto et al. [25] and $\Delta n_s = 0.124$ (step) and 0.145 (IWKB & polynomial) recently reported by Pun et al. [116]. Although the immersion process technique was used in the latter study, the work of Loni et al. [77] has shown that the index increase is independent of the process technique used with magnitude 0.131-134 (step) which agrees with the values in Table 5.2. As for the controversy about the discrepancies observed between benzoic and pyrophosphoric acids, the index increases reported here for pyrophosphoric acid ($\Delta n_s = 0.131 - 132$) are greater than those reported for benzoic acid [21,22,23] ($\Delta n_s = 0.126 - 127$). This moderate increase associated with pyrophosphoric acid is believed to be due to higher proton concentrations in the waveguide layer resulting from the larger dissociation constant of pyrophosphoric acid [25,77].

The discussion has so far concentrated on modeling the extraordinary index profile ($n_e(x)$). In Chapter 3, a technique based on the optimization of the anisotropic PE step-index TM dispersion relation was proposed as a method to determine to a first approximation the decrease (if any) in the ordinary index (n_o), an increasingly important characterization parameter especially in light of a recent proposal to fabricate TiPE buried waveguides. A similar approach has been used successfully by Yip and Colombini [91] (In their study, however, the optimization was simpler since both TE and TM modes were involved). As emphasized earlier, the success of the technique is dependent on using a very multimoded waveguide since discrepancies between the isotropic and anisotropic step-index models only become significant for $m \geq 4$. Unfortunately, the use of samples # 14 ($m = 4$) and # 15 ($m = 5$) resulted in discrepancies in the waveguide parameters which were within the experimental error. Consequently, conclusive estimates on the value of Δn_o could not be obtained. These results, however, further support the contention made in Chapter 3 that the neglect of the uniaxial anisotropy in PE waveguides is justified as long as the waveguide is not very multimoded (i.e. $m \gg 4$). Although they were not investigated, the use of the immersion process technique (which can result in waveguides with $m \gg 4$ since acid degradation is not as rapid [117]) as well as more accurate index measurement techniques such as Maker fringes interferometry [17] could lead to more conclusive data. The simple statistical nature of this technique contrasts with the rather involved experimental procedure used by De Micheli et al. [45] who found $\Delta n_o \approx -0.04$ for benzoic acid.

5.3.3 Correlating (Δn_s, d, a) with (T, t)

In this section, various empirical relationships are introduced which allow one to specify waveguide parameters (Δn_s, d, a) from arbitrary fabrication conditions (T, t). In Chapter 2, it was mentioned that PE waveguide depths have been found [21,22,26] to be proportional to $\sqrt{t}$. In order to verify this, plots of d versus $\sqrt{t}$ were made for each temperature and are shown in Fig. 5.6. Although the linear relationship is confirmed, the least squares fits do not go through the origin. This is due [54] to the fact that the substrate and acid were *not* preheated to the required exchange temperature (see Chapter 4). To take into account this factor, a warm-up time parameter, t_w, which depends on the particular fabrication setup used is introduced so that,

$$d = \sqrt{D_e}(\sqrt{t} - \sqrt{t_w}) \quad t > t_w \tag{5.10}$$

Table 5.3 lists the computed effective diffusion coefficients (D_e) for each temperature with the corresponding waveguide parameters. The average warm-up time was found to be $t_w \approx 0.15 hr$ (or about 9 minutes). Note that the results for $T = 200^o C$ are in excellent agreement with those reported by Goto and Yip [54]. The temperature dependence of D_e is determined by expressing [22,68,108] it in Arrhenius form (see Chapter 2),

$$D_e = C_1 \exp\left(-\frac{C_2}{T}\right) \tag{5.11}$$

A plot of $\ln D_e$ versus T^{-1} is shown in Fig. 5.7. Using linear regression, one finds C_1 and C_2 to be $2.62716 \times 10^7 \frac{\mu m^2}{hr}$ and $8.276 \times 10^3 \, ^o K$, respectively (where K stands for Kelvin). By substituting Eq. 5.11 into Eq. 5.10, one obtains the following useful design equation,

$$d = \sqrt{C_1}\exp\left(-\frac{C_2}{2T}\right)(\sqrt{t} - \sqrt{t_w}) \quad t > t_w \tag{5.12}$$

The use of this expression along with the results given in Table 5.3 allows one to determine the refractive index profile for any exchange temperature and time within the characterized ranges.

In the literature, the constant C_2 is sometimes alternatively expressed [22,26,77] as the ratio $\frac{Q}{R}$ where Q is the so-called activation energy for the PE process and $R = 8.31\frac{J}{mole\cdot{}^\circ K}$ is the universal gas constant. Hence, for the above data, $Q = C_2R \approx 69\frac{kJ}{mole}$. Using a spin coating process technique, Yamamoto et al. [26] found that $C_1 = 1.02 \times 10^{10}\frac{\mu m^2}{hr}$ and $Q = 95\frac{kJ}{mole}$ which is in excellent agreement with the values $C_1 = 7.36 \times 10^9\frac{\mu m^2}{hr}$ and $Q = (88 - 94)\frac{kJ}{mole}$ reported for benzoic acid (immersion process technique). This, however, contradicts the recent results of Loni et al. [26] who found that the diffusion coefficients for surface and spin coated samples were smaller than those obtained by immersion. Moreover, they also found that immersion in pyrophosphoric and benzoic acids yielded similar diffusion coefficients. This suggests that C_1 (surface or spin coating)$<$ C_1 (immersion in pyrophosphoric or benzoic acids). The value of C_1 reported above for this characterization is consistent with this. Since, in addition, differences between the acid and furnace temperatures (the latter was used in this work) may result [46] in some discrepancies in Q as well as the fact that the diffusion coefficients (and, hence, Q) are affected by the specific exchange environment and the process technique used [77], the approximately 25 % smaller value reported here is not unreasonable. Indeed, large discrepancies (60 %) in the Q values have been recently reported for pyrophosphoric and benzoic acid PE in $LiTaO_3$ [121,122].

As a final comment, the reproducibility of the above results was investigated by fabricating 2 single mode waveguides (# 19 and # 22 in Table 5.4-5.6 in the next section) under similar conditions (i.e. same exchange temperature and time).

Although the resulting discrepancies in the measured effective mode indices was $\pm 3 \times 10^{-3}$ which is greater than the experimental error ($\sim 5 \times 10^{-4}$), the corresponding differences in the calculated depth was less than 5 % which is quite good. Factors which may contribute to some of these discrepancies include:

- Since pyrophosphoric acid is sensitive to humidity, the proton source (which is exposed to air during the fabrication process) will also contain varying quantities of orthophosphoric acid which has a slightly smaller dissociation constant. As a result, the exact composition of the proton source is unknown [55].
- As the acid warms up to the set exchange temperature, it becomes less viscous resulting in some of it flowing off the surface of the substrate. This may lead to a nonuniform coat and, hence, a nonuniform diffusion as evidenced by the recently reported slight variation of N_e along the waveguide path [77].
- The warming and subsequent cooling of the substrate and acid result in some inaccuracies in the determination of the precise exchange temperature and time [123].

The reproducibility question is an important one since the design of some optical devices may be sensitive to small changes in the waveguide parameters caused by slight variations in the fabrication conditions [119,124]. In any case, this characterization has shown that the PE process is a simple and convenient technique for the fabrication of optical waveguides whose properties are (for the most part) reproducible and can be accurately modeled and correlated with arbitrary fabrication conditions.

5.4 Characterization of APE waveguides

5.4.1 Introduction

In Chapter 2, it was pointed out that the APE technique holds certain distinct advantages (eg. reduced fabrication time and complexity, greater flexibility in tailoring of index profile) over the use of buffered melts in the fabrication of high quality waveguides. Hence, it is desirable to accurately characterize it. In the past, the focus of the majority of studies [30,31,32,33] has been on improving waveguide loss and restoring the electro-optic coefficients. Although some attempts [19,21,44,46,54,62,125,127,128] have been made to correlate some fabrication parameters with measured index profiles, the studies are again incomplete. Moreover, these index profiles have generally been modeled by either inverse WKB methods [21,46,128] (which as was discussed earlier become accurate for only very multimoded waveguides) or simple analytic functions [19,44,54] (eg. step, Gaussian, exponential, etc.). Modeling techniques to accurately quantify, for example, the step to Gaussian and Gaussian to exponential transition regions are still lacking. The purpose of the second stage of this characterization then consists of the following:

1. To gain a better understanding of the anneal process by considering a more extensive range of fabrication conditions.
2. To develop more accurate and flexible APE refractive index profile modeling techniques.

Note that some of the work presented below has been reported elsewhere [35,36].

As in the PE process, several fabrication parameters can be varied in the APE process. These include:

- initial PE fabrication conditions (t, T)

- particular cut substrate (eg. x, y, or z)
- anneal temperature (T_a)
- anneal time (t_a)
- anneal environment (eg. wet or dry flowing O_2)

Using the fabrication procedure discussed in Chapter 4, initially single and multimode z-cut PE waveguides were made and subsequently annealed for times and at temperatures ranging from 15 minutes to 16 hours and 200^oC to 400^oC, respectively. For convenience, the initial exchange temperature was fixed at $T = 200^oC$. The chosen anneal temperature range reflects the fact that little change in the waveguide properties has been observed [21,44] to occur for $T_a < 200^oC$ while, for $T_a \geq 500^oC$, the surfaces of the waveguide samples have been found [62,63] to cloud over indicating that substantial surface damage has occurred. This damage is believed to be associated with the formation of Li deficient phases (eg. $LiNb_3O_8$) in the waveguide layer. Interestingly, in this study, the use of pyrophosphoric acid as the proton source was found to result in such surface damage for <u>all</u> samples annealed at $T_a = 400^oC$ for $t_a > 2$ hours. Although previous work involving benzoic acid has demonstrated annealing at $T_a = 400^oC$ for as much as $t_a = 16$ hours [19], the initial thicknesses (d_o) of the PE waveguides used was much greater ($d_o \geq 2.6\mu m$) than those used here ($d_o \leq 1.3\mu m$). A similar phenomenon (i.e. discrepancies in the progressive surface damage in thin and thick waveguides) has been reported [62] for annealing at $T_a = 500^oC$.[2] In addition, it has been recently found [20,54] that the properties of annealed waveguides are dependent on the initial PE exchange depth. These results again underscore the importance of exercising caution when modeling the waveguide properties of thin and thick waveguides.

---

[2] Since the properties of APE waveguides have been observed [19] to be affected by the particular anneal environment, it is possible that the flow rate as well as the water content of the O_2 used was not sufficient enough to prevent deoxidization. Such optimal anneal environment conditions, however, have not been reported.

5.4.2 Dispersion curves and single mode design considerations

As before, the prism coupler technique was used to measure the TM effective mode indices (see Table 5.4-5.6). Note that the table entry under $t_a = 0$ corresponds to the initial PE (i.e. before annealing). The dispersion curves, in particular, the evolution of the effective mode indices with anneal time for the various samples are illustrated in Fig. 5.8-5.14. Some of the salient features of the multimode plots include:

- The fundamental (i.e. $m = 0$) effective mode index decreases with anneal time indicating that the surface index is decreasing. After a sufficient anneal time, all the effective mode indices begin to decrease.
- The number of modes increases after a sufficient annealing period indicating that the depth of the waveguide is increasing faster than the surface index is decreasing (Recall from Chapter 3 that the number of modes supported by a waveguide is proportional to d and Δn_s).
- Most of the changes in the effective mode indices (and, hence, the refractive index profile) occur within the first two hours of annealing with the largest changes occurring for $T_a = 400^oC$.

These observations are consistent with those previously reported [46,54,125]. As for the (initially) single mode plots given in Fig. 5.12-5.14, they reveal that, although the annealing process generally results in an increase in the number of modes, one can extend the region of single mode behaviour by appropriately chosing the initial PE depth (d_o). It was found that d_o had to be decreased as T_a increased (see Table 5.7). A similar study carried out by Goto and Yip [54,105] for $T_a = 300^oC$ shows good agreement with what has been reported here for the same temperature. Interestingly, for $T_a = 400^oC$, the value of $d_o = 0.20\mu m$ was just below the cutoff of the fundamental mode (i.e. a mode was not supported initially). Even at $T_a = 200^oC$, considerable flexibility in the tailoring of the effective index is possible (see Fig. 5.12). Note that in addition to tailoring the effective mode index, the use of annealing allows for the relaxation of the tight fabrication tolerances that would otherwise be required in the fabrication of single mode *channel* waveguides [56,126,124].

5.4.3 Modeling the refractive index profile

The previous section discussed some of the qualitative features associated with the annealing process, in particular, a general increase in the waveguide depth with a corresponding decrease in the surface index. In order to quantify these changes, the evolving refractive index profile with anneal tim[illegible]s to be modeled accurately. To do this, the generalized Gaussian function an[illegible]ed in detail in section 5.2 is used. As can be seen from Fig. 5.2, the advantages of using this function include:

- a relatively simple analytic form (contrast this with the more complicated error function model proposed previously [20,120])
- tremendous flexibility in its ability to represent a wide range of functions (for example, the values $a = 1, 2, \gg 10$ refer to the exponential, Gaussian, and step profiles, respectively)
- optimization procedure allows one to accurately quantify the important transition regions (eg. step to Gaussian, Gaussian to exponential, etc.)

The computed optimized waveguide parameters for the various fabrication conditions are given in Table 5.8 (Maximum computing time was 20 minutes as before). The effect of anneal temperature and time on the value of a_{opt} (which is associated with the shape of the profile) is shown in Fig. 5.15 These plots show that while the profile remains step-like (i.e. $a_{opt} \gg 10$) for $T_a = 200^oC$ throughout the entire annealing period, the corresponding profile for $T_a = 400^oC$ becomes Gaussian after only one half hour of annealing and then progressively approaches an exponential. As for the intermediate anneal temperature of $T_a = 300^oC$, although the profile retains its step nature initially, it increasingly becomes graded approaching a Gaussian only after long periods of annealing (Note that even after $t_a = 12hrs$, the optimized profile with $a_{opt} \approx 3$ has still not become completely Gaussian).

The evolution of the index profiles with anneal temperature and time are shown in Fig. 5.16-5.19. These plots reveal excellent agreement between the optimized profiles (solid curves) and the experimental data (solid symbols). The dotted curves represent the step and Gaussian approximations that have been used in the past [44,54]. Note in particular the large discrepancies (which can be as much as 20%) between these approximations and the optimized profiles for $T_a = 300^oC$ and (to a lesser degree) $T_a = 400^oC$. The changes in the corresponding waveguide depth and surface index are shown in Fig. 5.20-5.21. The kink in the $T_a = 300^oC$ (dotted) curves at $t_a = 8hrs$ is due [54] to the fact that the approximation used has changed from step to Gaussian (A similar although smaller kink can be observed in the data recently reported by Wong [118] who used an IWKB method). By contrast, this phenomenon is absent in the optimized curves which is consistent with the physical observation that the annealing process generally results in the smoothing [62,128] of the hydrogen concentration (and, hence, the refractive index) profile. As can be seen from Table 5.6, the computed index and depth changes were $0.018/0.49\mu m$, $0.041/0.95\mu m$, and $0.079/2.53\mu m$ for $T_a = 200^oC$ ($t_a = 16hrs$), $T_a = 300^oC$ ($t_a = 12hrs$), $T_a = 400^oC$ ($t_a = 2hrs$), respectively, showing that considerable flexibility exists (especially at higher anneal temperatures) in the tailoring of the waveguide parameters. A tradeoff exists, however, because the larger changes in the waveguide parameters associated with higher temperature annealing may be more difficult to control accurately. Note that, although the optimal fabrication parameters (T_a, t_a) have not been conclusively established, there have been recent reports [32,47] of the fabrication of high quality (i.e low loss, good electro-optic behaviour, etc.) APE waveguides for $300^oC \leq T_a \leq 360^oC$ and $1hr \leq t_a \leq 3hrs$. It is in this intermediate T_a range where the significant improvement in the flexibility and accuracy provided by the above model can be taken full advantage of.

5.4.4 Nonlinear dependence of index on concentration

Another interesting point that has not as of yet been addressed is the common feature that the area under the evolving refractive index profile curves does *not* remain constant. As mentioned in Chapter 2, this phenomenon has been attributed [56,64] to a nonlinear dependence of the extraordinary refractive index and the hydrogen concentration. To investigate this more closely, consider the mathematical expression for the area,

$$\begin{aligned} \text{area} &= \int_0^\infty \Delta n(x)\, dx \\ &= \Delta n_s \int_0^\infty f(x)\, dx \\ &= \Delta n_s \int_0^\infty \exp\left(-\left(\frac{x}{d}\right)^a\right) dx \end{aligned} \tag{5.13}$$

By substituting $u = \left(\frac{x}{d}\right)^a$, one can express the above integral in terms of the well known *Gamma* function, Γ, as follows,

$$\text{area} = \Delta n_s \frac{d}{a} \Gamma\left(\frac{1}{a}\right) \tag{5.14}$$

$$\Gamma(\beta) = \int_0^\infty u^{\beta-1} \exp(-u)\, du \tag{5.15}$$

Note that since from Table 5.8 $1.4 \leq a \leq 40$, the corresponding values of $a^{-1} \ll 1$. To bring the argument of Γ to a more practical range (say $1 \leq \beta \leq 2$), one can use the familiar [129] recurrence relation $\Gamma(\beta+1) = \beta\Gamma(\beta)$ so that $\Gamma\left(\frac{1}{a}\right) = a\Gamma\left(\frac{1}{a}+1\right)$.

Using the results from Table 5.8, the evolution of the area with anneal temperature and time was computed and is plotted in Fig. 5.22. The plot shows that the area increases after the first anneal period (i.e $t_a = 0.5hr$) and steadily decreases afterward (For $T = 200°C$, the decrease occurs only after $t_a = 8hrs$). In addition to the nonlinear dependence of index on concentration, this decrease has recently been attributed to a concurrent process of hydrogen outdiffusion [123]. Note that the simple analytic form of the generalized Gaussian profile has led to a correspondingly simple expression for the area which readily allows for the verification of this nonlinear behaviour. This result again underscores the tremendous flexibility that the generalized Gaussian model offers.

5.4.5 Correlating (Δn_s, d, a) with (T_a, t_a)

As in the PE characterization, empirical relationships are introduced here which allow one to correlate the changes in the waveguide parameters (Δn_s, d, a) with the corresponding fabrication conditions (T_a, t_a). Although it was shown earlier that PE waveguide depths are proportional to $\sqrt{t}$, it is not clear that such a relationship should hold here. Hence, the following more general power law is used,

$$\frac{d}{d_o} - 1 = b\, t_a^c \tag{5.16}$$

$$1 - \frac{\Delta n_s}{\Delta n_{s_o}} = p\, t_a^q \tag{5.17}$$

where

d_o = initial PE depth

Δn_{s_o} = initial surface index increase

b, c, p, q = fitting parameters

The above equations were fitted[3] to the data obtained for $T_a = 300°C$ and $400°C$ (see Table 5.9) and are plotted in Fig. 5.23-5.24 (For $T_a = 200°C$, the changes in

---

[3] The fitting procedure involved performing a least squares nonlinear regression on the given data [75].

the waveguide parameters were relatively small). These results reveal that since $c, q\,(T_a = 300^oC) \ll c, q\,(T_a = 400^oC)$, the waveguide mechanisms associated with each temperature are different. It has been proposed (see Chapter 2) that the graded-index profiles arising from high temperature annealing (i.e. $T_a \gg 200^oC$) suggest that simple diffusion mechanisms are at work. To verify this, the technique described at the end of Chapter 2 was used to convert the theoretical concentration profile ($\alpha = 0$ for simple diffusion) to its corresponding index profile which was then compared to the measured profiles. The results are illustrated in Fig. 5.25-5.26. For $T_a = 400^oC$, the simple diffusion model predicts the changes in the surface index quite accurately. Discrepancies, however, exist in the shapes of the profiles. For $T_a = 300^oC$, there is very little agreement between theory and experiment. These results not only support the contention that the diffusion mechanisms are different for the different temperatures but, also, show that more complicated mechanisms are at work even at $T_a = 400^oC$. It may be possible to obtain better agreement between theory and experiment by using the nonlinear diffusion model (i.e. $\alpha \neq 0$) since the latter possesses an extra fitting parameter (α). This, however, was still being investigated at the time of writing of this thesis.

Referring back to the empirical relationships used to model the experimental data, it is natural to wonder about the validity of extending these relationships to the important single mode region since, as was pointed out earlier, discrepancies in the annealing of thin and thick waveguides have been found [20,54]. To investigate this, the two multimode waveguides (#23 and #24) annealed at $T_a = 400^oC$ were compared (see Table 5.6) yielding changes in the waveguide depth and surface index after $t_a = 2hrs$ of $2.53\mu m$ (221 % increase)/0.079 (59 % drop) and $2.52\mu m$ (293 % increase)/0.085 (65 % drop) for $d_0 = 1.14\mu m$ and $0.86\mu m$, respectively. The greater changes occurring in the thinner waveguide is consistent with not only what has been previously reported but, also, with all the APE concentration models discussed in Chapter 2. Consequently, one expects that thinner single mode waveguides would be characterized by even greater changes (which, unfortunately, would be impossible to determine from simple mode index measurements). This observation then must be kept in mind when using the numbers given in Table 5.7.

One final comment concerns propagation loss which is another important waveguide parameter. Although, as was mentioned in the introduction, an investigation into waveguide loss was not part of the aim of this characterization, some preliminary data obtained using the 2 prism-sliding method (described in Chapter 4) is given in Table 5.10. As pointed out in Chapter 2, a correlation of fabrication parameters with waveguide loss has not as of yet been conclusively established. Parallel to this, the controversy about lower losses associated with pyrophosphoric acid compared to benzoic acid has still not been settled. Clearly, more work needs to be done in this area. Such data would complement the above characterization (which has concentrated on refractive index profile modeling) and thus help in better optimizing the waveguide properties of PE devices.

To conclude, this characterization has shown that the annealing process allows for considerable flexibility in the tailoring of the refractive index profile which can be accurately modeled and correlated with the corresponding fabrication conditions.

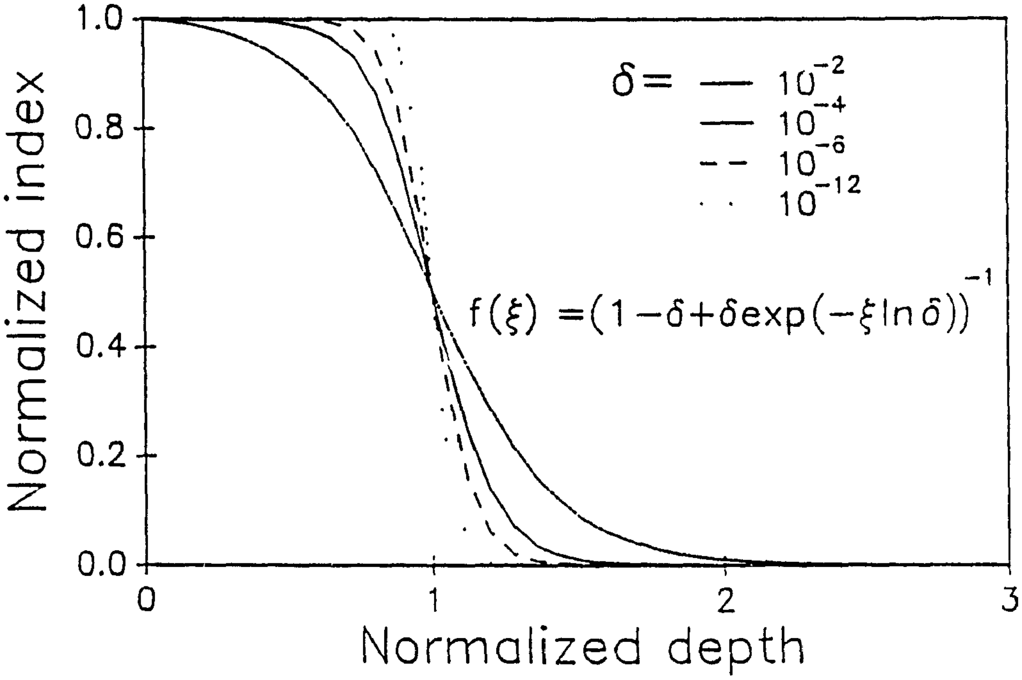

Figure 5.1: Effect of δ on the shape of the normalized Fermi index profile.

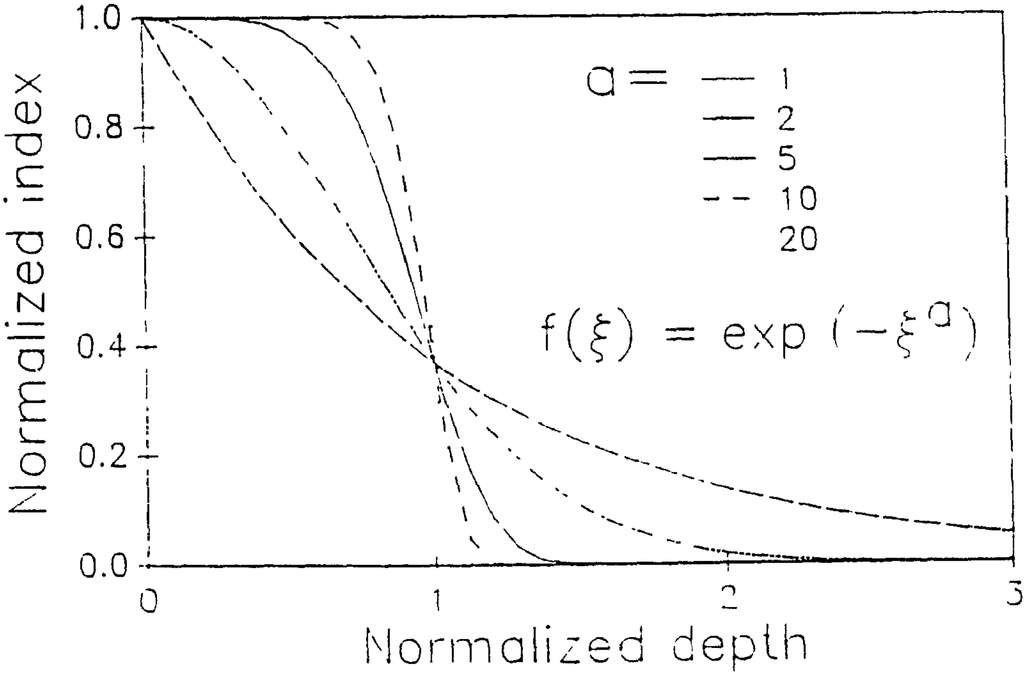

Figure 5.2: Effect of a on the shape of the normalized generalized Gaussian profile.

Table 5.1: TM effective mode index measurements.

T ($^{\circ}C$)	Sample #	t (min)	TM0	TM1	TM2	TM3	TM4	TM5
200	1	30	2.2093					
	2	60	2.2765					
	3	90	2.2974	2.2154				
	4	120	2.3085	2.2472				
	5	210	2.3213	2.2855	2.2323			
230	6	30	2.2203					
	7	60	2.3019	2.2298				
	8	90	2.3146	2.2675				
	9	140	2.3192	2.2806	2.2299			
	10	180	2.3249	2.2944	2.2598	2.2109		
260	11	15	2.2087					
	12	45	2.3166	2.2772	2.2225			
	13	64	2.3212	2.2879	2.2466			
	14	90	2.3282	2.3045	2.2817	2.2468	2.2037	
	15	120	2.3346	2.3182	2.2919	2.2703	2.2447	2.2156

Table 5.2: Computed waveguide parameters for a Fermi index profile.

T ($^\circ C$)	Sample #	t (min)	d (μm)	n_s	a_{opt} (μm)
200	1	30	0.2620	2.3312	0.0745
	2	60	0.5495	2.3312	0.0745
	3	90	0.7303	2.3305	0.0737
	4	120	0.9283	2.3300	0.0806
	5	210	1.2899	2.3318	0.0728
230	6	30	0.2916	2.3318	0.0998
	7	60	0.8071	2.3317	0.0917
	8	90	1.1089	2.3315	0.1046
	9	140	1.2696	2.3315	0.1056
	10	180	1.5443	2.3320	0.0974
260	11	15	0.1870	2.3312	0.1355
	12	45	1.2197	2.3312	0.1050
	13	64	1.4336	2.3309	0.1265
	14	90	1.9046	2.3312	0.0842
	15	120	2.4347	2.3312	0.1776

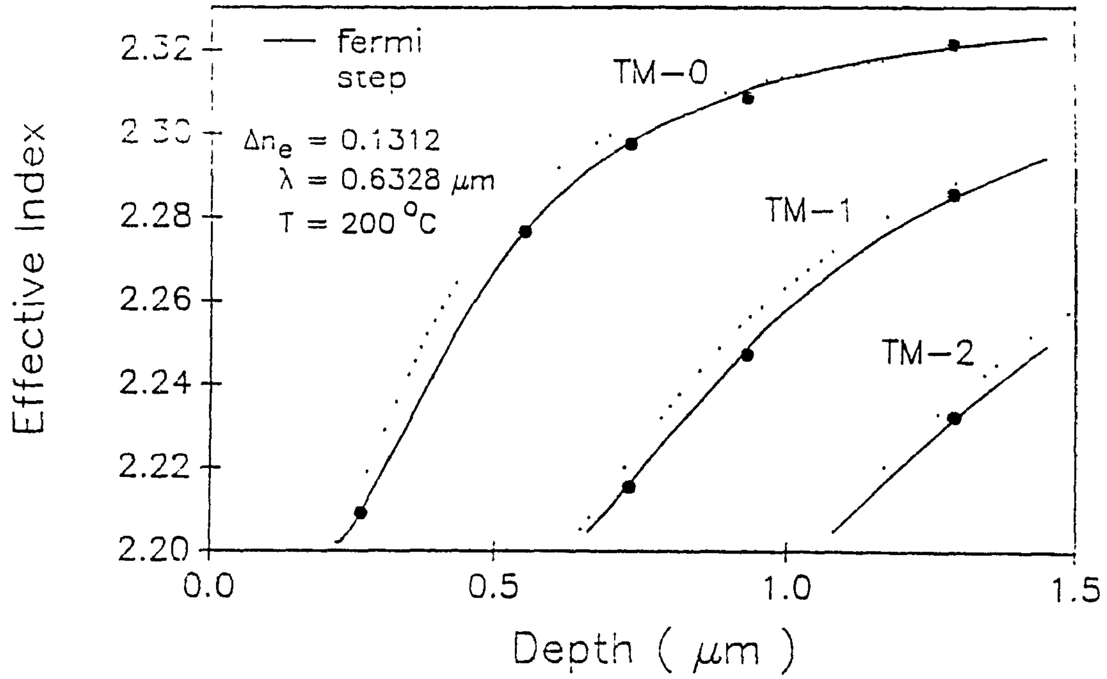

Figure 5.3: Comparison between Fermi and step-index dispersion curves and experiment (•) for $T = 200^oC$.

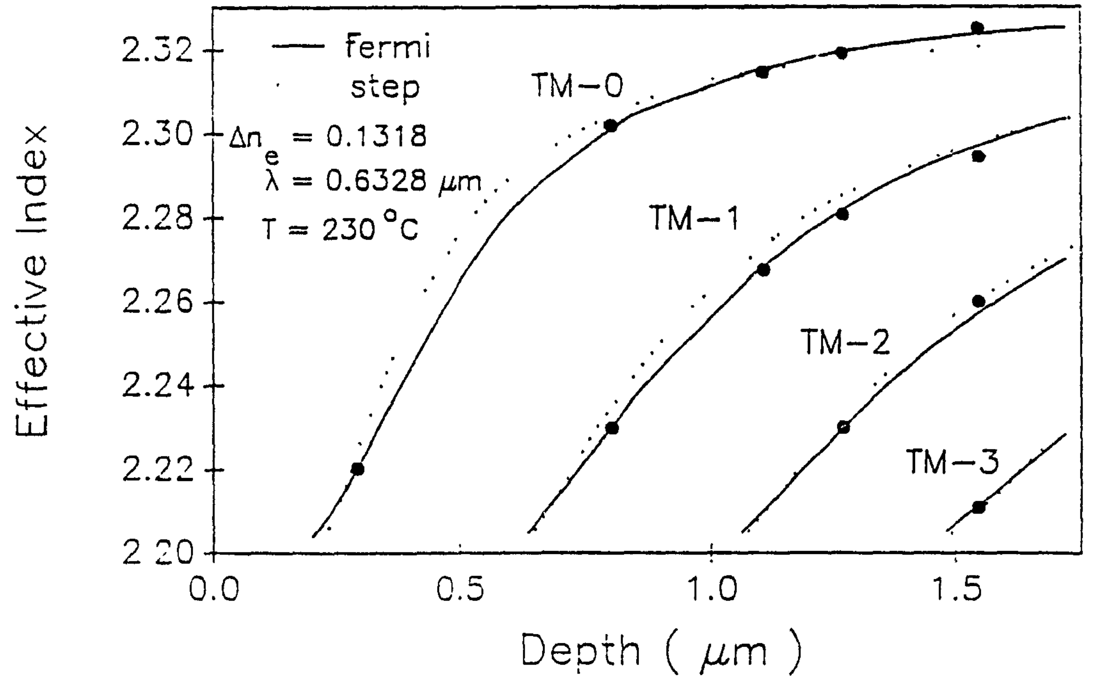

Figure 5.4: Comparison between Fermi and step-index dispersion curves and experiment (•) for $T = 230^oC$.

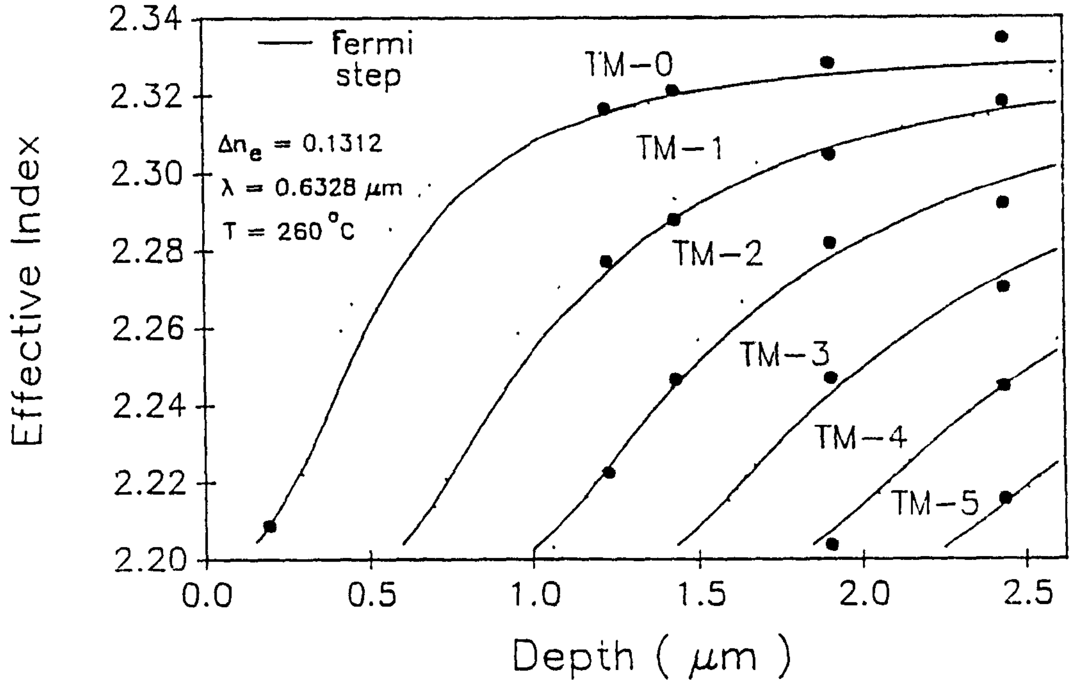

Figure 5.5: Comparison between Fermi and step-index dispersion curves and experiment (•) for $T = 260°C$.

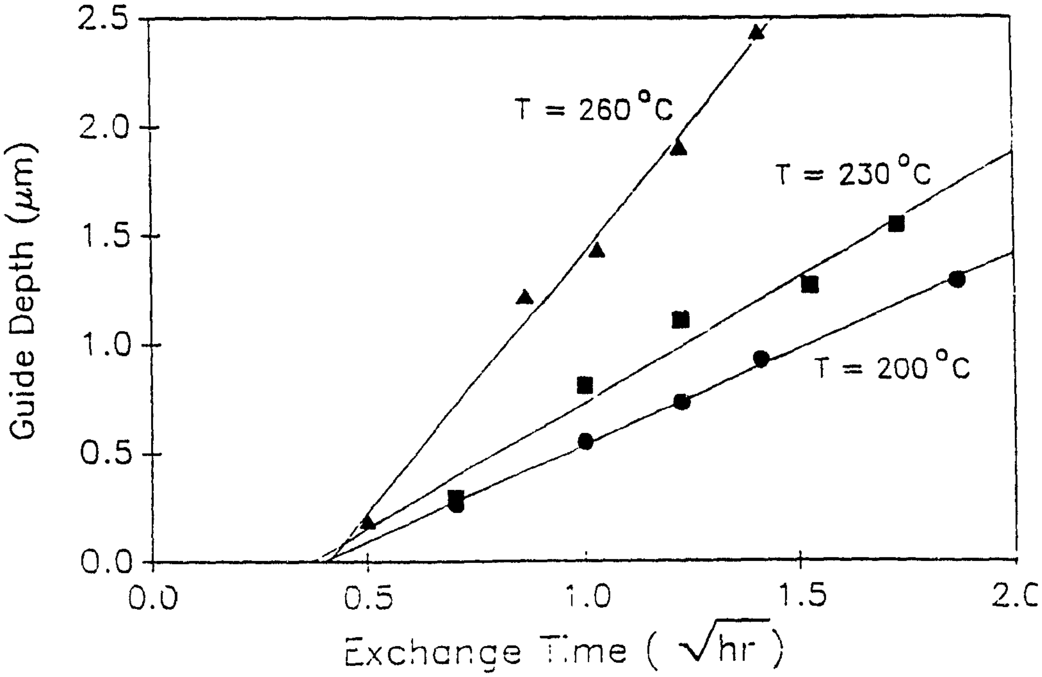

Figure 5.6: Guide depth versus square root of exchange time. Slope of least squares fit (——) yields effective diffusion coefficient (D_e).

Table 5.3: Temperature dependence of effective diffusion coefficient and corresponding waveguide parameters.

T ($^\circ C$)	D_e $\left(\frac{\mu m^2}{hr}\right)$	$\Delta n_{s_{avg}}$ (Fermi)	a_{avg} (μm)	$\Delta n_{s_{avg}}$ (step)
200	0.7797	0.1312	0.0745	0.1307
230	1.3248	0.1318	0.0998	0.1289
260	5.7073	0.1312	0.1355	0.1288

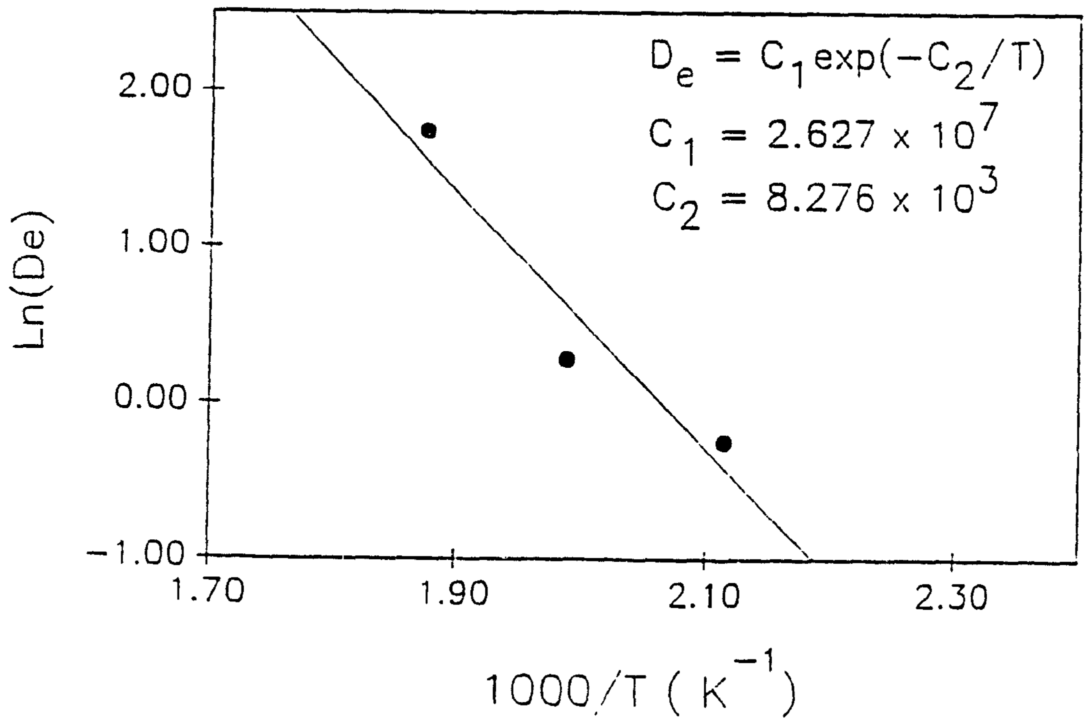

Figure 5.7: Relationship between D_e and inverse temperature (T^{-1}).

Table 5.4: TM effective mode index measurements before and after annealing (Note that $T = 200^oC$ for all initial PE waveguides given in Table 5.4-5.6).

T_a (^oC)	Sample #	t (min)	t_a (hr)	TM0	TM1	TM2	TM3	TM4	TM5
200	16	31	0	2.2397					
			0.5	2.2562					
			1.0	2.2611					
			2.0	2.2645					
			4.0	2.2650					
			8.0	2.2648					
			12.0	2.2647					
			16.0	2.2641					
200	17	220	0	2.3201	2.2821	2.2296			
			0.5	2.3141	2.2846	2.2377			
			1.0	2.3118	2.2849	2.2382			
			2.0	2.3112	2.2849	2.2410			
			4.0	2.3117	2.2896	2.2526	2.2052		
			8.0	2.3114	2.2909	2.2582	2.2145		
			12.0	2.3108	2.2912	2.2609	2.2187		
			16.0	2.3096	2.2904	2.2594	2.2179		

Table 5.5: TM effective mode index measurements before and after annealing.

T_a (^oC)	Sample #	t (min)	t_a (hr)	TM0	TM1	TM2	TM3	TM4	TM5
300	18	21	0	2.2028					
			0.5	2.2293					
			1.0	2.2249					
			2.0	2.2238					
			4.0	2.2161					
			6.0	2.2121					
			8.0	2.2104					
			12.0	2.2086					
			16.0	2.2082					
300	19	30	0	2.2311					
			0.5	2.2488					
			1.0	2.2454					
			2.0	2.2334					
			4.0	2.2264	2.2016				
			6.0	2.2182	2.2026				
			8.0	2.2169	2.2037				
			12.0	2.2145	2.2039				
			16.0	2.2123	2.2042				
300	20	205	0	2.3152	2.2643				
			0.5	2.2963	2.2772	2.2455	2.2078		
			1.0	2.2934	2.2745	2.2430	2.2083		
			2.0	2.2911	2.2711	2.2397	2.2084		
			4.0	2.2880	2.2659	2.2355	2.2095		
			6.0	2.2847	2.2619	2.2351	2.2108		
			8.0	2.2809	2.2576	2.2302	2.2100		
			12.0	2.2761	2.2540	2.2289	2.2108		

Table 5.6: TM effective mode index measurements before and after annealing.

T_a ($^\circ C$)	Sample #	t (min)	t_a (hr)	TM0	TM1	TM2	TM3	TM4	TM5
400	21	20	0	—					
			0.25	2.2092					
			0.5	2.2098					
			1.0	2.2065					
			1.5	2.2062					
			2.0	2.2039					
	22	30	0	2.2344					
			0.5	2.2145	2.2045				
			1.0	2.2106	2.2047				
			2.0	2.2064	2.2039				
400	23	120	0	2.3068	2.2422				
			0.25	2.2776	2.2485	2.2214	2.2031		
			0.5	2.2723	2.2452	2.2211	2.2051		
			1.0	2.2630	2.2381	2.2188	2.2067		
			1.5	2.2481	2.2312	2.2178	2.2083	2.2028	
			2.0	2.2352	2.2263	2.2161	2.2091	2.2045	
400	24	210	0	2.3176	2.2709	2.2064			
			0.5	2.2800	2.2575	2.2344	2.2174	2.2055	
			1.0	2.2653	2.2465	2.2304	2.2168	2.2077	
			2.0	2.2423	2.2319	2.2229	2.2151	2.2092	2.2050

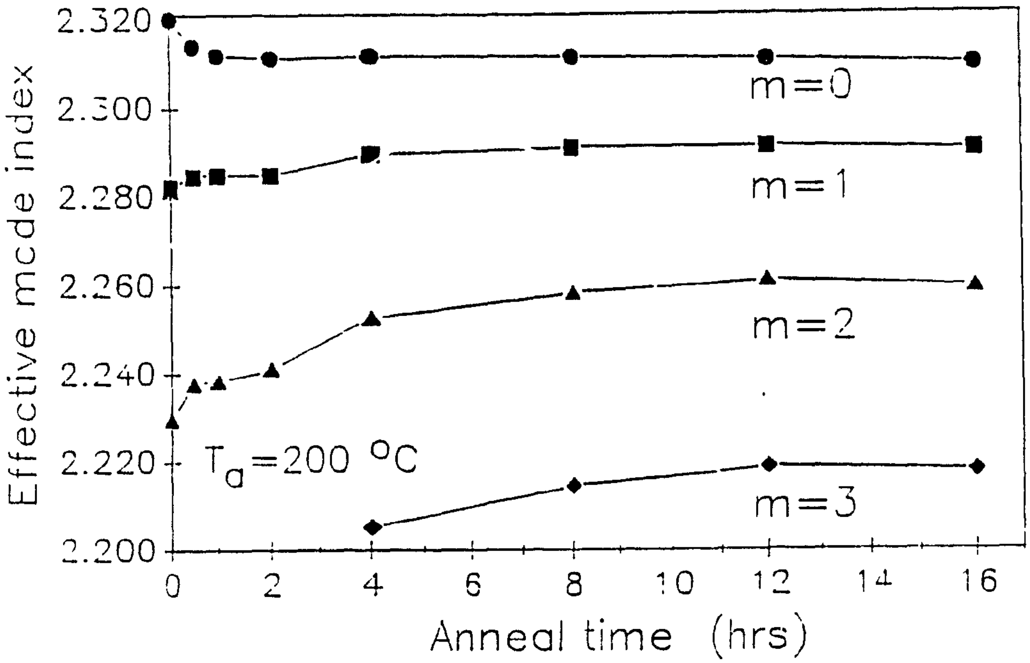

Figure 5.8: Evolution of effective mode indices with anneal time (sample # 17).

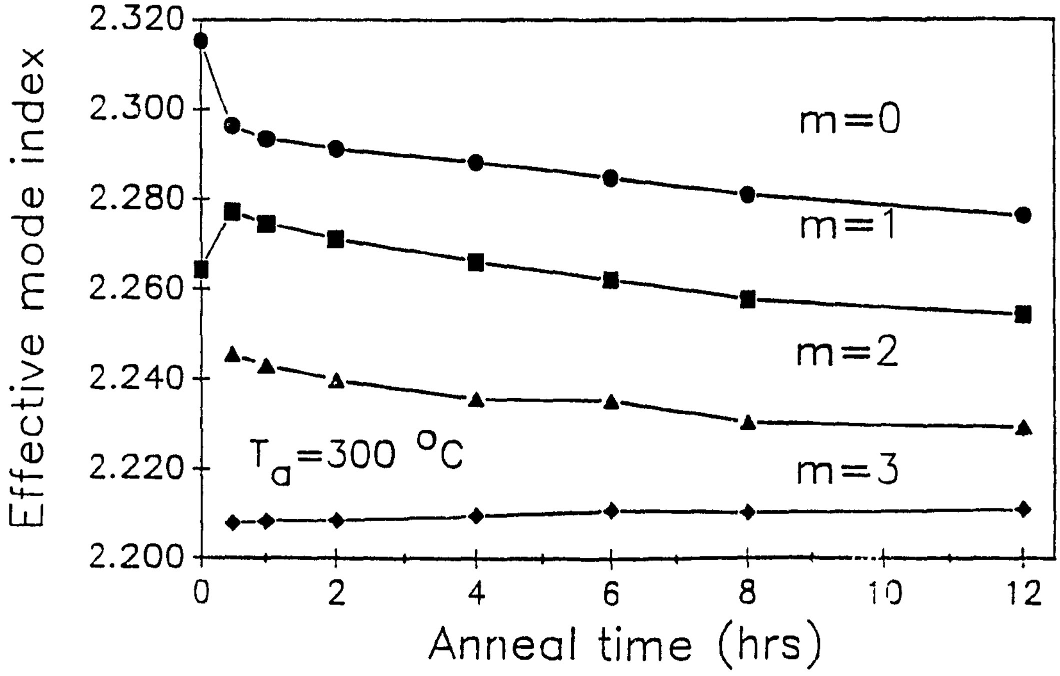

Figure 5.9: Evolution of effective mode indices with anneal time (sample # 20).

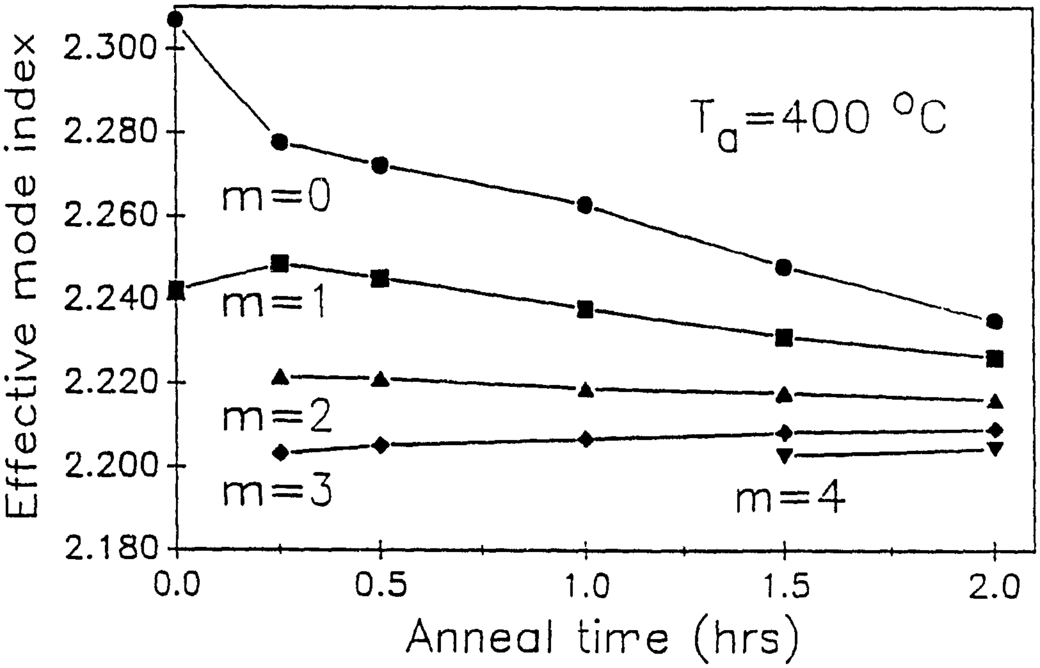

Figure 5.10: Evolution of effective mode indices with anneal time (sample # 23).

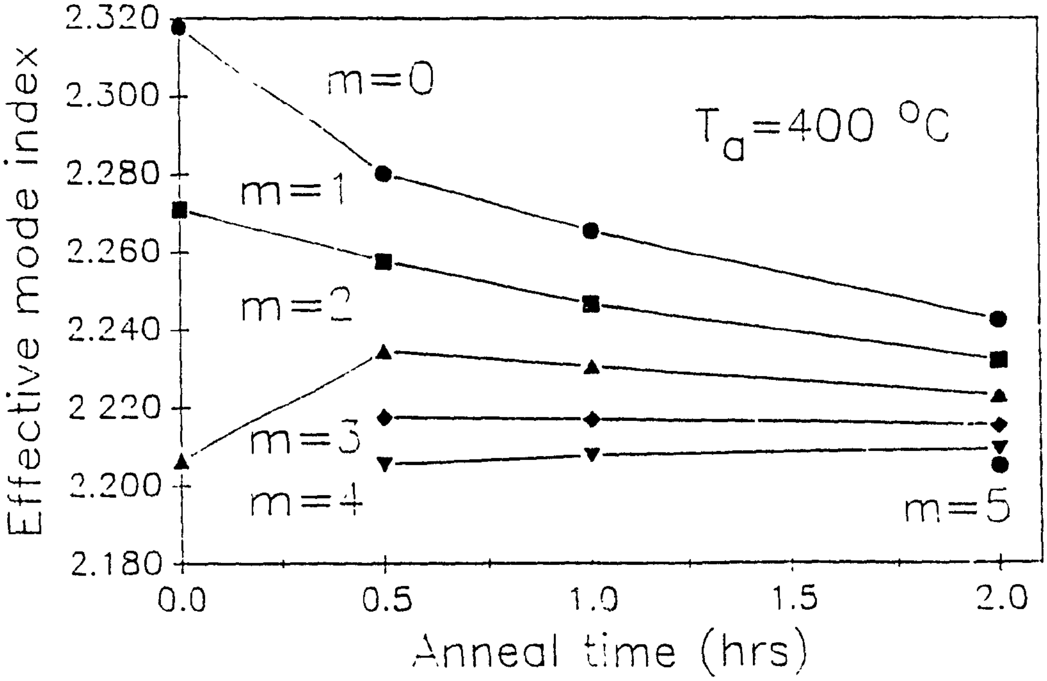

Figure 5.11: Evolution of effective mode indices with anneal time (sample # 24).

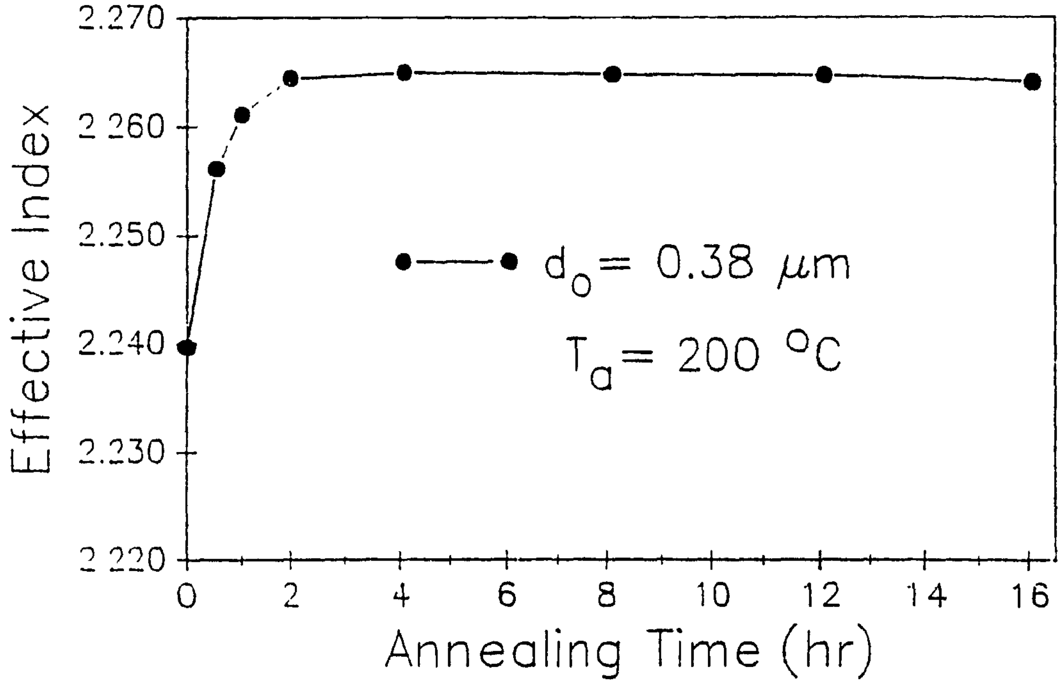

Figure 5.12: Evolution of effective mode indices with anneal time (sample # 16). Waveguide remained single mode for entire anneal period.

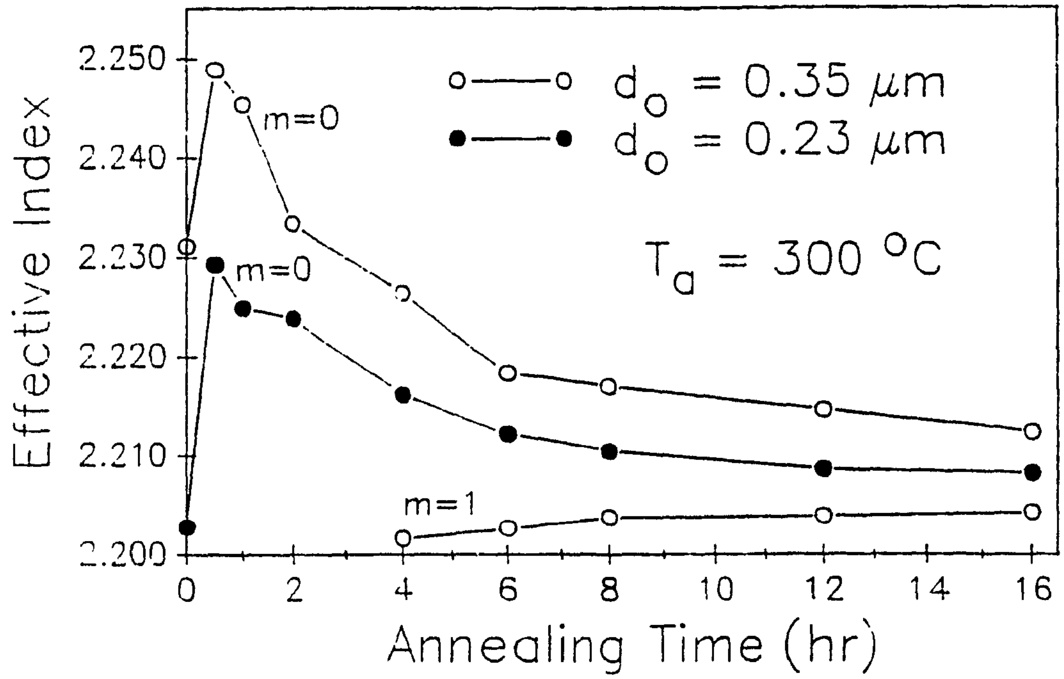

Figure 5.13: Evolution of effective mode indices with anneal time (samples # 18 and # 19). Reducing d_o to 0.23μm (just above cutoff) extends single mode behaviour.

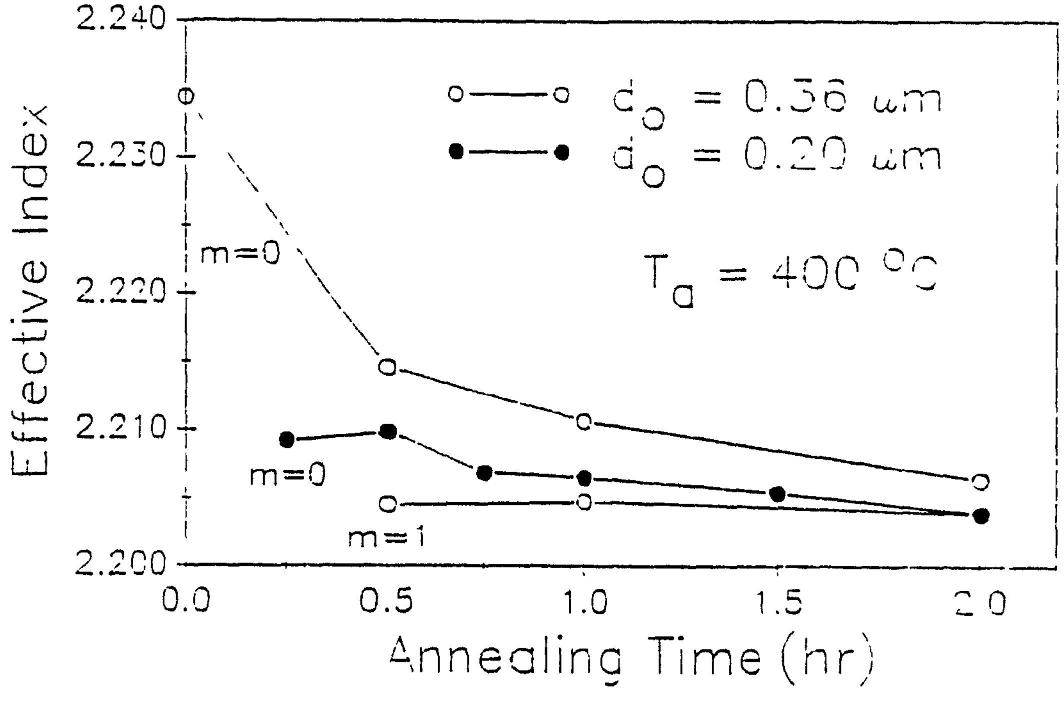

Figure 5.14: Evolution of effective mode indices with anneal time (samples # 21 and # 22). To extend single mode behaviour. the required $d_o = 0.20 \mu m$ resulted in no modes being supported initially.

Table 5.7: Single mode propagation criteria for APE waveguides.

T_a (°C)	d_o (μm)	initial N_e	t_a range (hrs)
200	0.38	2.2397	16
300	0.23	2.2028	16
400	0.20	—	2

Table 5.8: Computed anneal waveguide parameters for a generalized Gaussian index profile.

T_a ($^\circ C$)	Sample #	t_a (hrs)	d (μm)	Δn_s	a_{opt}
200	17	0	1.3195	0.1327	9.36
		0.5	1.4398	0.1221	20.00
		1.0	1.4535	0.1189	40.00
		2.0	1.4967	0.1180	30.00
		4.0	1.6553	0.1180	22.10
		8.0	1.7551	0.1170	21.10
		12.0	1.8054	0.1157	24.00
		16.0	1.8071	0.1146	23.00
300	20	0	1.0860	0.1314	11.00
		0.5	1.8260	0.1025	14.40
		1.0	1.8600	0.1005	10.64
		2.0	1.8743	0.0999	7.25
		4.0	1.9001	0.0982	5.00
		6.0	1.9592	0.0967	4.10
		8.0	1.9420	0.0955	3.14
		12.0	2.0319	0.0903	2.90
400	23	0	0.8600	0.1314	10.21
		0.25	1.6673	0.0998	2.42
		0.5	1.7351	0.0952	2.07
		1.0	1.7634	0.0906	1.55
		1.5	1.2695	0.0688	1.42
		2.0	3.3790	0.0462	1.66
400	24	0	1.1444	0.1325	11.09
		0.5	2.1322	0.1300	2.02
		1.0	2.4817	0.0833	1.74
		2.0	3.6779	0.0537	1.55

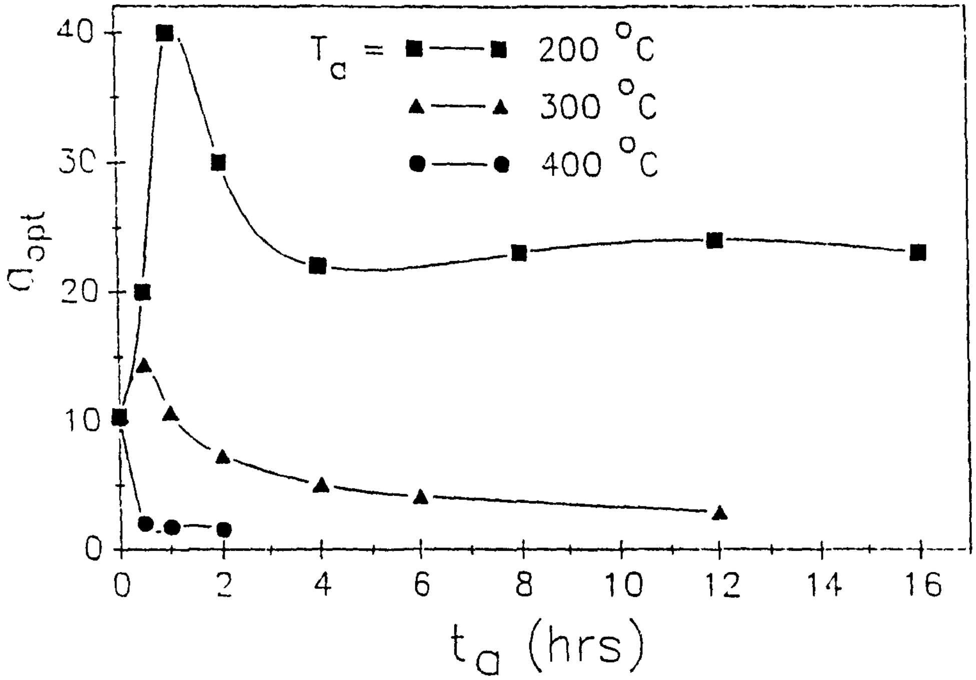

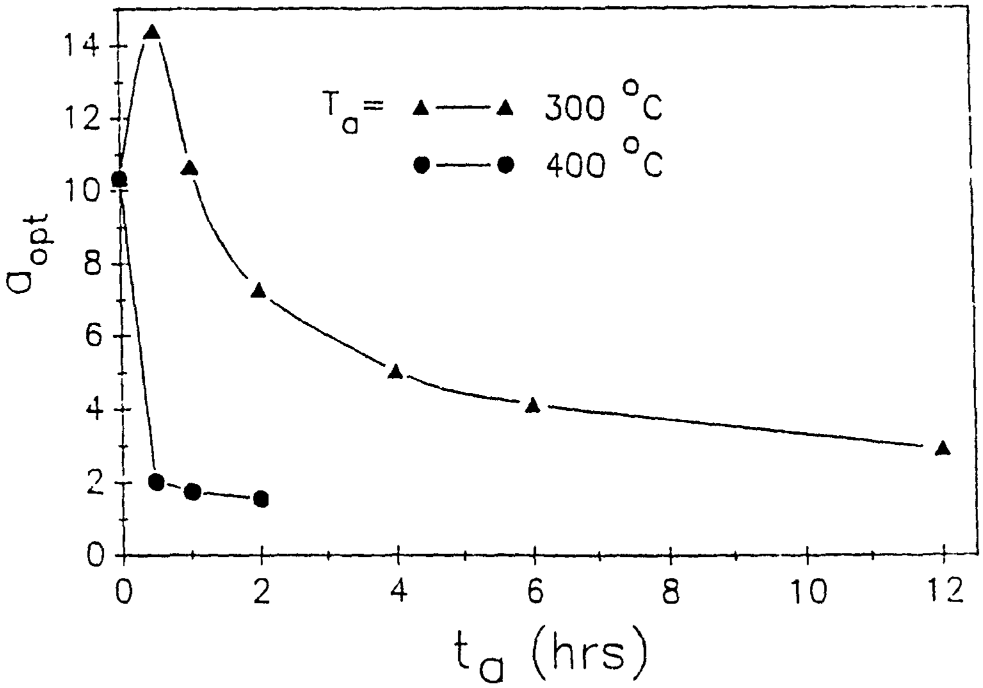

Figure 5.15: (top) Effect of the anneal temperature and time on the shape of the profile (a_{opt}). (bottom) Expanded view of the above figure focusing on $T_a = 300°C$ and $400°C$.

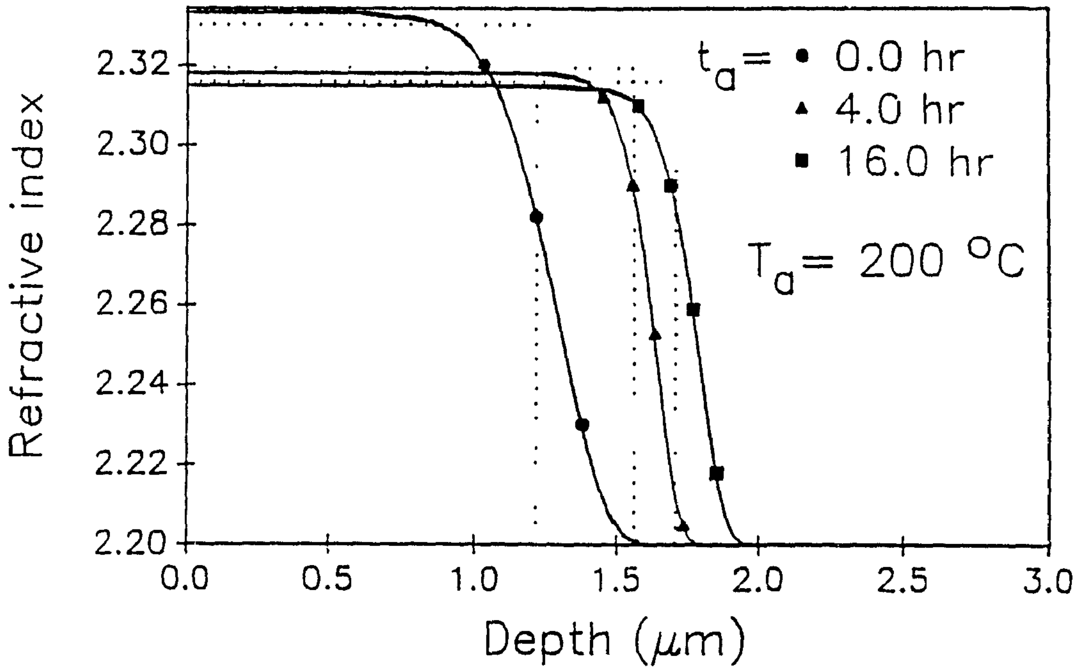

Figure 5.16: Evolution of refractive index profile with anneal time (sample # 17). Solid and dotted curves refer to optimized and step approximation results, respectively.

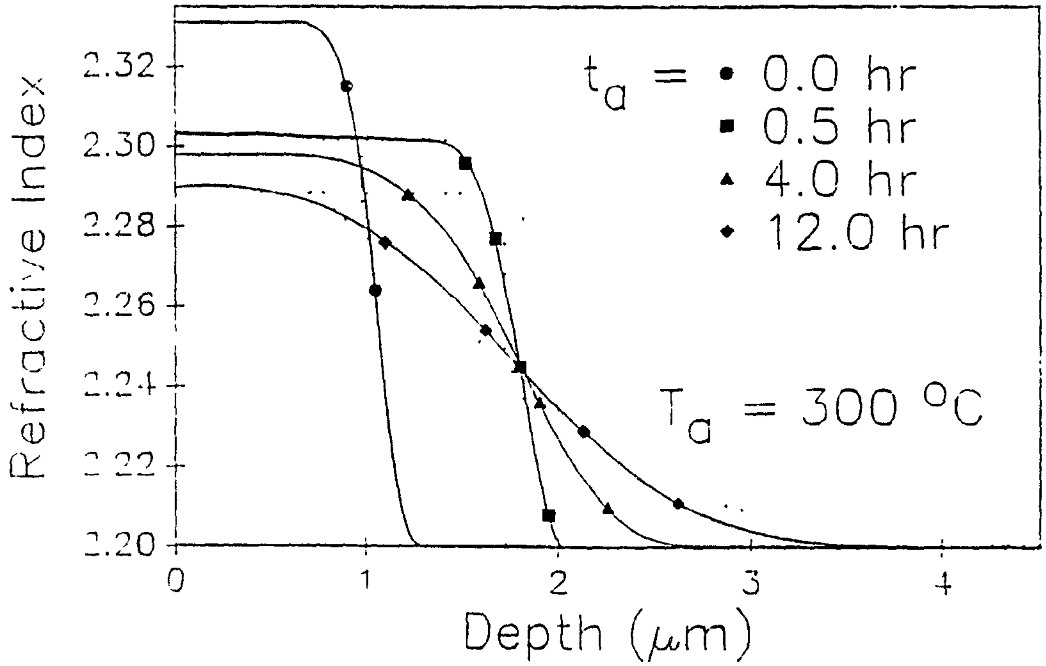

Figure 5.17: Evolution of refractive index profile with anneal time (sample # 20). Solid and dotted curves refer to optimized and step/Gaussian approximation results, respectively.

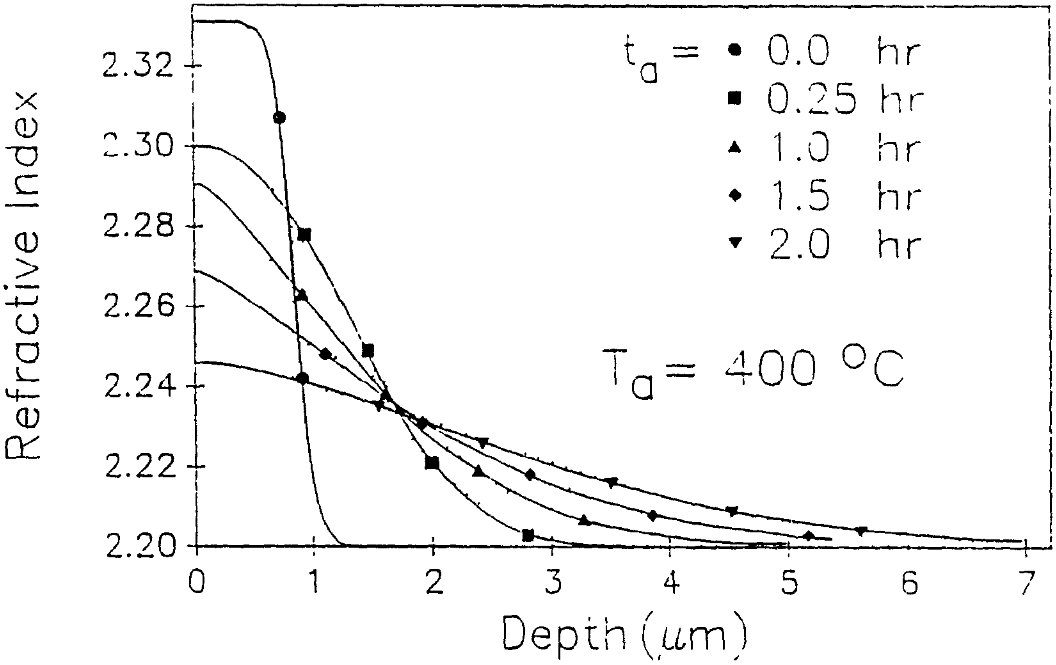

Figure 5.18: Evolution of refractive index profile with anneal time (sample # 23). Solid and dotted curves refer to optimized and Gaussian approximation results, respectively.

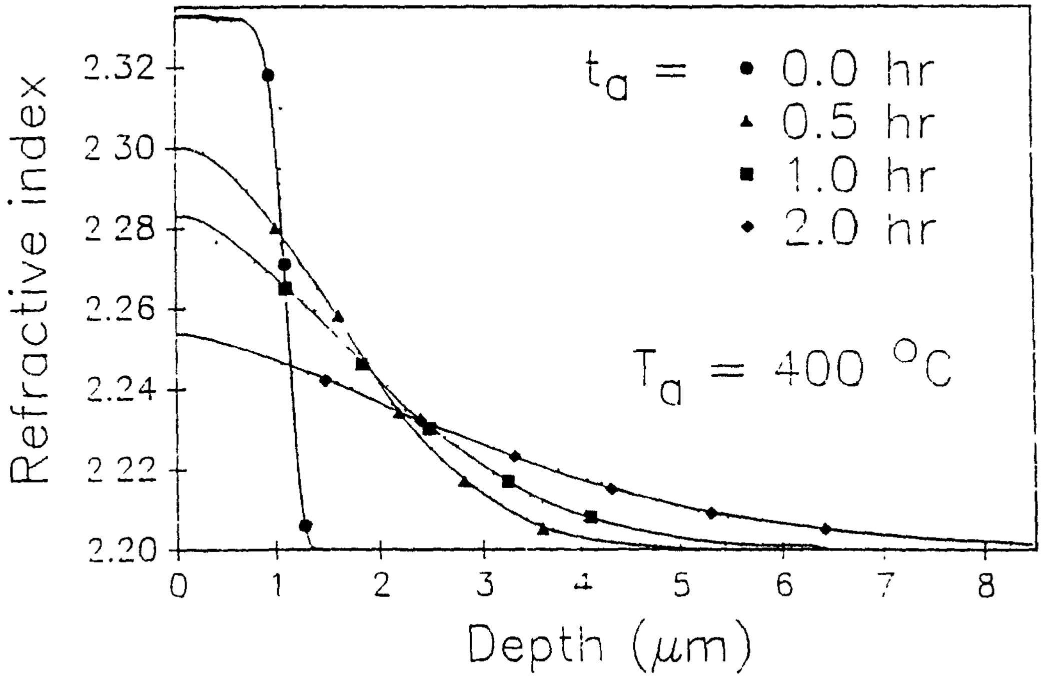

Figure 5.19: Evolution of refractive index profile with anneal time (sample # 24). Solid and dotted curves refer to optimized and Gaussian approximation results, respectively.

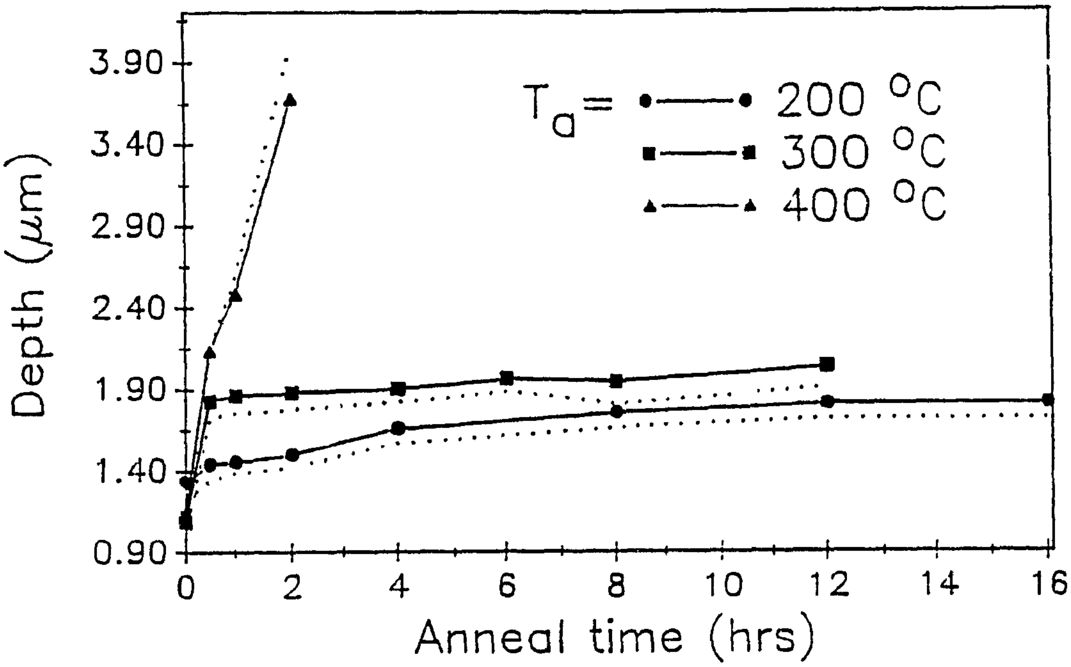

Figure 5.20: Effect of anneal temperature and time on waveguide depth.

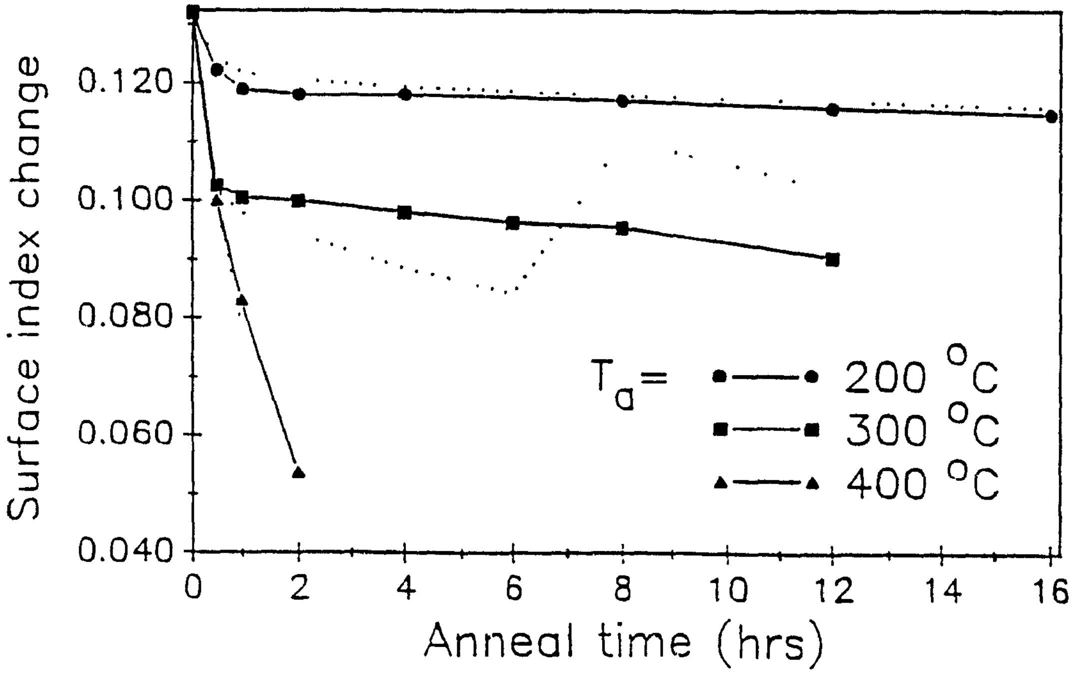

Figure 5.21: Effect of anneal temperature and time on waveguide surface index change.

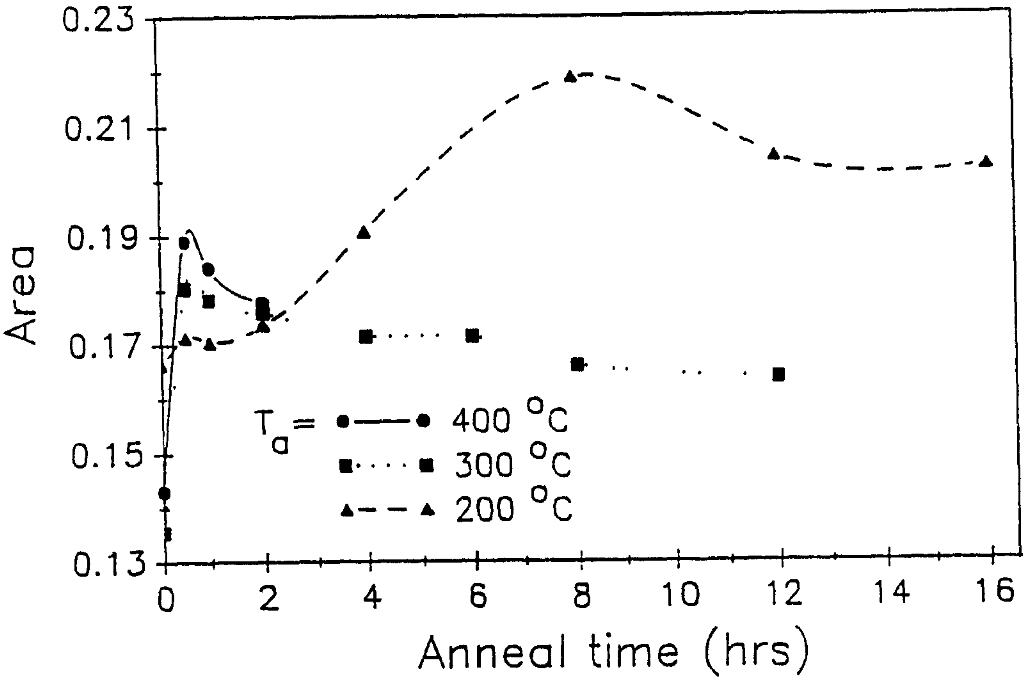

Figure 5.22: Effect of anneal temperature and time on the area under the refractive index versus depth curves.

Table 5.9: Least squares fitting parameters of evolving depth and surface index changes.

T_a (°C)	Sample #	b $(hrs)^{-c}$	c	p $(hrs)^{-q}$	q
300	20	0.7031	0.0754	0.2325	0.1033
400	23	1.4704	0.7794	0.4081	0.5852
400	24	1.2884	0.7577	0.3749	0.6574

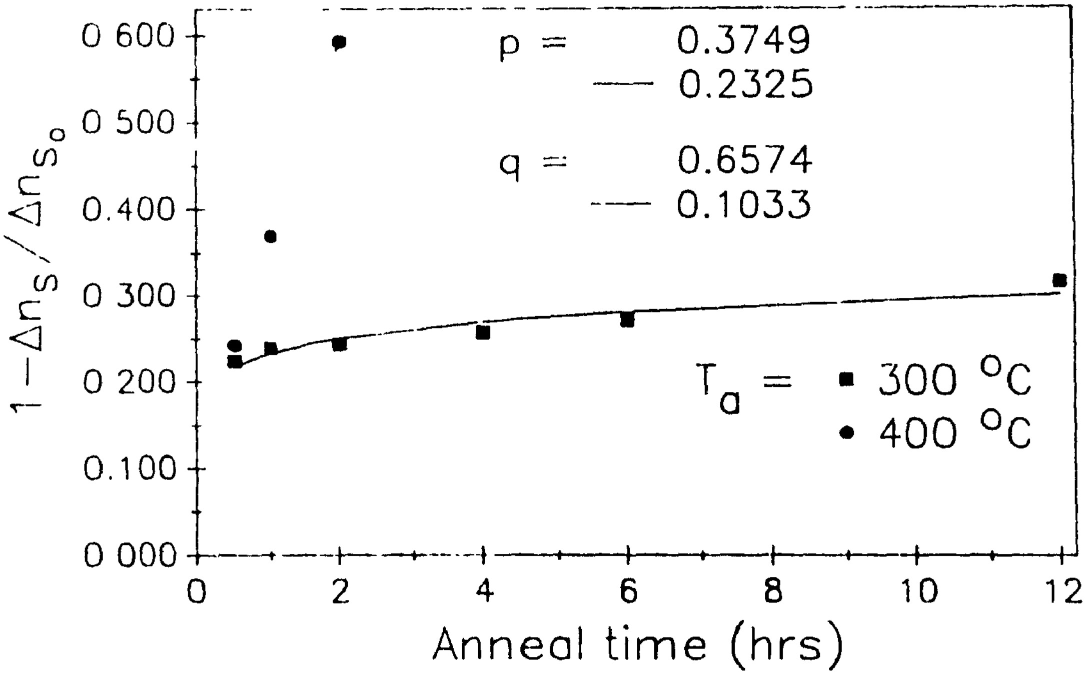

Figure 5.23: Least squares nonlinear regression fit to evolving surface index changes. Here, Δn_{s_o} is the initial ($t_a = 0$) surface index change.

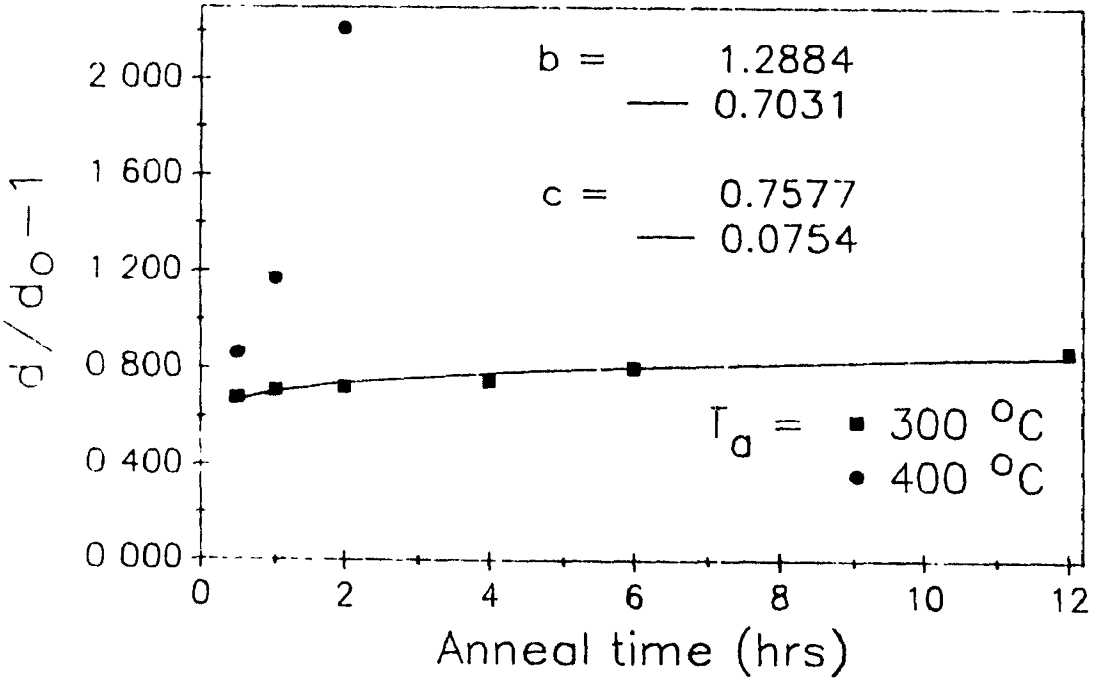

Figure 5.24: Least squares nonlinear regression fit to evolving depth changes. Here, d_o is the initial depth.

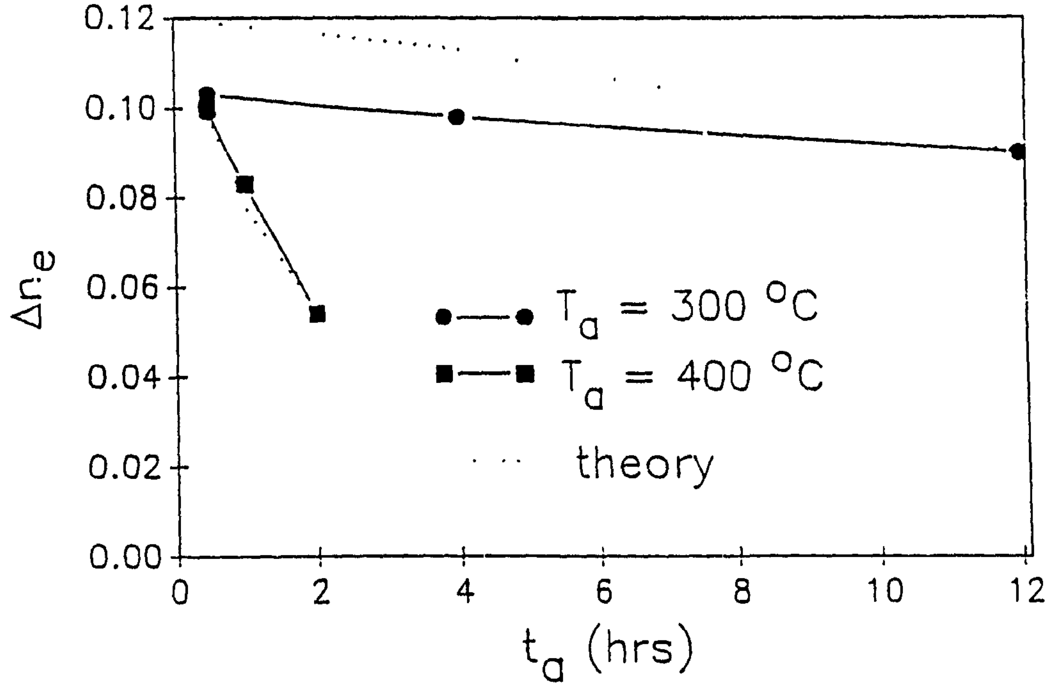

Figure 5.25: Comparison of simple diffusion theory with experiment.

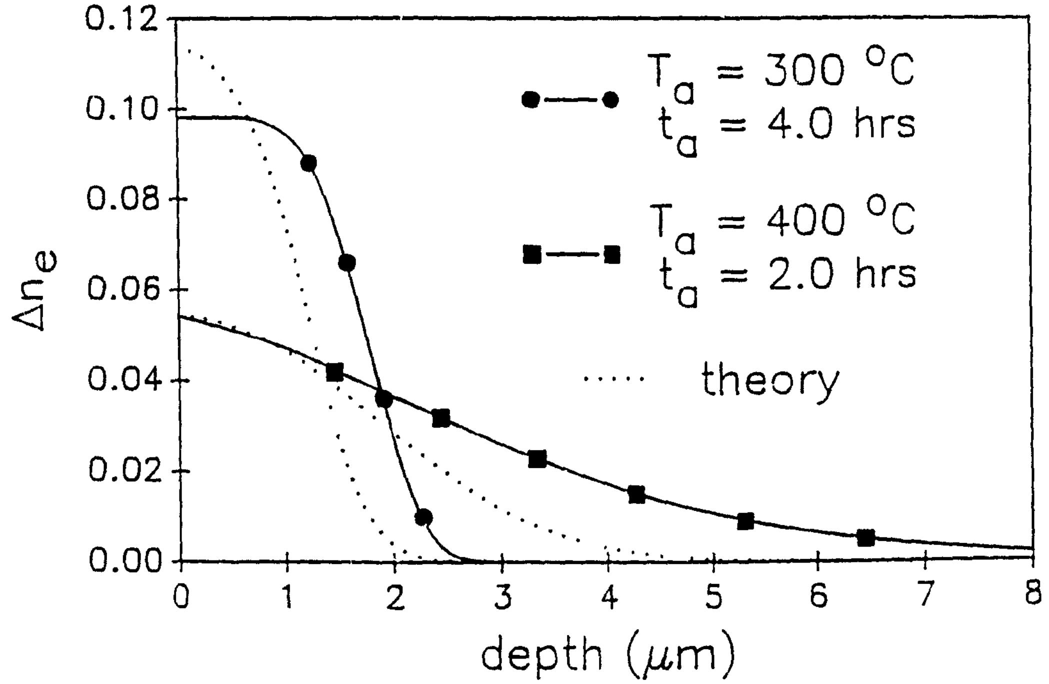

Figure 5.26: Comparison of simple diffusion theory with experiment.

Table 5.10: Propagation loss measurements.

Sample #	T_a (^oC)	t_a (hrs)	α_{dB} $\frac{dB}{cm}$
11	—	—	6.3
19	300	16	3.8

Chapter 6

Discussion and Conclusion

The goal of this thesis research was to fabricate and characterize planar proton-exchanged (PE) and annealed proton-exchanged (APE) optical waveguides in z-cut $LiNbO_3$. The objective of this characterization was to accurately model and correlate the waveguide refractive index profiles with the corresponding fabrication conditions. In addition, the effectiveness as design tools of the various diffusion models which have been proposed to describe the proton-exchange and annealing processes was investigated in detail. Such information will help in the design and optimization of PE $LiNbO_3$ devices for a variety of Integrated Optics applications.

The PE waveguides were fabricated using a very simple and convenient surface coating technique with pyrophosphoric acid as the proton source. The acid was observed to degrade for high exchange temperatures and long exchange times, certainly an important consideration as far as the quality of the fabrication procedure is concerned. A standard prism coupler was used to measure the effective mode indices. The use of a Fermi function was found to accurately model the refractive index profile resulting in a better agreement between these measured effective mode indices and the computed dispersion curves compared to the conventional step-index profile. Moreover, the extraordinary surface index increases of 0.131-0.132 which are consistent with what has been recently observed [54,55,77] (0.131-0.134) are significantly lower than the value of 0.145 reported elsewhere [24,116]. Nevertheless, these values are still slightly larger than the corresponding values reported [21,22] for PE in benzoic acid (0.126). An empirical correlation of the waveguide properties with the fabrication conditions was found to verify the $\sqrt{t}$ dependence of the optical depth (d) and the Arrhenius behaviour of the effective diffusion coefficient (D_e). Although the calculated Arrhenius coefficients (C_1, C_2) differ considerably from those reported by Yamamoto et al. [26], they show good agreement with some recent observations [77,121,122].

A rigorous treatment of the effect of the uniaxial anisotropy in PE waveguides on the dispersion curves showed that differences between the isotropic and anisotropic step-index models become significant for only very multimoded ($m \gg 4$) waveguides. Experimental data were found to verify this showing that discrepancies in the computed waveguide parameters were within experimental error. Consequently, for single mode design purposes, this effect can be neglected.

Parallel to the above waveguide characterization, a detailed investigation of the modeling of the PE diffusion process was carried out revealing that the standard nonlinear diffusion model based on the well established ion-exchange equations with the assumption of a constant self-diffusion coefficient can not adequately explain the hydrogen step and noncomplimentary lithium depletion concentration profiles that have been reported in the literature. These findings suggest that the PE process is not characterized by simple diffusion mechanisms nor a one for one ion-exchange. Although it was not attempted, the use of concentration dependent self-diffusion coefficients has recently been shown [56] to give better agreement between theory and experiment.

The annealing process which is a necessary step in the fabrication of high quality waveguides was studied in detail by considering a very wide range of fabrication conditions. Contrary to previous studies involving benzoic acid [19,125], the surface of all samples annealed at $T_a = 400^o C$ for $t_a > 2hrs$ became clouded indicating that substantial surface damage had occurred. This surface damage has been previously observed [62,63] to occur for $T_a \geq 500^o C$ only. The annealing of PE waveguides was found to result in an increase in the waveguide depth, a decrease in the surface index, and an increase in the number of propagating modes. By appropriately chosing the initial PE depth (d_o), the region of single mode behaviour could be extended. It was found that d_o had to be decreased as the anneal temperature increased. These results show that, in addition to tailoring the effective mode index, annealing can be used to relax the tight fabrication tolerances associated with PE single mode channel waveguides.

A generalized Gaussian function was used to accurately model the APE waveguide refractive index profile. Most of the changes in the waveguide parameters occurred approximately within the first 2 hours of annealing with greater changes occurring for higher anneal temperatures. The computed changes in the depth and surface index were $0.018/0.49\mu m$, $0.041/0.95\mu m$, and $0.079/2.53\mu m$ for $T_a = 200^o C$ $(t_a = 16hrs)$, $T_a = 300^o C$ $(t_a = 12hrs)$, $T_a = 400^o C$ $(t_a = 2hrs)$, respectively, showing that considerable flexibility exists in the tailoring of the waveguide parameters. The shape of the annealed profile was also found to depend on the anneal time and temperature. Approximately Gaussian profiles could only be obtained when higher anneal temperatures $(T_a \geq 300^o C)$ were used. The tremendous flexibility offered by the generalized Gaussian function was demonstrated by its ability to not only accurately quantify the profile shape transition regions (eg. step to Gaussian) but, also, to overcome the restrictions associated with the use of IWKB methods. Moreover, the relatively simple analytic form of this function resulted in a correspondingly simple expression for the area under the index versus depth curves. This area was found to vary with anneal time and temperature thus verifying the nonlinear dependence of the extraordinary refractive index on the hydrogen concentration.

An empirical correlation of the index and depth changes with the fabrication conditions using a general power law revealed that the physical mechanisms associated with intermediate ($T_a = 300^oC$) and high temperature ($T_a = 400^oC$) annealing are different and not governed by simple diffusion processes as has been previously assumed [56]. This result was further supported by the fact that the theoretical index profiles (calculated assuming simple diffusion) did not agree with their measured counterparts. It is possible that a better agreement may be obtained with a nonlinear diffusion model; this, however, was not investigated.

It is clear from the above discussion that the focus of this characterization has been on the modeling of PE/APE refractive index profiles. The techniques and models presented here are very general and flexible in that they can be used to study a wide range of waveguide fabrication technologies. In particular, PE $LiTaO_3$ waveguides have been given increasing attention in the last few years due to their better power handling capability compared to PE $LiNbO_3$ waveguides.

Aside from the modeling of the PE/APE processes, a detailed study of waveguide loss would complement this work and, hence, improve the optimization of PE devices. Other topics that still need to be addressed include the fabrication and characterization of buried waveguides which are important for optimal fiber coupling. Although previous work [53] has involved exploiting the negative PE ordinary index change and using an anneal TiPE process, the recent work of Gan'shin et al. [130] suggests that such structures can be fabricated by PE followed by a backdiffusion in a $LiNO_3$ melt. Another recent development is the use of a CO_2 laser to anneal localized regions of an integrated optical circuit thereby allowing for the fine tuning of the waveguide parameters. These different areas of PE characterization should provide for stimulating and interesting research for the future.

Appendix A

Prism Coupling Involving Anisotropic Media

To derive:

$$N_e = n_p \sin\left\{\alpha_p + \sin^{-1}\left(\frac{\sin\theta_i}{n_p}\right)\right\} \tag{A.1}$$

where

θ_i = external incident angle

n_p = prism index

α_p = base angle of the prism

Due to the uniaxial nature of the rutile prism as well as the $LiNbO_3$ substrate and waveguide film, one must be careful to distinguish between the *ordinary* and *extraordinary* indices of refraction. For the coordinate system chosen (see Fig. A.1), the principal index *tensors* for the film, substrate, and prism are as follows:

$$\tilde{n_f} = \begin{bmatrix} n_{fe} & 0 & 0 \\ 0 & n_{fo} & 0 \\ 0 & 0 & n_{fo} \end{bmatrix} \tag{A.2}$$

$$\tilde{n_s} = \begin{bmatrix} n_{se} & 0 & 0 \\ 0 & n_{so} & 0 \\ 0 & 0 & n_{so} \end{bmatrix} \tag{A.3}$$

$$\tilde{n_p} = \begin{bmatrix} n_{po} & 0 & 0 \\ 0 & n_{pe} & 0 \\ 0 & 0 & n_{po} \end{bmatrix} \tag{A.4}$$

where '˜' is used to denote a tensor quantity and the subscripts o and e refer to the ordinary and extraordinary index, respectively. Notice that the *optic axis* is in the y direction for the prism and x direction for the film and substrate. For PE waveguides, only TM waves can propagate in z-cut $LiNbO_3$ (i.e. the extraordinary index increases while the ordinary index actually decreases). Hence, the derivation below will concentrate exclusively on TM modes. Now, taking $n_a = 1$ (air), one can readily apply Snell's Law (i.e. phase-matching) at the prism-air interface to obtain:

$$n_{po} \sin\theta_t = \sin\theta_i \tag{A.5}$$

$$\rightarrow \quad \theta_t = \sin^{-1}\left(\frac{\sin\theta_i}{n_{po}}\right) \tag{A.6}$$

Notice that in applying Snell's Law, the *ordinary* index of the prism must be used because the TM wave is polarized along the x direction. Now, from basic geometry,

$$90 - \theta_t = 90 - \theta + \alpha_p \tag{A.7}$$

$$\rightarrow \quad \theta = \theta_t + \alpha_p \tag{A.8}$$

If one now applies phase-matching at the prism-air-film interface, one obtains:

$$n_{fe} \sin\theta_m = n_{po} \sin\theta \tag{A.9}$$

where m refers to the mode order. Since, by definition, $N_e = n_{fe}\sin\theta_m$, then by substituting Eq. A.6 and Eq. A.8 into Eq. A.9, the desired result is obtained, namely,

$$N_e = n_{po} \sin\left\{\alpha_p + \sin^{-1}\left(\frac{\sin\theta_i}{n_{po}}\right)\right\} \tag{A.10}$$

Hence, in the formula given in Chapter 4, one must keep in mind that $n_p = n_{po}$. Note that a more general treatment of the above phase-matching which takes into account errors due to prism misalignment has been recently reported [131]. This concludes the proof.

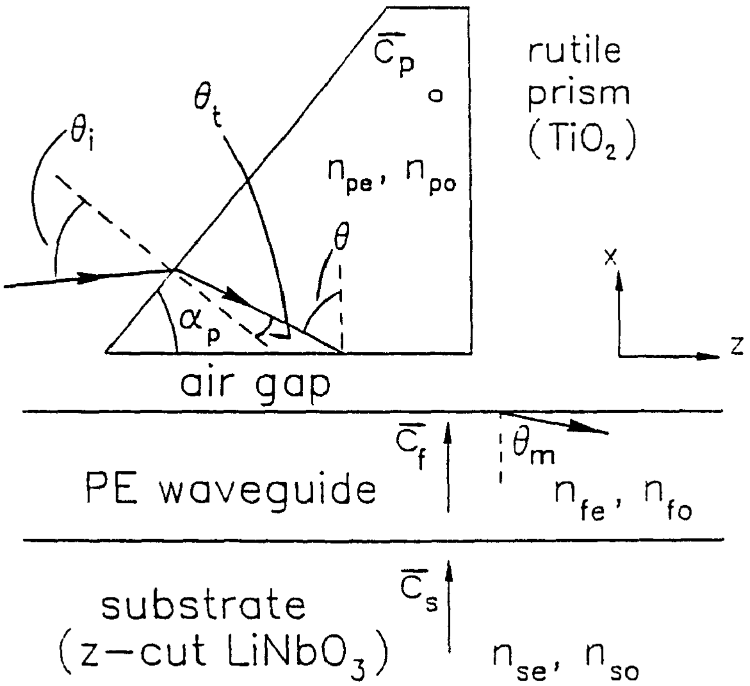

Figure A.1: Coupling to a PE $LiNbO_3$ waveguide using a rutile (TiO_2) prism. The vector, $\vec{c}$, refers to the optic axis direction in each medium.

Bibliography

[1] L.D. Hutcheson, ed., *Integrated Optical Circuits and Components: Design and Applications*, Marcel Dekker, Inc., New York, 1987.

[2] T. Tamir, ed.,*Topics in Applied Physics Volume 7: Integrated Optics*, Springer-Verlag, New York, 1982.

[3] D. Gunter, ed., *Electro-optic and Photorefractive Materials*, Springer-Verlag, New York, 1986.

[4] D.L. Lee, *Electromagnetic Principles of Integrated Optics*, John Wiley & Sons, Inc., New York, 1986.

[5] H. Nishihara, M. Haruna, and T. Suhara, *Optical Integrated Circuits*, McGraw Hill, New York, 1989.

[6] L. Thylen, "Integrated Optics in $LiNbO_3$: Recent Developments in Devices for Telecommunications," J. Lightwave Tech., LT-6, 847 (1988).

[7] R.A. Syms, "Tutorial Review: Advances in channel waveguide lithium niobate integrated optics," Opt. Quantum Elec., 20, 189 (1988).

[8] M.M. Abouelleil and F.J. Leonberger, "Waveguides in Lithium Niobate (review)," J. Am. Ceram. Soc., 72, 1311 (1989).

[9] R.F. Leheny, "Progress in optoelectronic integration (invited paper)," in Technical Digest on Integrated Photonics Research (Hilton Head, SC), Vol. 5, 50 (1990).

[10] A. Yi-Yan, W.K. Chan, T.J. Gmitter, L.T. Florez, J.L. Jackel, E. Yablonovitch, R. Bhat, and J.P. Harbison, "Grafted *GaAs* Detectors on Lithium Niobate and Glass Optical Waveguides," IEEE Photonics Tech. Lett., 1, 379 (1989).

[11] L.M. Walpita, "Organic materials in future integrated opto-electronic circuits (invited paper)," in SPIE OE/FIBERS '89 (Boston, Mass.), Integrated Optics and Optoelectronics, Vol. 1177, 58 (1989).

[12] D. Yevick and T. Fysik, "Numerical Methods in Integrated Optics (invited paper)," in SPIE OE/FIBERS '89 (Boston, Mass), Integrated Optics and Optoelectronics, Vol. 1177, 186 (1989).

[13] T.P. Young, "Computer-aided design of integrated optics: closing the synthesis loop (plenary paper)," in Technical Digest of Integrated Photonics Conference (Hilton Head, SC), Vol. 5, 3 (1990).

[14] M.A. Sekerka-Bajbus and G.L. Yip, "An improved $Ti : LiNbO_3$ line modulator by ion-beam milling," in Integrated Optical Circuit Engineering VI, SPIE, 993, 102 (1988).

[15] R.V. Johnson, "Recent Developments in Integrated Optics at Crystal Technology," in SPIE OE/FIBERS '89 (Boston, Mass), Integrated Optics and Optoelectronics, Vol. 1177, 327 (1989).

[16] G.J. Sellers and S. Sriram, "Manufacturing of lithium niobate integrated optic devices," Optics News, Feb., 29 (1988).

[17] M.F. Grant, A. Donaldson, D.R. Gibson, and M. Wale, "Recent progress in lithium niobate integrated optics technology under a collaborative Joint Opto-Electronics Research Scheme (JOERS) programme," Opt. Eng., 27, 002 (1988).

[18] S. Fouchet, A. Carenco, C. Daguet, R. Guglielmi, and L. Riviere, "Wavelength Dispersion of Ti Induced Refractive Index Change in $LiNbO_3$ as a Function

of Diffusion Parameters," J. Lightwave Tech., LT-5, 700 (1987).

[19] K.K. Wong, "Integrated optical waveguides and devices fabricated by proton-exchange: a review," in Integrated Optical Circuit Engineering VI, SPIE, 993, 13 (1988).

[20] M.M. Howerton, P.R. Skeath, A.S. Greenblatt, and W.K. Burns, "Experimental Determination of Refractive Index Dependence on Hydrogen Concentration in Proton Exchanged $LiNbO_3$," in Technical Digest on Integrated Photonics Research (Hilton Head, S.C.), Vol. 5, 141 (1990).

[21] J. Jackel, C.E. Rice, and J.J. Veselka, "Proton-exchange for high index waveguides in $LiNbO_3$," Appl. Phys. Lett., 41, 607 (1982).

[22] D.F. Clark, A.C.G. Nutt, K.K. Wong, P.J.R. Laybourn, and R.M. De La Rue, "Characterization of proton-exchange slab optical waveguides in z-cut $LiNbO_3$," J. Appl. Phys., 54, 6218 (1983).

[23] K.K. Wong, A.C.G. Nutt, D.F. Clark, P.J.R. Laybourn, and R.M. De La Rue, "Characterization of proton-exchange slab optical waveguides in x-cut $LiNbO_3$," IEE Proc. Part J, 133, 113 (1986).

[24] K. Yamamoto and T. Taniuchi, "Proton-exchanged $LiNbO_3$ waveguides by new protonic source," First Optoelectronic Conference (OEC '86, Tokyo, Japan) Post-Deadline Papers Technical Digest, Paper B11-4, 16 (1986).

[25] K. Yamamoto and T. Taniuchi, "New Proton-Exchange Technique for $LiNbO_3$ fabrication," in Technical Digest, Sixth International Conference on Integrated Optics and Optical Fiber Communication Conference (Reno, Nevada), paper TUH2 (1987).

[26] K. Yamamoto and T. Taniuchi, in Paper of Technical Group of Optical and Quantum Electronics (The Institute of Electronics and Communication Engi-

neers of Japan), paper (in Japanese) OQE86-72 (1986).

[27] J. Baumert and J.A. Hoffnagle, "Numerical Method for the Calculation of Mode Fields and Propagation Constants in Optical Waveguides," J. Lightwave Tech., LT-4, 1626 (1986).

[28] J. Jackel, C.E. Rice, and J.J. Veselka, "Composition control in proton-exchanged $LiNbO_3$," Elec. Lett., 19, 387 (1983).

[29] K.K. Wong, "An experimental study of dilute melt proton-exchanged waveguides in x and z-cut lithium niobate," GEC J. Res., 3, 243 (1985).

[30] J.J. Veselka and G.A. Bogert, "Low insertion loss channel waveguides in $LiNbO_3$ fabricated by proton exchange," Elec. Lett., 23, 172 (1987).

[31] P.G. Suchoski, T. Findakly, and F.J. Leonberger, "Low loss proton exchanged $LiNbO_3$ waveguides with no electro-optic degradation," Tech. Digest of Top. Meeting on Integrated and Guided Wave Optics (IGWO '88), Santa Fe, New Mexico, 88 (1988).

[32] P.G. Suchoski, T. Findakly, and F.J. Leonberger, "Stable low loss proton exchanged $LiNbO_3$ waveguides with low electro-optic degradation," Opt. Lett., 13, 1050 (1988).

[33] A. Loni, R.M. De La Rue, and J.M. Winfield, "Very low-loss proton-exchanged $LiNbO_3$ Wavegides With a Substantially Restored Electrooptic Effect," Topical Meeting on Integrated and Guided-Wave Optics, Santa Fe, New Mexico, MD3-1 (1988).

[34] J. Nikolopoulos and G.L. Yip, "Characterization of proton-exchanged optical waveguides in z-cut $LiNbO_3$ using pyrophosphoric acid," in SPIE OE/FIBERS '89 (Boston, Mass), Integrated Optics and Optoelectronics, Vol. 1177, 24 (1989).

[35] J. Nikolopoulos and G.L. Yip, "Characterization of proton-exchanged and annealed proton-exchanged optical waveguides in z-cut $LiNbO_3$," in SPIE OE/FIBERS '90 (San Jose, Cal.), Fiber netwoking, Telecommunications, and Sensors, Vol. 1374-04 (1990).

[36] J. Nikolopoulos and G.L. Yip, to be submitted.

[37] R.V. Ramaswamy, " Ion-Exchanged Glass Waveguides: A Review," J. Lightwave Tech., LT-6, 984 (1988).

[38] M. Abou-El-Leil and F. Leonberger, "Model for Ion-Exchanged Waveguides in Glass," J. Amer. Ceramic Soc., 71, 497 (1988).

[39] M. Shah, "Optical waveguides in $LiNbO_3$ by ion exchange technique," Appl. Phys. Lett., 26, 652 (1975).

[40] J. Jackel, "High Δn optical waveguides in $LiNbO_3$: Thallium-lithium ion-exchange," Appl. Phys. Lett., 37, 739 (1980).

[41] Y. Chen, W.S. Chang, S.S. Lau, L. Wielunski, and R.L. Holman, "Characterization of $LiNbO_3$ waveguides exchanged in $TlNO_3$ solution," Appl. Phys. Lett., 40, 10 (1982).

[42] J. Jackel and C.E. Rice, "Variation in waveguides fabricated by immersion of $LiNbO_3$ in $AgNO_3$ and $TlNO_3$: The role of hydrogen," Appl. Phys. Lett., 41, 508 (1982).

[43] C.E. Rice and J. Jackel, "$HNbO_3$ and $HTaO_3$: new cubic perovskites prepared from $LiNbO_3$ and $LiTaO_3$ via ion-exchange," J. Solid State Chem., 41, 308 (1982).

[44] M. De Micheli, J. Botineau, S. Neveu, P. Sibillot, D.B. Ostrowsky, and M. Papuchon, "Independent control of index and profiles in proton-exchanged Lithium Niobate guides," Opt. Lett., 8, 114 (1983).

[45] M. De. Micheli, J. Botineau, P. Sibillot, D.B. Ostrowsky, and M. Papuchon, "Fabrication and characterization of titanium indiffused proton-exchanged (TiPE) waveguides in Lithium Niobate," Opt. Comm., 42, 101 (1982).

[46] A. Loni, G. Hay, R.M. De La Rue, and J.M. Winfield, "Proton-Exchanged $LiNbO_3$ Waveguides: The Effects of Post-Exchange Annealing and Buffered Melts as Determined by Infrared Spectroscopy, Optical Waveguide Measurements, and Hydrogen Isotopic Exchange," J. Lightwave Tech., JLT-7, 911 (1989).

[47] T. Findakly, P.G. Suchoski, and F.J. Leonberger, "High quality $LiTaO_3$ integrated optical waveguides and devices fabricated by the annealed proton-exchange technique," Opt. Lett., 13, 797 (1988).

[48] M. Goodwin and C. Stewart, "Proton-exchanged optical waveguides in y-cut Lithium Niobate," Elec. Lett., 19, 223 (1983).

[49] C. Canali, A. Carnera, G. Della Mea, P. Mazzoldi, S.M. Al-Shukri, A.C.G. Nutt, and R.M. De La Rue, "Structural characterisation of proton-exchanged $LiNbO_3$ optical waveguides," J. Appl. Phys., 59, 2643 (1986).

[50] M. Minakata, K. Kumagai, and S. Kawakami, "Lattice constant changes and electro-optic effects in proton-exchanged $LiNbO_3$ optical waveguides," Appl. Phys. Lett., 49, 992 (1986).

[51] A.L. Dawar, S.M. Al-Shukri, R.M. De La Rue, A.C.G. Nutt, and G. Stewart, "Fabrication and characterization of titanium-indiffused proton-exchanged optical waveguides in z-cut $LiNbO_3$," Opt. Comm., 61, 100 (1987).

[52] A.L. Dawar, S.M. Al-Shukri, R.M. De La Rue, A.C.G. Nutt, and G. Stewart, "Fabrication and characterization of titanium-indiffused proton-exchanged optical waveguides in y-cut $LiNbO_3$," Appl. Opt., 25, 1495 (1986).

[53] A.C.G. Nutt, E. Sudo, and K. Nishizawa, "Control of Ti-indiffused $LiNbO_3$ waveguide profile and propagation characteristics by the proton exchange of lithium ions," OFC/IOOC '87, Reno, Nevada, 64 (1987).

[54] N. Goto and G.L. Yip, "Characterization of proton-exchange and annealed $LiNbO_3$ waveguides with pyrophosphoric acid," Appl. Opt., 28, 60 (1989).

[55] N.A. Sanford and J.M. Connors, "Optimization of Cerenkov sum-frequency generation in proton-exchanged $Mg : LiNbO_3$ channel waveguides," J. Appl. Phys., 65, 1429 (1989).

[56] S.T. Vohra, A.R. Mickelson, and S.E. Asher, "Diffusion Characteristics and Waveguiding Properties of Proton Exchanged and Annealed $LiNbO_3$ Channel Waveguides," J. Appl. Phys., 66, 5161 (1989).

[57] A. Loni, R.M. De La Rue, and J.M. Winfield, "Proton-exchanged, Lithium Niobate planar-optical waveguides: chemical and optical properties and room-temperature hydrogen isotopic exchange reactions," J. Appl. Phys., 61, 64 (1987).

[58] S.T. Vohra and A.R. Mickelson, "The effects of finite melt volume on proton exchanged lithium niobate," J. Lightwave Tech., LT-6, 1848 (1988).

[59] W.E. Lee, N.A. Sanford, and A.H. Heuer, "Direct observation of structural phase changes in proton-exchanged $LiNbO_3$ optical waveguides using transmission electron microscopy," J. Appl. Phys., 59, 2629 (1986).

[60] Private communications with Dr. I. Shih (McGill University, Dept. Elec. Eng.).

[61] J. Jackel and C.E. Rice, "Short and long term index instability in proton exchanged lithium niobate waveguides," in Processing of Guided Wave Optoelectronic Materials, R.L. Holman, D.M. Smyth Eds., Proc. SPIE, 460, 43 (1984).

[62] V.A. Gan'shin, Y.N. Korishko, and V.Z. Petrova, "Fabrication of $H : LiNbO_3$ optical waveguides," Sov. Phys. Tech. Phys., 30, 1313 (1985).

[63] A. Yi-Yan, "Index instabilities in proton-exchanged $LiNbO_3$ waveguides," Appl. Phys. Lett., 42, 633 (1983).

[64] C.E. Rice, J. Jackel, and W.L. Brown, "Measurement of the deuterium concentration profile in a deuterium exchanged $LiNbO_3$ crystal," J. Appl. Phys., 57, 4437 (1985).

[65] N. Schmidt, K. Beltzer, M. Grabs, S. Kapphan, and F. Klose, "Spatially resolved second-harmonic-generation investigations of proton-induced refractive-index changes in $LiNbO_3$," J. Appl. Phys., 65, 1253 (1989).

[66] C.E. Rice, "The structural properties of $Li_{1-x}H_xNbO_3$," J. Solid State Chem., 64, 188 (1986).

[67] F. Hellfferich and M.S. Plesset, "Ion exchange kinetics, a non-linear diffusion problem," J. Chem. Phys., 28, 418 (1958).

[68] G. Stewart, C. A. Millar, P.J.R. Laybourn, C.D.W. Wilkinson, and R.M. De La Rue, "Planar optical waveguides formed by silver migration in glass," IEEE J. Quant. Elect., QE-13, 192 (1977).

[69] J. Albert and G.L. Yip, "Refractive index profiles of planar waveguides made by ion-exchange in glass," Appl. Opt., 24, 3692 (1985).

[70] C.D.W. Wilkinson and R. Walker, "The diffusion profile of stripe optical waveguides formed by ion exchange," Elec. Lett., 14, 599 (1978).

[71] W.F. Ames, *Nonlinear PDE's in Engineering*, Academic Press, Inc., New York, 1965.

[72] J. Crank, *The Mathematics of Diffusion*, Oxford University Press, London, 1956.

[73] J. Albert, *Characterizations and Design of Planar Optical Waveguides and Directional Couplers by Two-Step $K^+ - Na^+$ Ion-Exchange in Glass, Ph.D. Thesis*, McGill University, 1987.

[74] V.E. Wood, "Diffusion profiles in ion-exchanged waveguides," J. Appl. Phys., 47, 3370 (1976).

[75] G. Bach, Notes from course on *Numerical Analysis* given at McGill University, Montreal, Dept. of Electrical Engineering.

[76] Private communications with A. Mickelson (University of Colorado, Boulder).

[77] A. Loni, R.W. Keys, R.M. De La Rue, M.A. Foad, J.M. Winfield, "Optical characterisation of z-cut proton-exchanged $LiNbO_3$ waveguides fabricated using orthophosphoric and pyrophosphoric acid," IEE Proceedings, 136, Pt. J, 297 (1989).

[78] J. Crank, *The Mathematics of Diffusion*, Oxford University Press, 1975.

[79] V. Neuman, O. Parriaux, and L.M. Walpita, "Double-alkali effect: influence on index profile of ion-exchanged waveguides," Elec. Lett., 15, 704 (1979).

[80] D.E. Day, "Mixed Alkali Glasses - Their Properties and Uses," J. Non-Crystall. Sol., 21, 343 (1976).

[81] L.C. Andrews, *Elementary Partial Differential Equations*, Academic Press, Inc., New York.

[82] A.R. Mitchell, *Computational Methods in Partial Differential Equations*, John Wiley and Sons, Inc., New York, 1969.

[83] P.C. Noutsios, *Characterization of Planar Glass Waveguides by $K^+ - Na^+$ Ion-Exchange*, *Master's Thesis*, McGill University, 1990.

[84] A. Knoesen, T.K. Gaylord, and M.G. Moharam, "Hybrid Guided Modes in Uniaxial Dielectric Planar Waveguides," J. Lightwave Tech., LT-6, 1083 (1988).

[85] W.K. Burns and J. Warner, "Mode dispersion in uniaxial optical waveguides," J. Opt. Soc. Amer., 64, 441 (1974).

[86] V. Ramaswamy, "Propagation in Asymmetrical Anisotropic Film Waveguides," Appl. Opt., 13, 1363 (1974).

[87] D.P. Gia Russo and J.H. Harris, "Wave propagation in anisotropic thin-film optical waveguides," J. Opt. Soc. Amer., 63, 138 (1973).

[88] S. Yamamoto, Y. Koyama, and T. Makimoto, "Normal-mode analysis of anisotropic and gyrotropic thin-film waveguides for integrated optics," J. Appl. Phys., 43, 5090 (1972).

[89] M. Gottlieb, C. Ireland, and J. Ley, *Electro-Optic and Acousto-Optic Scanning and Deflection*, Marcel Dekker, Inc., New York , 1983.

[90] H. Haus, *Waves and Fields in Optoelectronics*, Prentice-Hall, Inc., New Jersey, 1984.

[91] E. Colombini and G.L. Yip, "A Novel Monomolecular Layered Film Anisotropic Optical Waveguide for Integrated Optics," Trans. IECE Jap., E 61, 154 (1978).

[92] G. Zhang and K. Sasaki, "Measuring anisotropic refractive indices and film thicknesses of thin organic crystals using the prism coupling method," Appl. Opt., 27, 1358 (1988).

[93] K. Yamanouchi, T. Kamiya, and K. Shibayama, "New leaky surface waves in anisotropic metal-indiffused optical waveguides," IEEE Trans. Microwave Theory Tech., MTT-26, 298 (1978).

[94] J. Ctyroky and M. Cada, "Generalized WKB Method for the Analysis of Light Propagation in Inhomogeneous Anisotropic Optical Waveguides," IEEE J. Quantum Elec., QE-17, 1064 (1981).

[95] J. Ctyroky, "Light Propagation in Proton-Exchanged $LiNbO_3$ Waveguides," J. Opt. Comm., 5, 16 (1984).

[96] A.N. Kaul, S.I. Hosain, and K. Thyagarajan, "A Simple Numerical Method for Studying the Propagation Characteristics of Single-Mode Graded-Index Planar Optical Waveguides," IEEE Trans. Microwave Theory Tech., MTT-34, 288 (1986).

[97] P. K. Mishra and A. Sharma, "Analysis of Single Mode Inhomogeneous Planar Waveguides," J. Lightwave Tech., LT-4, 204 (1986).

[98] M.J. Adams, *An Introduction to Optical Waveguides*, John Wiley & Sons Ltd., New York, 1981.

[99] G.B. Hocker and W.K. Burns, "Modes in diffused optical waveguides of arbitrary index profile," IEEE J. Quantum Elec., QE-11, 270 (1975).

[100] A. Gedeon, "Comparison between rigorous theory and WKB analysis," Opt. Comm., 12, 329 (1974).

[101] J. Janta and J. Ctyroky, "On the accuracy of WKB analysis of TE and TM modes in planar graded-index waveguides," Opt. Comm., 25, 49 (1978).

[102] R. Srivastava, C. K. Kao, and R. V. Ramaswamy, "WKB Analysis of Planar Surface Waveguides with Truncated Index Profiles," J. Lightwave Tech., LT-5, 1605 (1987).

[103] L. Torner, F. Canal, and J. Hernandez-Marco, "Cutoff behaviour of graded-index slab waveguides," Opt. Quantum Elec., 21, 451 (1989).

[104] A.C. Nutt, "Experimental Observations of Light Propagation in Proton-Exchanged Lithium Niobate Waveguides," J. Opt. Commun., 6, 8 (1985).

[105] N. Goto and G.L. Yip, "A TE-TM Mode Splitter in $LiNbO_3$ by Proton Exchange and Ti Diffusion," J. Lightwave Tech., LT-6, 1567 (1989).

[106] P.C. Noutsios and G.L. Yip, "Shallow Buried Waveguides Made by Purely Thermal Migration of K^+ Ions in Glass," Opt. Lett., 15, 212 (1990).

[107] B.L. Gabriel, *SEM: A User's Manual for Materials Science*, American Society for Metals, Metals Park, Ohio, 1985.

[108] J. Albert and G.L. Yip, "Characterization of Planar Optical Waveguides by K^+-Ion Exchange in Glass," Opt. Lett., 10, 151 (1985).

[109] I.P. Kaminow and L.W. Stulz, "Loss in cleaved Ti-diffused $LiNbO_3$ waveguides," Appl. Phys. Lett., 33, 62 (1978).

[110] H.P. Weber, F.A. Dunn, and W.N. Leibolt, "Loss measurements in thin film optical waveguides," Appl. Opt., 12, 755(1973).

[111] Y. H. Won, P.C. Jaussaud and G.H. Chartier, "Three-prism loss measurements of optical waveguides," Appl. Phys. Lett., 37, 269 (1980).

[112] Y. Okamura et al., "Measuring mode propagation losses of integrated optical waveguides: a simple method," Appl. Opt., 22, 3892 (1983).

[113] J.R. Meyer-Arendt, *Introduction to Classical and Modern Optics*, Prentice-Hall, New Jersey, 1984.

[114] J.L. White and P.F. Heidrich, "Optical waveguide refractive index profiles determined from measurement of mode indices: a simple analysis," Appl. Opt., 15, 151 (1976).

[115] K.S. Chiang, "Construction of refractive-index profiles of planar dielectric waveguides from the distribution of effective indexes," J. Lightwave Tech., LT-3, 385 (1985).

[116] E.Y.B. Pun, T.C. Kong, P.S. Chung, and H.P. Chan, "Index profile of proton-exchanged waveguides in $LiNbO_3$ using pyrophosphoric acid," Elec. Lett., 26, 81 (1990).

[117] M.A. Foad, A. Loni, R.W.Keys, J.M. Winfield, and R.M. De La Rue, "Proton-exchanged Lithium Niobate optical waveguides made from phosphoric acids: detailed studies and comparisons with guides made with benzoic acid," in SPIE OE/FIBERS '89 (Boston, Mass), Integrated Optics and Optoelectronics, Vol. 1177, 31 (1989).

[118] K.K. Wong, T.G. Palanisamy, K.P. Dimitrov-Kuhl, and H. van de Vaart, "High performance proton-exchange $LiTaO_3$ devices for integrated optical sensor applications," in SPIE OE/FIBERS '89 (Boston, Mass.), Integrated Optics and Optoelectronics, Vol. 1177, 40 (1989).

[119] J.L. Jackel, "Recent advances in $LiNbO_3$ integrated optics," Optics News, Feb., 10 (1988).

[120] K. Tada, T. Murai, T. Nakabayashi, T. Iwashima, and T. Ishikawa, "Fabrication of $LiTaO_3$ Optical Waveguide by H^+ Exchange Method," Jap. J. Appl. Phys., 26, 503 (1987).

[121] Y. Li, K. Tada, T. Murai, and T. Yuhara, "Electrooptic Coefficient r_{33} in Proton-Exchanged z-cut $LiTaO_3$ Waveguides," Jap. J. Appl Phys pt. 2, 28,

L263 (1989).

[122] Y. Li, T. Yuhara, K. Tada, "Characteristics of low-propagation-loss $LiTaO_3$ optical waveguides proton exchanged in pyrophosphoric acid," in Technical Digest of Integrated Photonics Research (Hilton Head, SC), Vol. 5, 141 (1990).

[123] V. Hinkov and E. Ise, "Control of Birefringence in Ti : $LiNbO_3$ Optical Waveguides by Proton Exchange of Lithium Ions," J. Lightwave Tech., LT-4, 444 (1986).

[124] J.D. Farina, "Laser annealing of proton-exchanged $LiNbO_3$ integrated-optic structures," in Technical Digest of Integrated Photonics Research (Hilton Head, SC), Vol. 5, 71 (1990).

[125] S.M. Al-Shukri, A. Dawar, R.M. De La Rue, A.C.G. Nutt, M. Taylor, J. R. Tobin, G. Mazzi, A. Carnera, and C. Summonte, "Analysis of annealed proton-exchanged waveguides on $LiNbO_3$ by optical waveguide measurements and microanalytical techniques," in Proc. Top. Meet. Integrated and Guided-Wave Optics (Kissimmee, Fl), Postdeadline Papers, PDP7-1 (1984).

[126] A.C.G. Nutt, K.K. Wong, D.F. Clark, P.J.R. Laybourn, and R.M. De La Rue, "Proton-exchanged $LiNbO_3$ slab and stripe waveguides: characterisation and comparisons," in Proc. 2nd Eur. Conf. Integrated Optics (Florence, Italy), 1983.

[127] A. Dawar, S.M. Al-Shukri, and R.M. De La Rue, "Surface acoustic waveguides optical wave interaction in y-cut $LiNbO_3$ annealed proton-exchanged waveguides," IEEE International Workshop on Integrated and Guided-Wave Optics, Post-Deadline Papers, PD7 (1984).

[128] C. Canali, A. Carnera, P. Mazzoldi, and R.M. De La Rue, "$LiNbO_3$ optical waveguide fabrication by Ti indiffusion and proton exchange: process, perfor-

mances and stability," in SPIE, Integrated Optical Circuit Engineering, Vol. 517, 119 (1984).

[129] J.J. Tuma, *Engineering Mathematics Handbook*, Second Edition, McGraw-Hill, New York, 1979.

[130] V.A. Gan'shin, V. Ivanov, Y. Korkishko, and V.Z. Petrova, "Some characteristics of ion exchange in lithium niobate crystals," Sov. Phys. Tech. Phys., 31, 794 (1986).

[131] J.M. Naden, G.T. Reed, and B.L. Weiss, "Analysis of Prism-Waveguiding Coupling in Anisotropic Media," J. Lightwave Tech., LT-4, 156 (1986).